Assembly of void galaxies: Star formation and molecular gas

Jesús Domínguez Gómez
Depto. Física Teórica y del Cosmos
Universidad de Granada
Programa de doctorado en
Física y Matemáticas (FISYMAT)

Una tesis presentada para la obtención del título de
Doctor por la Universidad de Granada
dentro del Programa de Doctorado en Física y Matemáticas
Supervisado y dirigido por:
Dr. María Isabel Pérez Martín y Dr. Ute Lisenfeld
Julio 2023

UNIVERSIDAD DE GRANADA

FisyMat
PROGRAMA DE DOCTORADO EN FÍSICA Y MATEMÁTICAS

Editor: Universidad de Granada. Tesis Doctorales
Autor: Jesús Domínguez Gómez
ISBN: 978-84-1195-494-5
URI: https://hdl.handle.net/10481/96703

Thesis title: *"Assembly of void galaxies: Star formation and molecular gas"*

PhD Supervisors: Dr. María Isabel Pérez Martín
Dr. Ute Lisenfeld

Part of this work has been previously presented in the following papers published on *Astronomy & Astrophysics* or *Nature*.

1. *"CO-CAVITY pilot survey: Molecular gas and star formation in void galaxies"* by J. Domínguez-Gómez, U. Lisenfeld, I. Pérez, Á. R. López-Sánchez, S. Duarte Puertas, J. Falcón-Barroso, K. Kreckel, R. F. Peletier, T. Ruiz-Lara, R. van de Weygaert, J. M. van der Huls, and S. Verley. *Astronomy & Astrophysics*, Volume 658, A124. Year: 2022. DOI: 10.1051/0004-6361/202141888.

2. *"Galaxies in voids assemble their stars slowly"* by J. Domínguez-Gómez, I. Pérez, T. Ruiz-Lara, R. F. Peletier, P. Sánchez-Blázquez, U. Lisenfeld, J. Falcón-Barroso, M. Alcázar-Laynez, M. Argudo-Fernández, G. Blázquez-Calero, H. Courtois, S. Duarte Puertas, D. Espada, E. Florido, R. García-Benito, A. Jiménez, K. Kreckel, M. Relaño, L. Sánchez-Menguiano, T. van der Hulst, R. van de Weygaert, S. Verley and A. Zurita. *Nature* (in press). Year: 2023. DOI: 10.1038/s41586-023-06109-1.

3. *"Stellar mass-metallicity relation throughout the large-scale of the Universe: CAVITY mother sample"* by J. Domínguez-Gómez, I. Pérez, T. Ruiz-Lara, R. F. Peletier, P. Sánchez-Blázquez, U. Lisenfeld, B. Bidaran, J. Falcón-Barroso, M. Alcázar-Laynez, M. Argudo-Fernández, G. Blázquez-Calero, H. Courtois, S. Duarte Puertas, D. Espada, E. Florido, R. García-Benito, A. Jiménez, K. Kreckel, M. Relaño, L. Sánchez-Menguiano, T. van der Hulst, R. van de Weygaert, S. Verley and A. Zurita. *Astronomy & Astrophysics* (submitted). Year: 2023.

A mi hermano
a mis padres
a mi abuela
a mí

Acknowledgements

Empecemos por lo más importante, la familia.

Gracias Chana. La de veces que me has preguntado durante estos cuatro años que qué me pasa. Pocas veces te ha faltado razón, no hay nada como la intuición de una madre. No ha sido fácil, y tú lo sabes bien ¡cuántas sobremesas callado y pensativo! ¡cuántos días inexpresivo frente al ordenador! y la Chana por ahí husmeando: *"Jesús, ¿no vienes a comerte una frutita?", "¿no quieres hacer un descansito?", "el sábado no trabajarás, ¿no?", "Ahora, después de comer, te echas una siestecita", "¡Ay qué pesailla es la Chana!"*, decías tú, no yo. Pues ya se ha terminado, el doctorado digo, otras cosas vendrán. Gracias por estar ahí, nunca fuiste pesada, nunca lo pensé. Si no hubiera sido por esas "interrupciones", igual esto habría terminado de otra manera. Gracias por estar siempre al otro lado de la puerta, de la escalera, del teléfono. Gracias por estar siempre ahí. Te quiero mamá.

Gracias Manolo. Sumergirse en los detalles puede llevarte a la perdición, a olvidar el objetivo principal. Gracias papá por recordarme siempre que esto es algo mucho más grande y bonito que todos esos código, números y gráficas. ¿Cuántas veces me has preguntado que en qué consiste mi tesis, que qué es el gas molecular y la formación estelar, y que cómo puedo saber esas cosas de las galaxias si están tan lejos? las veces que hiciesen falta. Cada vez que te lo explicaba volvía al principio de todo, cambiaba a un punto de vista global. Ya no ajustaba líneas espectrales sin alma, sino que veía el Universo reflejado en tus ojos, miles de millones de galaxias describiendo una preciosa maraña de luces de colores. Me recordaba manejando telescopios profesionales, viajando al instituciones internacionales de investigación, y trabajando codo con codo con científicos y científicas de prestigio. Gracias papá por recordarme la razón por la que decidí hacer esto. Gracias por devolverme la ilusión cada vez. Te quiero papá.

Gracias Manuel. *"¿Qué pasa tío? así que son"*. Anda hijo, parecía que no iban a terminar nunca estos cuatro años. ¿Me arrepiento? no ¿volvería hacerlo? s(n)í. Ha sido duro pero nada me motiva más que la aprobación de la persona a la que más admiro, mi hermano. A veces no es fácil salir de los bucles, volver a la realidad y relativizar la magnitud de nuestras preocupaciones. No han sido pocos los momentos de agobio y estrés, pero nada como un viajecito a Dornbirn para volver a la calma: diíta de esquí, salchichita, birrita, bajada en trineo, subida al Staufen, brunch en el Pier 69, y mi preferido, los desayunos de 3 horas en casita, con Prosecco, claro. Todo eso está de lujo pero ya sabemos que nos basta con unas barritas, chascas y un buen debate para solucionar el mundo. Lusi, no me olvido de ti ¿cómo podría? *"vamos a llamar a gente, ¡Bravo por la fresquista!"*. No he conocido a una persona más buena y empática que tú. Hablar contigo me da paz. Me cargáis las pilas cada vez que os veo. Me ponéis los pies sobre la Tierra. Me empujáis a seguir. Os quiero.

Gracias Mari. *"¡Ay mi rico! ¡ay mi talento! estás más delgado, cuídate hijo, coooome"*. El cariño de una abuela sólo es comparable al de una madre. Gracias por tu experiencia, por tus recetas. Gracias por casi 90 años de historietas. Gracias por tu alegría y picaresca, que me pintan una sonrisa de oreja a oreja. Te quiero abuela.

Sigamos con los amigos, estas personas que te encuentras y te acompañan por la vida, algunas por etapas, otras hasta el final. A diferencia de la familia, los amigos se pueden elegir, hasta cierto punto. Gracias a todos por elegirme a mí, gracias a todos por caminar a mi lado. Pero siempre hay amigos especiales, amigos que se merecen una mención particular. Gracias a los de siempre: José, Pablo, Manuel. Gracias a los *Niñatos* por esa falta de seriedad tan seria, por quitarle las tonterías a cualquiera, por no permitir ni una pizca de pretensión, por el cariño incondicional, por hacerme sentir uno más. Gracias a los *Amigos de Paco*, que aún diseminados por el mundo seguimos manteniendo la familia con visitas, comidas de accionistas, Oktoberfests, y ahora también con bodas. Gracias al *Trasvase* por acompañarme en uno de los mejores años de mi vida, por dejarme formar parte de vuestra familia napolitana, por seguir juntos después de una década, por venir siempre a mi casa, por hacerme siempre un hueco en la vuestra. Gracias a los hermanos de doctorado, por acompañarme codo con codo estos cuatro años, porque sólo un doctorando entiendo a otro doctorando, gracias a todos, pero sobre todo, gracias a Walo y Manuel porque, como dije antes, siempre hay amigos especiales.

Gracias a mis compañeros. Porque esto no es sólo un trabajo, se convierte en algo más cuando la gente que te acompaña genera a tu alrededor un ambiente familiar más que laboral. Gracias por acogerme, por los cafés de las 11, por integrarme en vuestro *grupus*. Gracias a todos pero, como siempre, hay personas especiales que se merecen algunas palabritas más. Gracias Simon por tu música, por tus enseñanzas, por tu amistad. Gracias Tomás por tu apoyo, por tu paciencia, por tu ilusión.

Gracias a quienes han hecho esto posible. Gracias Isa. Gracias Ute. Cualquiera que lea los agradecimientos dirá que la tesis ha sido un calvario pero todos sabemos que no. Ha sido un viaje muy bonito, hemos aprendido mucho, y no sólo de ciencia. Ha habido muchos momentos de risas y algún que otro *"¡EUREKA!"*. Hace 6 años, antes del máster, me suscribí a *Nature*, recibía la revista en casa cada semana. ¿Quién me iba a decir a mí que haría un doctorado y pasaría a ser uno de los autores de esta revista? *"Sueño cumplido, ¡check!"*. Pero es cierto que ha sido duro en según qué momentos, sobre todo al final. Gracias por vuestra empatía, por dejarme hacer, por guiarme, por sostenerme.

Por último, gracias a mí por mi esfuerzo, por mi trabajo, por mi persistencia, por mantener la ilusión, por continuar, por confiar.

"Before the Big Bang
there was no up
there was no down
there was no side to side

there was no light
there was no dark
nor shape of any kind

there were no stars or planet Mars
or protons to collide
there was no up
there was no down
there was no side to side

and furthermore to underscore this total lacking state
there was no here
there was no there
because there was no space

and in this endless void which can't be thought of as a place
there was no time
and so no passing minutes, hours, days

of all the paradoxes
that belabour common sense
I think this one's the greatest
this time before events

because how did we go from nothing
to infinitely dense?
from immeasurably small
to inconceivably immense?

but before we get unmoored from the question at the start
let's take a breath and marvel
at when math becomes an art

because we don't have to understand it
to know there was a time
when there was no up
there was no down
there was no side to side"

Reina del Cid

Contents

Summary

Galaxies in the Universe are distributed in a web-like structure characterised by different large-scale environments: dense clusters, elongated filaments, sheet-like walls, and under-dense regions, called voids. The low number density of galaxies in voids is expected to affect the properties of their galaxies. Void galaxies are essential to understand the physical processes that drive galaxy evolution as they are less affected by external factors than galaxies in denser environments. Previous studies have shown that galaxies in voids are on average bluer, less massive, and have later morphologies than galaxies in denser environments. However, there is no consensus about the star formation properties of void galaxies, and it has never been observationally proven that their star formation histories are significantly different from those in filaments, walls, and clusters. The Calar Alto Void Integral-field Treasury surveY (CAVITY) project was started to fill this gap by studying in detail a sample of around 300 void galaxies with integral field spectroscopy.

In this thesis, as a preparatory study of the CAVITY project, we analyse stellar populations in the centre of void galaxies to derive the star formation history, which describes the rate at which the galaxies have assembled their stars; and the average stellar metallicity, which traces the accumulated fossil record of star formation through out the entire life of the galaxies. In addition, we also analyse the star formation rate, molecular gas mass, and star formation efficiency of void galaxies as tracers of their current and potential star formation. Comparing the star formation rate, molecular gas, star formation efficiency, star formation history, and stellar metallicity of galaxies in various environments, including voids, filaments, walls, and clusters, can provide valuable insights into how the large-scale environment impacts galaxy evolution.

We present the first molecular gas mass survey of void galaxies,

together with data for the atomic gas mass and star formation rate (SFR) from the literature. We compare with galaxies in filaments and walls in order to better understand how the molecular gas mass and SFR are related to the large-scale environment. We observed with the IRAM 30 m telescope the CO$(1-0)$ and CO$(2-1)$ emission of 20 void galaxies selected from the Void Galaxy Survey, with a stellar mass range from $10^{8.5}$ to $10^{10.3}$ solar masses. We detected 15 objects in at least one CO line. We compared the molecular gas mass, the star formation efficiency (SFE), the atomic gas mass, the molecular-to-atomic gas mass ratio, and the specific star formation rate (sSFR) of the void galaxies with two control samples of galaxies in filaments and walls, selected from xCOLD GASS and EDGE-CALIFA, for different stellar mass bins.

In general, we do not find any significant difference in the molecular and SFR between void galaxies and galaxies in filaments and walls, but some tentative differences emerge for some other parameters when trends with stellar mass are studied. The SFE of void galaxies seems lower than in filament and wall galaxies for low stellar masses. In addition, it appears that there is a trend of increasing deficiency in the atomic gas content in void galaxies compared to galaxies in filaments and walls for higher stellar masses, accompanied by an increase in the molecular-to-atomic gas mass ratio. However, all trends with stellar mass are based on a low number of galaxies and need to be confirmed for a larger sample of galaxies. This study can be considered the starting point and trigger of the CO-CAVITY subproject within CAVITY, aimed at providing comprehensive information of the molecular gas content of the CAVITY galaxies.

We also present the first stellar population comparison between galaxies in different large-scale environments for a stellar mass range from $10^{8.0}$ to $10^{11.5}$ solar masses and a redshift range of $0.01 < z < 0.05$. We aim to better understand how the large-scale structure affects galaxy evolution by studying the star formation history and the stellar mass-metallicity relation of thousands of galaxies, which allows us to make a statistically sound comparison between galaxies in voids, filaments, walls, and clusters. We apply non-parametric full spectral fitting techniques (pPXF and STECKMAP) to 10807 spectra from the SDSS-DR7 (987 in voids, 6463 in filaments and walls, and 3357 in clusters) to obtain their stellar populations (stellar mass, age, and metallicity) and derive their SFH and mass-weighted average stellar metallicity.

We find that void galaxies have had, on average, slower star forma-

tion histories than galaxies in denser large-scale environments. We find two main star formation history types, which are present in all the environments: 'short-timescale' galaxies are not affected by their large-scale environment at early times but only later in their lives; 'long-timescale' galaxies have been continuously affected by their environment and stellar mass. Both types have evolved slower in voids than in filaments, walls, and clusters. We also find that galaxies in voids have on average slightly lower stellar metallicities than galaxies in filaments and walls, and much lower than galaxies in clusters. These differences are more significant for low-mass than for high-mass galaxies, for 'long-timescale' than for 'short-timescale', for spiral than for elliptical, and for blue than for red galaxies.

In this thesis, it is confirmed that the large-scale environment affects galaxy evolution slowing down the star formation history and reducing the stellar metallicity of void galaxies compared to galaxies in filaments, walls, and clusters. In addition, it seems that there are no significant differences with respect to the molecular gas, star formation rate, and star formation efficiency between galaxies in different large-scale environments. However, these last results need to be confirmed for a larger sample of void galaxies.

Resumen

Las galaxias se distribuyen en el Universo describiendo una estructura similar a una red, caracterizada por diferentes ambientes a gran escala: cúmulos densos, filamentos alargados, muros laminares y regiones de baja densidad llamadas vacíos. Se espera que la baja densidad de los vacíos afecte a las propiedades de sus galaxias. Las galaxias de vacíos son esenciales para comprender los procesos físicos que impulsan la evolución de las galaxias, ya que se ven menos afectadas por factores externos que las galaxias en ambientes más densos. Estudios previos han mostrado que las galaxias de vacíos son, en promedio, más azules, menos masivas y tienen morfologías de tipo más tardío que las galaxias en ambientes más densos. Sin embargo, no hay un consenso sobre sus propiedades de formación estelar y nunca se ha demostrado observacionalmente que las historias de formación estelar en vacíos sean significativamente diferentes a las de filamentos, muros y cúmulos. El proyecto Calar Alto Void Integral-field Treasury surveY (CAVITY) comenzó con el objetivo de responder estas dudas estudiando en detalle una muestra de alrededor de 300 galaxias en vacíos con datos espectrales de campo integrado.

En esta tesis, como estudio preparatorio del proyecto CAVITY, analizamos sus poblaciones estelares para calcular la historia de formación estelar, que describe la velocidad a la que las galaxias han ensamblado sus estrellas; y la metalicidad estelar promediada, que traza el registro fósil acumulado de la formación estelar a lo largo de toda la vida de las galaxias. Además, también analizamos la tasa de formación estelar, la masa de gas molecular y la eficiencia de formación estelar de las galaxias de vacíos como indicadores de su formación estelar actual y potencial. Comparar la tasa de formación estelar, el gas molecular, la eficiencia de formación estelar, la historia de formación estelar y la metalicidad estelar de las galaxias en varios ambientes, incluyendo

vacíos, filamentos, muros y cúmulos, puede proporcionar información valiosa sobre cómo el ambiente a gran escala afecta a la evolución de las galaxias.

En esta tesis presentamos el primer estudio de masa de gas molecular en galaxias de vacíos. Comparamos estos datos junto con datos de masa de gas atómico y tasa de formación estelar (SFR, por sus siglas en inglés) obtenidos de la literatura, con respecto a las galaxias en filamentos y muros, con el fin de entender mejor cómo se relaciona el gas molecular y la formación estelar con el ambiente a gran escala. Observamos en el telescopio de 30 m del IRAM la emisión de CO($1-0$) y CO($2-1$) de 20 galaxias en vacíos seleccionadas del Void Galaxy Survey, con un rango de masa estelar de $10^{8.5}$ a $10^{10.3}$ masas solares. Detectamos 15 objetos en al menos una línea de CO. Comparamos la masa de gas molecular, la eficiencia de formación estelar (SFE), la masa de gas atómico, la relación entre la masa de gas molecular y atómico, y la tasa de formación estelar específica (sSFR) de las galaxias de vacíos con dos muestras de control de galaxias en filamentos y muros, seleccionadas de xCOLD GASS y EDGE-CALIFA, para diferentes intervalos de masa estelar y teniendo en cuenta la tasa de formación estelar. Este estudio se puede considerar el punto de partida y detonante del subproyecto CO-CAVITY dentro del proyecto CAVITY, cuyo objetivo es aportar información general sobre el contenido de gas molecular de las galaxias de CAVITY.

En general no encontramos ninguna diferencia significativa en la masa de gas molecular o en la tasa de formación estelar entre las galaxias de vacíos y las galaxias en filamentos y muros. Sin embargo, surgen algunas diferencias tentativas para otros parámetros cuando se estudian las tendencias con la masa estelar. La SFE de las galaxias de vacíos parece ser menor que en las galaxias en filamentos y muros para masas estelares bajas, y parece que hay una deficiencia de H I en las galaxias en vacíos en comparación con las galaxias en filamentos y muros para altas masas estelares, acompañada de un aumento en la relación entre la masa de gas molecular y atómico. Sin embargo, todas las tendencias con la masa estelar se basan en un número bajo de galaxias y deben confirmarse para una muestra de galaxias más grande.

También presentamos la primera comparación de poblaciones estelares entre galaxias en diferentes ambientes a gran escala para un rango de masa estelar de $10^{8.0}$ a $10^{11.5}$ masas solares y un rango de corrimiento al rojo de $0.01 < z < 0.05$. Nuestro objetivo es comprender mejor cómo la estructura a gran escala afecta a la evolución de

las galaxias mediante el estudio de la historia de formación estelar y la relación masa-metalicidad estelar de miles de galaxias, lo que nos permite realizar una comparación estadísticamente significativa entre galaxias en vacíos, filamentos, muros y cúmulos. Aplicamos técnicas no parametrizadas de ajuste espectral completo (pPXF y STECKMAP) a 10807 espectros del SDSS-DR7 (987 en vacíos, 6463 en filamentos y paredes, y 3357 en cúmulos) para obtener sus poblaciones estelares (masa estelar, edad y metalicidad) y calcular las historias de formación estelar (SFH) y las metalicidad estelar media pesada en masa.

En esta tesis mostramos que, en promedio, las galaxias de vacíos han tenido historias de formación estelar más lentas que las galaxias en ambientes más densos. Encontramos dos tipos principales de historias de formación estelar presentes en todos los ambientes: las galaxias con SFH de 'corta escala de tiempo' no se ven afectadas por su ambiente a gran escala en etapas tempranas, sino sólo más tarde en sus vidas; las galaxias con SFH de 'larga escala de tiempo' han sido continuamente afectadas por su ambiente y masa estelar. Ambos tipos han evolucionado más lentamente en los vacíos que en los filamentos, muros y cúmulos. También encontramos que las galaxias de vacíos tienen, en promedio, ligeramente menor metalicidad estelar que las galaxias de filamentos y muros, y mucho menor que las galaxias de cúmulos. Estas diferencias son más significativas para galaxias de baja masa que para galaxias de alta masa, para SFH de 'larga escala de tiempo' que para SFH de 'corta escala de tiempo', para espirales que para elípticas, y para azules que para rojas.

En esta tesis confirmamos que el ambiente a gran escala afecta a la evolución de las galaxias ralentizando la historia de formación estelar y reduciendo la metalicidad estelar de las galaxias de vacíos en comparación con las galaxias de filamentos, muros y cúmulos. Además, parece que las galaxias de vacíos no presentan diferencias en el contenido de gas molecular, la tasa de formación estelar, ni la eficiencia de formación estelar en comparación con galaxias en ambientes más densos. Sin embargo, es necesario confirmar estos últimos resultados para una muestra más grande de galaxias en vacíos.

Chapter 1

Introduction

Contents

1.1 General background

1.1.1 Galaxies

In ancient times, when people gazed up at the sky, their observations were limited to the Sun, the Moon, the fixed stars, the planets, and occasional celestial events like comets and shooting stars. Additionally, they could see the luminous band of the Milky Way (MW) spanning across the night sky. Some Greek philosophers (500-300 BC) such as Aristotle, Anaxagoras, and Democritus proposed that the MW was composed by groups of distant stars. Two thousands years later, Galileo confirmed this when he pointed for the first time a telescope to the sky. Others tried to explain why these distant stars were concentrated in the MW but not uniformly over the sky. Immanuel Kant proposed, based on some of Thomas Wright ideas, that the stars, together with the Sun (and the Earth), were distributed in a planar disc (Longair 2023, L23 hereafter). When we look up to the MW, we are looking in a direction contained in the planar disc where we see a huge number of distant stars. However, when we look at the rest of the sky, we are looking in a direction perpendicular to the planar disc where we only see a few nearby stars contained in the disc below or above the Sun. From this idea, Kant proposed the theory of the island universes (Pérez Fernández 2017, PF17 hereafter).

Until a century ago, it was thought that the MW was the entire Universe and some people like Herschel tried to define a map of the MW. It is necessary to measure the location of the objects over the sky, which is relatively easy, but it is also necessary to measure their distance to us, which is, however, hard to estimate, especially for distant stars. Herschel made the assumption that all stars had the same intrinsic brightness, allowing him to estimate their distances. He found that all the stars were distributed in a finite and very thin disk-like plane (Herschel 1785), breaking with the Giordano Bruno idea of an infinite Universe. However, the assumptions that Herschel made were wrong: not all the stars have the same intrinsic brightness (Michell 1767; Herschel 1802) and the space between the stars, the Interstellar Medium (ISM), is not transparent. Stars may have different masses and compositions that make them brighter or fainter. In addition, the ISM contains gas and dust that absorbs light, dimming the stars that we observe. There was a huge number of stars that Herschel could not see behind the gas and dust, beyond the limits he defined. It was then

impossible to define the limits of the MW.

Claudius Ptolemy was the first one to describe in his book (Almagest) the foggy aspect of some stars, and Abd al-Rahman al-Sufi discovered Andromeda as a cloud, however, we now know that it is another galaxy made out of stars (PF17). Later, Charles Messier catalogued 103 nebulae, and the Herschel siblings, William and Caroline, and subsequently William's son, John, catalogued around a thousand more (Herschel 1864). Later, John Dreyer published an extended catalogue with around 15000 objects: *A New General Catalogue of Nebulae and Clusters of Stars* (NGC galaxies, Dreyer 1888) and two *Index Catalogues* (IC galaxies, Dreyer 1895, 1910). Some of these objects were actually galaxies. Around a century ago, the differences between a nebula, a stellar cluster or a galaxy were not clear. Some people such as Shapley thought that the MW was the entire Universe, others like Curtis thought that some nebulae were inside the MW but others were independent galaxies beyond. In 1920, they both led the Great Debate (Hoskin 1976; Smith & Gingerich 1982; Trimble 1995; Longair 2023) to decide who was right, however, nothing was concluded until Hubble measured the distance to Andromeda by applying the period-luminosity relation of cepheids, which was discovered by Leavitt & Pickering (1912), and found that Andromeda is outside the MW. Curtis was right.

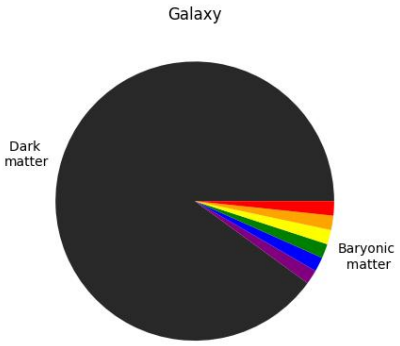

Figure 1.1: **Schematic chart of the fraction of matter in a galaxy:** dark matter (90%) in grey and baryonic matter (10%) in colours.

Galaxies are formed by stars, gas, and dust, but this is only the $\sim 10\%$ of the mass of the galaxies, the baryonic matter (see Figure 1.1). The rest of the matter ($\sim 90\%$) in a galaxy is dark matter. Dark matter does not have charges as protons and electrons, so it does not absorb, emit, or reflect the light (it is invisible) and only interacts with baryonic matter by gravity. The dark matter has not been physically detected yet but its gravitational effects have been observed in the rotation curves of disk galaxies, the kinematics of galaxy clusters, and the gravitational lens-

ing. The rotation curve of the stars and gas around the centre of a galaxy is determined by the mass of the galaxy. However, when Rubin et al. (1980) measured the velocity of the stars and drew the rotation curve, she saw that the estimated mass of the galaxy was much larger than what it was observed. Additionally, according to the general relativity of Einstein (1915, 1916), gravity curve the path of the light. If a cluster of galaxies is between us and a far galaxy, the light of the galaxy that goes around the cluster is deviated by gravity to us, we then can see several disrupted images of the far galaxy, or even a ring (the Einstein ring) projected around the cluster. Observing the different projections of the galaxy, we can estimate the mass of the cluster but, again, the estimations are much larger than what we observe. This excess of mass is what we call dark matter (Gabàs Masip 2017).

Morphology

Hubble was the first to study the properties of the galaxies and classify them according to their morphology (Hubble 1926) in the visible wavelength range following the Hubble sequence (see Figure 1.2). He defined three types of galaxies: elliptical, spiral, and lenticular galaxies. There is another morphological type, the irregular galaxies, designed by the acronym Irr, which were not considered in the Hubble sequence. Hubble thought that his morphological classification was also a scheme of the evolution of the galaxies. He thought that an elliptical (or early-type) galaxy could generate a disc, evolving to a spiral (or late-type) galaxy. Now, the opposite theory is the most accepted, elliptical galaxies are supposed to form after the merging of two spiral galaxies (L23).

Elliptical (E) galaxies have the shape of an ellipsoid, have little amount of gas, are formed mainly by old red stars, and barely form new stars. Spiral (S) galaxies have the shape of a disk with a Black Hole (BH) in the centre, spiral arms, and a bulge, which can form a bar (SB). They have a relatively high amount of gas from which they form new stars inside their spiral arms. Lenticular (S0) galaxies also have disk, bulge but they do not contain much gas so they do not have star forming spiral arms. Irregular (Irr) galaxies have neither disk nor elliptical shape, they are gas-rich and star-forming galaxies but do not have spiral arms or a defined centre or bulge.

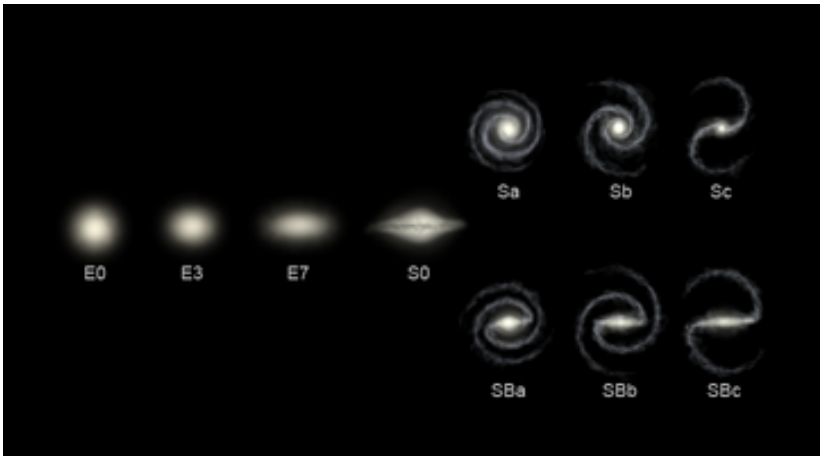

Figure 1.2: **Edwin Hubble morphological classification of galaxies.** Credit: https://upload.wikimedia.org/wikipedia/commons/thumb/8/8a/Hubble_sequence_photo.png/360px-Hubble_sequence_photo.png

Colour magnitude diagram

The Colour Magnitude Diagram (CMD) represents the distribution of galaxies according to their colour and magnitude, and it is useful to classify galaxies as the colour is a proxy of their star formation activity and the magnitude is a proxy of their stellar mass ($M_\star$). The colour of the galaxies depends on the type of their stars, their Star Formation Rate (SFR), and the amount of dust in their ISM. Massive stars are hotter and bluer than less massive stars, which are colder and redder (see Section 1.1.3). Massive blue stars have short lifetimes, so they are only found in galaxies that are currently forming stars. Additionally, if the ISM of a galaxy has much dust, it absorbs the radiation of the stars, more efficiently at high frequencies (blue) than at low frequencies (red), reddening the light.

There are three main galaxy populations in the CMD (Figure 1.3): the red sequence, the blue cloud, and the green valley. The red sequence is populated by red galaxies that are typically quenched and elliptical. In the blue cloud we typically find blue, spiral, and star-forming galaxies. Galaxies from the green valley have intermediate properties and might be evolving between the blue cloud and the red sequence (L23). In general, galaxies are assumed to start their lives forming stars in the blue cloud. They increase their stellar mass, moving to the right side

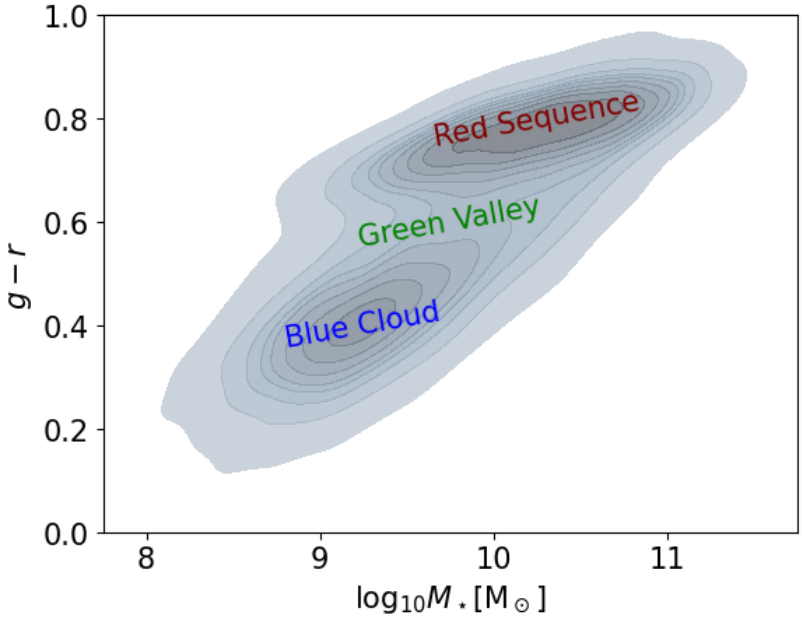

Figure 1.3: **Colour-mass diagram (CMD) of galaxies.** Density distribution of galaxies in the colour vs. stellar mass plane. Three galaxy populations are highlighted in the CMD: blue cloud (blue), green valley (green), and red sequence (red). This figure is made with galaxies from the SDSS within a redshift range of $0.01 < z < 0.05$.

of the CMD, until the star formation stops for some reason. When the SFR decreases, the galaxy get redder, moves up in the CMD into the red sequence. They do not increase their stellar mass unless they start forming stars again (coming back to the blue cloud or the green valley), or they merge with other galaxies (moving over the red sequence to the upper right corner of the CMD, see Section 10 in Cimatti et al. 2020).

The SFR is a measurement of the current star formation of the galaxy, which is the average stellar mass in units of solar mass ($M_\odot$) that is formed in the galaxy per year. Galaxies can be classified as star-forming, quenched, or starburst galaxies. Star-forming galaxies are typically spiral, blue, and gas-rich galaxies, and their SFR correlates with their stellar mass (or brightness) along the Star-Forming Main Sequence (SFMS), see Figure 1.4. Quenched galaxies are typically elliptical, red, and gas-poor galaxies with low SFRs, below the SFMS. Starburst galaxies are star-forming galaxies with extremely high SFRs,

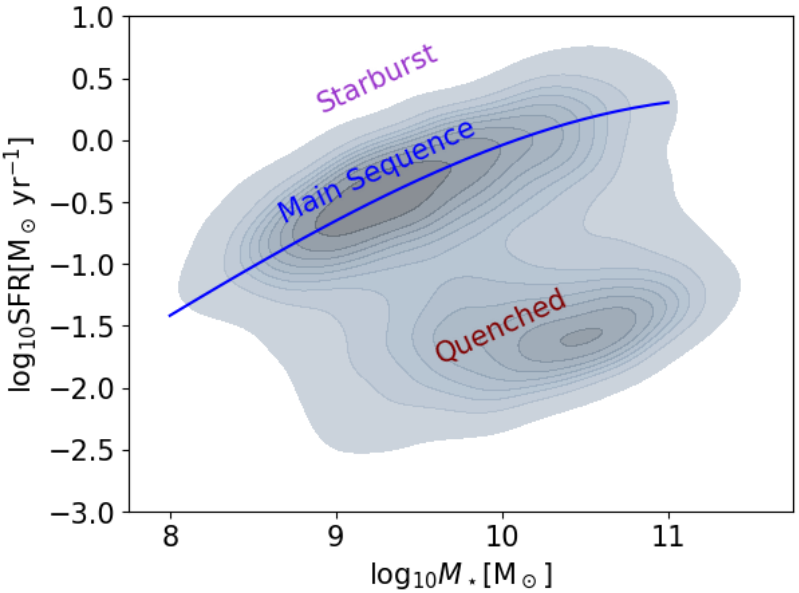

Figure 1.4: **Density distribution of galaxies in the Star formation rate (SFR) vs. stellar mass ($M_\star$) diagram.** Three populations are highlighted in the diagram: starburst (purple), star forming main sequence (blue), and quenched (red) galaxies.

above the SFMS (Cimatti et al. 2020).

1.1.2 Interstellar medium

The ISM is the matter in between the stars, around 10% of the baryonic mass of the galaxy. It is made out of cold and hot gas, dust, and high energy particles, all embedded in magnetic fields. One of the goals of this thesis is to study the star formation properties of galaxies, which is directly linked with the gas in their ISM. The gas is made out of hydrogen (70%), helium (28%), and a small fraction (2%) of metals, which are elements heavier than helium (He). The gas can be found in three different states: atomic, molecular, and ionised (PF17). Here we give a brief introduction of the relation between the star formation and the different states of the gas.

The atomic gas (H I) is the reservoir of matter from which the stars will form in the future. It can be found in a diffuse distribution around the galaxy but also as clouds inside the disk. It is mainly made out of

neutral hydrogen, which does not emit any recombination, vibrational, or rotational line. However, when the electron of an atom of Hydrogen change its spin, it emits a photon at 21 cm, allowing astronomers to detect H I.

The molecular gas (H_2) is mainly found in compact ($\sim$ 1 pc), cold ($\sim$ 10 K), and dense ($\sim 10^3$ cm^{-3}) clouds inside the galaxy disk (see Table 16.2 in Wilson et al. 2013). These densities are high enough for the gas to collapse prior to the imminent star formation. The amount of molecular gas provides us an estimation of the potential star formation of the galaxy. The atoms of hydrogen in the ISM combine and form molecular hydrogen. However, the density of the atomic clouds is so low that it is very unlikely that two atoms of H collide to form a molecule. It is more likely that atoms of H collide with a relatively large grain of dust, stick to its surface, and find other atoms of H there. The molecule of H_2 forms on the surface of the grains of dust, and later leaves into the ISM (Gould & Salpeter 1963). The more dust, the more molecular gas. Molecular clouds do not receive enough radiation to ionise their molecules and emit observable recombination lines. Hydrogen form symmetric molecules without electric dipole, so they do not emit vibrational or rotational lines. Among others, carbon monoxide (CO) is commonly used as a tracer to estimate the total mass of molecular clouds. It is a molecule with electric dipole, which emits rotational lines (wavelengths of 1 and 3 mm), and is abundant in molecular clouds. It is well known that there are around 10^4 molecules of H_2 per molecule of CO, depending on the metallicity, temperature, and density of the cloud (Solomon et al. 1997; Bolatto et al. 2013).

Another form in which hydrogen is found in the ISM is ionised, and it is usually concentrated in the so-called H II regions. Such ionised gas is an indicator of the SFR of the galaxy. When massive stars finally form from the collapse of the molecular gas, they emit energetic photons that excite the electrons of the gas, generating ionised regions, the H II regions. The excited electrons can also emit a photon and come back to its initial state (emission lines). Measuring the intensity of these emission lines (i.e. Hα from the Blamer series), we can estimate the SFR of the galaxy (Hao et al. 2011; Murphy et al. 2011).

1.1.3 Stellar populations

We now know what a galaxy is, and we know that stars are one of their main constituents. However, as always in science, this knowledge,

together with the understanding of what stars are, took a long time to unveil. According to Aristotle, the Universe was divided into the Earth (everything below the Moon) and the sky (everything above the Moon). The Earth was imperfect and mutable, things changed and moved up and down. The sky was perfect and stable, planets and stars moved describing perfect circles and the stars were fixed in the firmament. In this sense, every temporal event that was seen on the sky, as a nova or a comet, were thought to happen, as meteors, in the mutable atmosphere, below the Moon. This model was believed for a long time until Tycho Brahe proved in 1572 that the novae took place beyond the Moon, outside the atmosphere. Later, David Fabricius in 1596 and Geminiano Montanari in 1667 discovered stars that change their characteristics with time. And finally, Edmon Halley discovered in 1718 that stars move over the sky. Definitely the sky is not immutable and the stars are not fixed in the firmament (Galadí-Enríquez 2016, GE16 hereafter).

Kelvin and Helmholtz said that the energy of the Sun comes from its gravitational collapse. However, according to this, the lifetime of the Sun would be just about 30 Myr, which was much longer than the age that the Bible estimated for the Earth ($\sim$ 5 kyr), and much shorter than the estimations of geology, and biological evolution ($\sim$ 300 Myr). Later, Fritz Houtermas discovered in 1927 that the energy of the Sun was due to the nuclear fusion of the atoms in its core. According to this physical process, the estimated lifetime of stars were in agreement with geological and biological processes. A star is a massive and compact accumulation of hot gas in hydrostatic equilibrium. The temperature and pressure in its core are high enough to fuse the nuclei of light atomic elements into heavier elements emitting radiation. During its normal behaviour, the star is in equilibrium as the pressure and the emitted radiation compensate the gravitational force (GE16).

Stars were thought to be of different natures as they may have different intensities and colours. In addition, it was also assumed that the composition of the Sun was similar to the Earth until Cecilia Payne discovered in 1925, using spectroscopy, that the Sun is formed mainly by hydrogen (H). The relative abundance of H is 10000 times higher than the metals. Now we know that the Universe is formed by $\sim$ 74% of H, $\sim$ 25% of He, and $\sim$ 1% of metals. The Earth's crust is made out of 50% oxygen but the stars only possess 1% of oxygen. All the stars are of the same nature and their characteristics (such as luminosity, colour, spectrum, and size) are determined by their initial mass, the

stage of their evolution, and their metallicity (GE16).

Spectral types

The spectra of the stars are then classified according to their temperature and composition. The Harvard classification divides stars into classes from A to Q (in alphabetic order) according to the intensity of the absorption lines of hydrogen (Balmer series), from more (A) to less (Q) intense. Later, it was discovered that the temperature is the main parameter that determines the spectra of a stars, and the classification was reduced and reordered from higher to lower temperature: O, B, A, F, G, K, M, with sub-types from 9 to 0. In addition, two stars may have the same spectral type but different size, and consequently different luminosity and gravity in their surface. Yerkes classified the stars according to their sizes from type I (super-giant) to VII (dwarf) (GE16).

Hertzsprung-Russel diagram

The Hertzsprung-Russel (HR) diagram (see Figure 1.5) is useful to classify the stars according to their temperature (horizontal axis) and luminosity (vertical axis). Hotter stars are located to the left and colder ones to the right, more luminous stars to the top and dimmer ones to the bottom. The temperature can be replaced by other related properties such as spectral type or colour, from O and blue in the left to M and red to the right. The position of a star in the HR diagram is not random, but follows the stellar evolution theory. When a star forms, it appears in the Main Sequence (MS), diagonal of the HR diagram; in the upper left end if it is massive, hot, and blue, or in the lower right end if it is less massive, cold, and red. Stars spend most of their lives in the MS but, depending on their mass, they finally move to other regions of the diagram as giant stars (upper right) or white dwarfs (lower left). While the stars evolve over the HR diagram their spectra evolve as well. Therefore the mass, metallicity, and age of the stars may be estimated from their spectra (GE16). This concept will be key in our analysis to derive the stellar populations of the galaxies from their spectra (see Section 4).

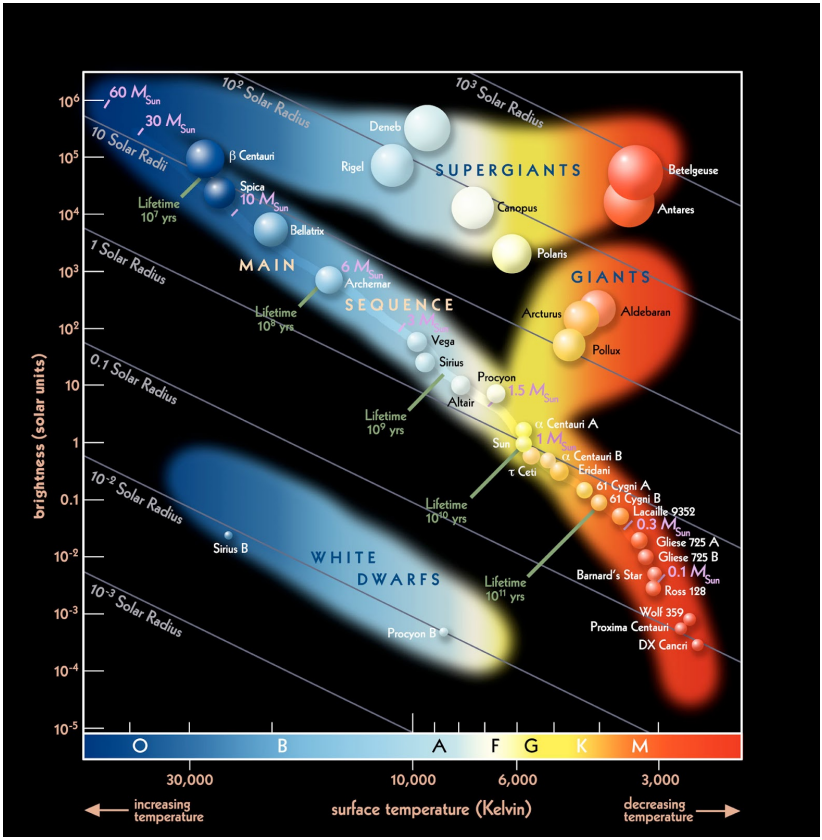

Figure 1.5: **Hertzsprung-Russell diagram:** The vertical axis represents the brightness of the star in solar units, the horizontal axis the surface temperature in Kelvin of the star, which is associated with its type of spectrum (from O to M, according to the Harvard classification) and colour. The coloured areas are the regions where we can find different types of stars, such as main sequence, giants, supergiants and whit dwarfs. The diagonal straight lines represent different stellar sizes. The estimated lifetime (green) and mass (pink) of the stars are indicated over the main sequence. The spheres are examples of real stars but their sizes are not scaled. Credit: https://scienceabovetheclouds.blogspot.com/2016/06/pianeti-terrestri-vicino-noi-solo-40.html

Birth of stars

Stars form from a cloud of molecular gas that collapses under gravity after a perturbation such as a shock wave of a supernova, or a density wave in the spiral arms of a disk galaxy. The cloud increases its temperature and pressure slowing down the collapse but the black-body emission, and the emission lines of the metals reduce the energy of the cloud, which keeps collapsing. The more metals, the higher the emission, and the faster the collapse. If the cloud collapses fast, there is no time for the gas to rearrange, and the cloud breaks up into smaller collapsing clouds, forming many small stars. It is more likely to form low-mass, red, cold stars than massive, blue, hot ones. The probability distribution of the mass of the stars that form from a cloud is called Initial Mass Function (IMF). When the temperature and pressure inside the core of the sub-clouds are high enough, the nuclear fusion starts, emitting a huge amount of energy that, together with the pressure, balances the gravitational collapse inside the stars.

If we represent over the HR diagram all the stars that form at the same time from a cloud of gas, they would start their lives distributed along the MS. Stars spend the major part of their lives on the MS burning H into He. Once H is used up in the inner region, conditions become unstable and the stars expand and leave the MS. Massive stars have higher temperature and pressure in their cores, making the nuclear fusion faster so that they leave the MS earlier than less massive stars. If we represent the position of stars on the HR diagram after a few Myr, the most massive stars will no longer be located on the MS but have moved towards lower temperatures after expanding as giant stars. The distribution of a population of stars with the same age and metallicity but different masses outlines over the HR diagram what we called an isochrone (see Section 3.9.2 in Schneider 2015).

1.1.4 Mapping the Universe

Determining the position of an object on the sky is straightforward. However, measuring its distance is much more difficult. We can estimate the distance of stars within the MW applying parallax up to $\sim$ 30 pc, or even $\sim$ 2.5 kpc from satellites such as Gaia. At larger distances ($\sim$ 7 Mpc), we use cepheid stars to estimate the distance of nearby galaxies after relations have been calibrated (see Section 11.2 in Combes et al. 2002). At larger distances, where we can not resolve individual stars, we use SuperNova type Ia (SNIa), which is an

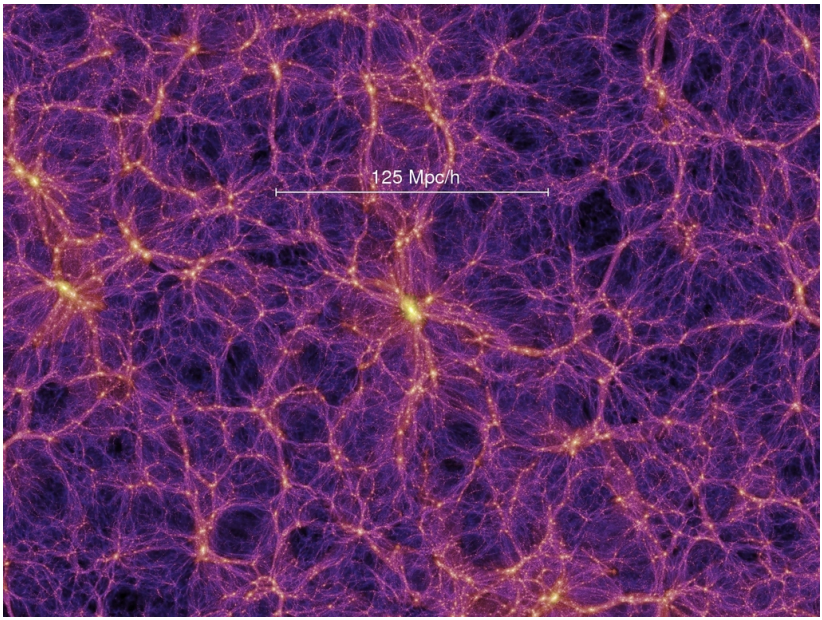

Figure 1.6: **Large-scale structure of the universe.** Dark matter distribution of the Millennium Simulation from the Max-Planck-institute für Astrophysik. Image from ESA/Plank. Credit: https://wwwmpa.mpa-garching.mpg.de/galform/virgo/millennium/

intense standard candle that allow us to estimate the distance of far-away galaxies. Heber Curtis observed for the first time that a SNIa in the Andromeda galaxy was ten times dimmer than in the MW, from which he estimated that the distance to Andromeda was more than 0.5 million light-year (Gabàs Masip 2017). Later in 1912, Vesto M. Slipher observed that the spectra of the galaxies were shifted to redder frequencies, they were redshifted, and Hubble found a correlation with distance (Hubble 1929). This is what we call the Hubble flow, and we can use it to estimate a first approximation of the distance of the galaxies by measuring the redshift of their spectra. We then can measure the distribution of galaxies in the tridimensional space and draw the large-structure of the Universe (see Figure 1.6).

Cosmic Microwave Background Radiation

The Hubble flow proofs that the Universe is expanding, galaxies are moving away from each other, the farther, the faster. Friedmann (1922,

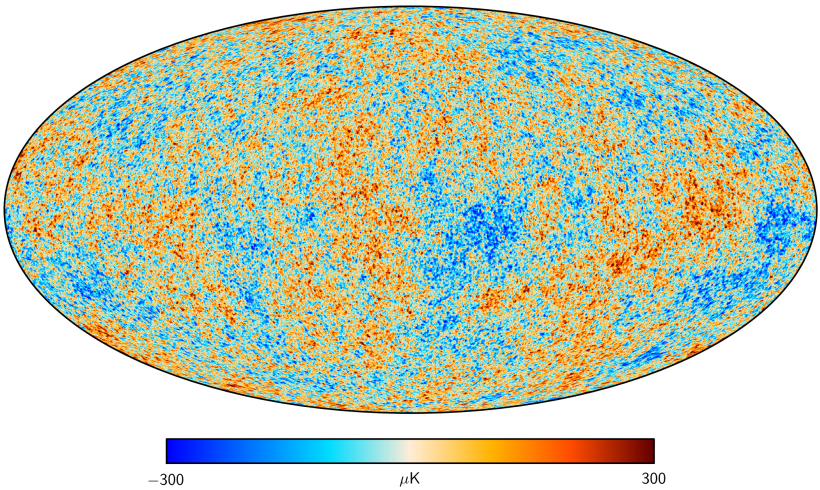

Figure 1.7: **Map of the temperature fluctuations in the Cosmic Microwave Background Radiation.** Image from ESA/Plank. Credit: https://www.cosmos.esa.int/web/planck.

1924) and Lemaître (1931) applied general relativity to the Universe and suggested that if it is expanding, all might have started concentrated in a unique point, what we now call the Big Bang. Later, Penzias & Wilson (1965) discovered the Cosmic Microwave Background Radiation (CMBR), which was a major proof that supports the Big Bang theory. According to this theory, in its first stages, the Universe was small, dense, and hot. The energy of the photons maintained all the matter ionised as plasma with free protons and electrons. The Universe was expanding and the plasma was cooling down until it reached a temperature of 3000 K. Then, the energy of the photons was not enough to ionise the matter anymore, protons and electrons recombined, and photons propagated as free radiation. After the recombination, the Universe kept expanding and the free radiation has been cooling down until today. We still detect this radiation with radio-telescopes in the wavelength range of 1 cm $< \lambda <$ 1 m with the intensity spectrum of a black-body at a radiation temperature of about 2.7 K. The intensity of the CMBR is very uniform all over the sky, so the distribution of matter in the early Universe was very homogeneous. However, there are small temperature fluctuation, ie. red and blue regions in Figure 1.7, corresponding to relatively hot over-densities and cold under-densities in the early Universe. We know that the fluctuations of the CMBR

are too small to give rise to the present-day large-scale structure of the universe. At the moment of recombination, the density fluctuations of dark matter must have been much higher, and those have produced the present large-scale structure (L23).

1.2 Galaxy formation

In 1915 Albert Einstein developed the General Theory of Relativity (Einstein 1915, 1916), which explains the deformation of the space-time caused by the presence of matter, as well as how matter moves within the curved space-time. In addition, Bernhard Riemann defined closed spherical non-Euclidean geometries. Together, they enabled the formulation of self-consistent models of the Universe as a whole, and established a connection between the geometry of the space-time and the gravitational forces that shape the large-scale structures of the Universe. In 1917, Einstein introduced the *cosmological constant* Λ to his equations as he could not find static solutions for the Universe (Einstein 1917). Later, Friedmann (1922, 1924) and Lemaître (1931) found static and expanding solutions of the Einstein's field equations without the need of a cosmological constant. Einstein considered the introduction of the cosmological constant as the biggest blunder of his life (Gamow 1970). The Friedman solutions estimated the age of the Universe as $1/\mathrm{H}_0 \sim 2$ Gyr, where $\mathrm{H}_0 \sim 500$ km s^{-1} Mpc^{-1} was the first estimation of the Hubble's constant. This time-scale was less than the age of the Earth as estimated by nucleocosmochronology. A positive value of the cosmological constant solved this controversy as it increases the expansion time-scale of the Universe. However, the Hubble constant was overestimated, it is actually $\mathrm{H}_0 \sim 70$ km s^{-1} Mpc^{-1}, alleviating the controversy between the age of the Earth and the age of the Universe (L23).

Currently, there is still a controversy about the Hubble constant, commonly known as the Hubble tension. This refers to the inconsistency between direct and indirect methods to estimate the expansion of the Universe (Poulin et al. 2023). Direct methods measure values of the Hubble constant as $\mathrm{H}_0 = 73.04 \pm 1.04\,\mathrm{km\,s^{-1}\,Mpc^{-1}}$ by observing current probes of the late-universe, such as cepheids and SNIa. Indirect methods provide estimates of $\mathrm{H}_0 = 67.27 \pm 0.60\,\mathrm{km\,s^{-1}\,Mpc^{-1}}$, inferred by the Λ Cold Dark Matter (ΛCMD) cosmological model calibrated on early-universe data, i.e. the CMBR. Numerous other techniques have

been applied to understand the Hubble tension but this remains an unsolved problem.

The first models of the Universe (i.e. Friedmann) were defined as isotropic and uniform, with no structure, dark matter, or dark energy. However, when considering small density perturbations and their evolution under gravity, the Universe develops structures. Jeans (1902); Lemaître (1933); Tolman (1934); Lifshitz (1946) studied the criteria for the gravitational collapse in the different Friedman models, and concluded that galaxies and the large-scale structure of the Universe can not have formed from infinitesimal random density fluctuations but from finite perturbations. Novikov (1964) estimated that structures such as galaxies or clusters of galaxies formed from density perturbations with amplitudes of $\delta\rho/\rho \sim 10^{-4}$, which are not infinitesimal and are generated by physical processes occurring in the very early Universe (L23). According to Jeans' prescription, density perturbations were adiabatic sound waves. Silk (1968) demonstrated that these waves experienced damping due to repeated electron scatterings, resulting in the dissipation of fluctuations with masses below the Silk mass (approximately 10^{12} $M_\odot$). Consequently only very massive galaxies and large-scale structures could form after recombination. Alternatively, Peebles and colleagues proposed an isothermal model where the fluctuations were not sound waves but isothermal perturbations. In this model, small-scale fluctuations ($> 10^6$ $M_\odot$) survived to the recombination epoch, and galaxies formed through hierarchical clustering under the influence of gravitational perturbations on larger scales. The adiabatic model leads to a "top-down" process in which the large-scale structure form first and galaxies are formed at relatively later epochs by fragmentation. However, the isothermal model leads to a "bottom-up" in which galaxies form at very early cosmic epochs and gather to form larger structures (L23).

Harrison (1970) and Zeldovich (1972) analysed the size distribution of the observed structures of the Universe, and inferred the Harrison-Zeldovich spectrum of initial perturbations with amplitudes of $\sim 10^{-4}$. Sachs & Wolfe (1967) assumed that the recombination process was instantaneous, and obtained that the adiabatic initial perturbations resulted in temperatures fluctuations of $\Delta T/T = \frac{1}{3}\Delta\rho/\rho$. The baryonic theories (adiabatic and isothermal) predict temperature fluctuations in the range of $\Delta T/T \sim 10^{-3} - 10^{-4}$, which should be observed in the intensity distribution of the CMBR. However, this was in conflict with the increasingly sensitive ($\Delta T/T < 10^{-4}$, Partridge 1980a,b) observa-

tions of the CMBR, which set an upper limit of the fluctuations below the values estimated by the models with low density parameters.

The upper limit of the baryonic density fluctuations requires that most of the matter in the Universe is non-baryonic (L23). Two solutions for this problem are the hot and the cold dark matter. Lyubimov et al. (1981) showed in their experiments that the electron neutrino had a rest-mass of ~ 30 eV. Gershtein & Zel'dovich (1966) estimated that neutrinos with a similar rest-mass could have a significant impact on the overall mass density of the Universe. Doroshkevich et al. (1980) introduced a new version of the adiabatic model in which the Universe is dominated by neutrinos with finite rest-mass. In this scenario, known as the *Hot Dark Matter* model, neutrinos were relativistic when decoupled from the plasma. As neutrinos are very weakly interacting particles, they propagate mostly freely, smoothing out the small density perturbations quickly. As in the adiabatic model, only large-scale density fluctuations survived the recombination epoch. The Hot Dark Matter model reduces the estimations of the temperature fluctuations in the CMBR below the observational upper limits. It could predict the formation of large-scale structures such as clusters of galaxies by assuming a neutrino rest-mass of ~ 30 eV, or heavier to predict the formation of smaller structures such as dwarf galaxies Tremaine & Gunn (1979). However, the Lyubimov et al. (1981) estimation was wrong, the rest-mass of the neutrino is not ~ 30 eV but ~ 1 eV.

In 1982, James Peebles and Richard Bond introduced the *Cold Dark Mater* to encompass new particles candidates for the dark matter. In this scenario the particles were non-relativistic when decoupled from the plasma. The matter was cold and the small perturbations did not damped out by fast propagating weakly interacting particles. As in the isothermal model, after recombination, baryonic matter collapsed within the potential wells of dark matter, forming galaxies, groups, and clusters in a hierarchical clustering. Peebles (1982) demonstrated that the Cold Dark Matter predicts fluctuations of the CMBR below the observational upper limits. Both, Hot and Cold Dark Matter models predict CMBR fluctuations of $\Delta T/T < 10^{-5}$, which were observed with the NASA Cosmic Background Explorer (COBE) with an angular resolution of 7° (Smoot et al. 1992), later with the Wilkinson Microwave Anisotropy Probe (WMAP, Bennett et al. 2003), and the ESA Plank satellite with angular resolution of 5 arcmin (Planck Collaboration et al. 2020). These fluctuations correspond to the largest voids observed in the distribution of galaxies (L23).

The Cold Dark Matter is considered the picture that best describe the formation of galaxies and the large-scale structure of the Universe, and its parameters have to be derived from the observations. The observation of SNIa up to redshift $z \sim 1$ allowed Knop et al. (2003) and Tonry et al. (2003) to find that the cosmological constant is not zero, and fitted the density parameter $\Omega_\Lambda = \Lambda/3H_0^2 \sim 0.7$, also known as dark energy, generating the ΛCDM model. For this thesis, we assume a flat ΛCDM cosmology with a matter density $\Omega_M = 0.3$, a dark energy density $\Omega_\Lambda = 0.7$, and a Hubble constant $H_0 = 70\,km\,s^{-1}\,Mpc^{-1}$.

1.3 Large-scale of the Universe

The discovery of the Universe's accelerated expansion revealed that matter and radiation alone cannot explain its evolution. To accommodate the observations in the general relativity, it was necessary to include dark energy with negative pressure, which accelerates the expansion. The SNIa, the CMBR, and the Baryon Acoustic Oscillations (BAO) are some of the probes that allow us to derive the cosmological parameters from the observations. The BAO represents correlated over-densities in the matter distribution on large scales (Percival et al. 2001; Cole et al. 2005; Eisenstein et al. 2005). It can be interpreted as the imprint of the sound waves in the original fluctuations at the recombination epoch, and it has shaped the large-scale structure of the expanding Universe (Moresco et al. 2022).

Galaxies in the Universe are distributed in a web-like structure characterised by different large-scale environments: dense clusters, elongated filaments, sheetlike walls, and under-dense regions, called voids (Peebles 2001; Kreckel et al. 2011; Pan et al. 2012; Varela et al. 2012; van de Weygaert 2016). Voids are the most under-dense large-scale regions in the Universe. They occupy large volumes ($10 - 30\ h^{-1}$ Mpc in diameter) with density contrast of $\delta = \delta\rho/\rho \lesssim -0.8$, (Peebles 2001; Kreckel et al. 2011, 2012; Pan et al. 2012; Varela et al. 2012; van de Weygaert 2016), where ρ is the average density of the Universe. They are inhabited by the void galaxy population, which is partially distributed along filament-like substructures throughout the void, also known as tendrils. These substructures have been modelled by numerical simulations (van de Weygaert & van Kampen 1993; Sheth & van de Weygaert 2004; Aragon-Calvo & Szalay 2013; Ricciardelli et al. 2013; Rieder et al. 2013) and were also observed (Patiri et al. 2006; Beygu et al. 2013; Al-

paslan et al. 2014).

Clusters are occupied by groups of numerous galaxies, which are luminous and easily detectable. On the contrary, voids host less luminous galaxies, which are harder to detect. In order to identify a void, it is essential to measure its boundaries and detect the faint galaxies residing within it. This is possible by applying void finder algorithms, such as the Watershed Void Finder (WVF) and the VoidFinder (described in sections 2.1.1 and 2.2, respectively), to large deep redshift galaxy surveys such as the Sloan Digital Sky Survey (SDSS) presented in York et al. (2000), the 2dF Galaxy Redshift Survey (2dFGRS, Colless et al. 2001), or the 2MASS Redshift Survey (2MRS, Huchra et al. 2012), which show the large-scale structure of the Universe.

The low number density of galaxies within voids makes them remarkably sensitive to neutrinos and dark matter. Neutrinos, due to their low mass, can permeate the innermost regions of the voids, while baryonic and dark matter remain confined to their boundaries by gravitational forces. Dark energy dominates the matter-energy balance in the voids compared to the Universe as a whole (Moresco et al. 2022, and references therein). This scenario is supported by the Goldberg & Vogeley (2004) simulation, in which, following Birkhoff's theorem (Birkhoff 1927), they assume that the internal dynamics of voids are spherical, symmetric, and evolve independently of the dynamics of the outside universe. According to their approximation, voids evolve as a universe with a larger Hubble constant (H_0), and a smaller matter density (Ω_M) but the same cosmological constant (Λ), which also implies a lower Ω_Λ than the average Universe. However, Birkhoff's theorem is a crude approximation on how the voids behave. Other simulations have shown that voids do not evolve independently of the outside universe as matter may move from filaments to voids (Vallés-Pérez et al. 2021), and all voids do not develop a symmetric expansion but may close along one or two directions (Sheth & van de Weygaert 2004; Lavaux & Wandelt 2010). In addition, an observational study (Courtois et al. 2023) has recently shown that some voids (defined by the spatial distribution of galaxies) may be dense reservoirs of dark matter (derived by the velocity of galaxies), which contradicts the notion that the matter density within all voids is lower than that of the average universe. Much remains unknown about the cosmological characteristics of voids and the dynamical behaviour of galaxies within them.

The origin of these large-scale structures are the primordial density fluctuations of the Universe. Studying the current large-scale distri-

bution of galaxies can bring valuable cosmological information of the primordial Universe. Standard galaxy clustering analysis is more sensitive to collapsed regions such as galaxy clusters, where the number of galaxies is statistically high. However, galaxies are virialised in clusters and loose memory of the initial conditions of the Universe. On the contrary, low-density regions such as voids remain more linear and retain insights of the primordial conditions of the Universe. Therefore, to extract cosmological insights it is necessary to explore voids with a statistically significant number of galaxies in multiple voids to compensate the lower number of galaxies within them (Pisani et al. 2019).

1.4 Void galaxies

Void galaxies are essential to understand the physical processes that drive galaxy evolution as they are less affected by an intense gravitational potential and external processes than galaxies in filaments, walls and clusters. These external processes include mergers or tidal interactions with other galaxies, as well as hydro-dynamical interactions between the IntraCluster Medium (ICM) and the ISM, such as ram pressure stripping (Boselli & Gavazzi 2006). This makes voids a good probe to study the intrinsic properties of galaxies and compare them with galaxies in denser large-scale environments, where the galactic properties are more affected by external processes and altered by an accelerated evolution. Void galaxies represent a unique galaxy population based on which astronomers can unveil how the large-scale environment affects the assembly, evolution, and properties of galaxies.

Previous studies have shown that galaxies in voids are on average bluer, less massive, and have later morphological types than galaxies in filaments and walls (Rojas et al. 2004; Park et al. 2007; Hoyle et al. 2012; Kreckel et al. 2012; Florez et al. 2021). In addition, Porter et al. (2023) have recently found that at low redshift ($z < 0.075$) the fraction of late-type galaxies is higher in voids than in the field but these differences are not conclusive at higher redshifts ($0.075 < z < 0.150$). All these results show that void galaxies are, on average, active galaxies and suggest that they are at an early stage of their evolution, in contrast to galaxies in denser environments, which are, on average, more passive.

The fraction of galaxies with an elevated SFR is higher in voids than in denser environments. However, there is no consensus about SFR differences for a given stellar mass, luminosity, or morphology. Some

studies have found that void galaxies have an enhanced SFR for a given stellar mass (Rojas et al. 2005; Beygu et al. 2016; Florez et al. 2021) but others did not find any significant difference (Patiri et al. 2006; Kreckel et al. 2012; Ricciardelli et al. 2014). These discrepancies suggest that further study is needed of how star formation evolves within void galaxies. However, while the SFR provides insight into the current star formation of galaxies, it does not offer information regarding their potential capacity to keep forming stars in the future. Analyzing the gas content of the galaxy, from which the stars are formed, can give insights about this matter.

There is no consensus about the atomic gas content in void galaxies. Szomoru et al. (1996) and Kreckel et al. (2012) found that the atomic gas properties of void galaxies are similar to galaxies in filaments and walls, suggested that the small-scale rather than the large-scale environment of the galaxies affects their gas content and evolution as the small-scale clustering in the voids (within a projected distance of 600 kpc and 200 km s^{-1}) is also similar to what is found in filaments and walls. However, Florez et al. (2021) found that void galaxies have higher atomic gas masses than galaxies in filaments and walls. In addition, simulations (Kereš et al. 2005) showed that there are two modes of gas accretion: in the cold accretion mode, the gas flows along the filaments into the galaxy, and it is more likely to occur in void galaxies; in the hot accretion mode, the virialised gas in the potential well of the halo falls into the inner regions of the galaxy while cooling down, this mode is more common in denser environments, such as clusters. However, it has never been observationally confirmed due to the significant difficulty in directly measuring gas accretion rates onto galaxies. Therefore, further study is needed to understand how the large-scale environment affect the gas content and gas accretion of galaxies.

While atomic gas provides insights into the gas reservoirs of the galaxy for future star formation, the molecular gas mass informs us about the fuel reservoir for the upcoming generation of stars, which is closely linked to the Star Formation Efficiency (SFE = SFR/M_{H_2}) of the galaxies. Only three previous studies have analysed the molecular gas content of void galaxies (Sage et al. 1997; Beygu et al. 2013; Das et al. 2015), and they suggested that the molecular gas properties are similar to galaxies in filaments and walls. However, these results are based on very few galaxies, between one to five objects in each study, which is not enough to draw any statistical conclusion. To better understand the effect of the large-scale environment on the molecular gas

content and SFE of galaxies, it is essential to generate larger galaxy surveys of molecular gas.

The star formation of the galaxies can be also analysed by studying the metallicity of their ISM, as it is directly correlated with its SFR (Salim et al. 2014; Duarte Puertas et al. 2022). Some studies have analysed the effect of the local environment on the gas-phase mass-metallicity relation (MZ_gR) of galaxies. Pasquali et al. (2012) found that satellite galaxies have higher gas-phase metallicities than central galaxies with the same stellar mass, more significantly at low than at high stellar masses. In addition, at a fixed stellar mass, the gas-phase metallicity of satellite galaxies increase with the halo mass (M_h) of the group, also more significantly for low-mass galaxieswithin the range $10^{11} < M_h/M_\odot < 10^{14}$. Deng (2011) found that star-forming galaxies have higher gas-phase metallicities in regions with the highest local densities. Pilyugin et al. (2017) found that late-type galaxies with higher local densities have higher gas-phase metallicities. This effect is more significant for low-mass than for high-mass galaxies. They derived the local density as the number of neighbours inside five different projected distances: $R_0 = 1$, 2, 3, 4, and 5 Mpc but they did not compare galaxies in different large-scale structures such as voids, filaments, walls and clusters. They also found that regions with the highest local ($R_0 = 1$ Mpc) densities are not necessarily associated with the highest densities on larger scales ($R_0 = 5$ Mpc), which supports that high local densities are also found in voids. This confirms that local and large-scale environments are not the same, and further comparisons are needed between galaxies in voids, filaments, walls and clusters.

Some studies have compared the MZ_gR between different large-scale environments, but there is no consensus about the metallicity properties in void galaxies. Pustilnik et al. (2011) found that dwarf void galaxies (absolute B-band magnitude, $-18.4 < M_B < -11.9$) have around 30% lower gas metallicity than galaxies in denser large-scale environments, but Kreckel et al. (2015) did not find any significant difference between dwarf galaxies in different large-scale environments. Wegner & Grogin (2008) found tentatively lower gas-phase metallicities in early-type void galaxies, but Wegner et al. (2019) did not find any significant gas-phase metallicity difference between star-forming galaxies in voids and denser environments. However, the robustness of these results is hampered by the low number of galaxies in their samples (20, 8, 26, and 33, respectively) not allowing strong conclusions. In addition, Panter et al. (2008) showed that the gas-phase metallicity of cluster galax-

ies increases with their environmental density. However, the gas-phase metallicity is only measurable for star-forming galaxies with emission lines, and are largely affected by the current star formation rate (Salim et al. 2014; Duarte Puertas et al. 2022), which only probes the star formation in last few Myr.

While the gas content, SFR, and gas-phase metallicity give insights into the current and potential star formation of galaxies, they do not give information about their historical evolution. To understand how the large-scale environment has affected the galaxy evolution it is necessary to study their stellar populations: i.e. the Star Formation History (SFH), which describes the rate at which the galaxy has assembled its stars; and the stellar metallicity, which is the accumulated fossil record of the galaxy's star formation. They can be derived from absorption lines for both active and passive galaxies. As a general estimation, Rojas et al. (2005) found that void galaxies have, on average, lower values of the 4000 Å Balmer break than galaxies in denser environments, suggesting that the stellar populations in void galaxies are younger but more sophisticated stellar population analysis is necessary to make a strong conclusion. However, our knowledge about the stellar population of galaxies in different large-scale environments remain limited.

Previous studies have analysed the SFHs of groups of galaxies to understand how the local environment influences the stellar populations of galaxies in groups and clusters. Pasquali et al. (2010) found that low-mass ($< 10^{10}$ $M_\odot$) satellite galaxies have older and more metal-rich stars than central galaxies with the same stellar mass but Gallazzi et al. (2021) and Trussler et al. (2021) found that this environmental effect weaken after separating star-forming, green valley, and quiescent galaxies. In addition, Pasquali et al. (2010) and Gallazzi et al. (2021) found that the stellar age and metallicity of central galaxies increases with the halo mass when they average for all stellar masses. However, Scholz-Díaz et al. (2022) found that this correlation is produced by the stellar-to-halo mass relation. The stellar age and metallicity of central galaxies decreases with the halo mass for a fixed stellar mass in low-mass halos ($< 10^{13.5}$ $M_\odot$). Scholz-Díaz et al. (2022) also found that their results remain when late-type and early-type galaxies are separated but Trussler et al. (2021) only find this anti-correlation for passive centrals. They interpreted this in terms of dry mergers, which increase the resulting stellar mass and halo mass but not the stellar metallicity. However, groups of galaxies are found in all the large-scale environments of the Universe, and these studies of the local environ-

ment are not reliable to extrapolate their results to galaxies in voids. Currently, if the large-scale environment affects the galaxy evolution remains unknown.

1.5 CAVITY

Numerous studies have analysed the correlation between galaxy properties and the surrounding large-scale structure of the Universe in which they reside, and they have provided evidence that voids host a distinct galaxy population compared with galaxies in denser environments. However, further research is needed as the outcomes of some of these studies have generated controversy and many aspects of the topic are still unknown. The Calar Alto Void Integral-field Treasury surveY (CAVITY)[1] aims to provide solutions on some of the previously exposed controversial topics, and to shed light on unexplored aspects of the large-scale of the Universe.

CAVITY is a legacy project of the Centro Astronómico Hispano en Andalucía (CAHA) in Calar Alto Observatory[2]. This project is generating the first statistically complete IFU data set of void galaxies. The CAVITY survey presents a well defined mother sample of around 2500 void galaxies, which are fully enclosed in the SDSS footprint within a redshift range from 0.01 to 0.05, and cover a wide range of stellar masses ($10^{8.5} \leq M_{\star}[\mathrm{M}_{\odot}] < 10^{11.0}$). The CAVITY survey aims to observe around ~ 300 of these galaxies with the PMAS-PPAK Integral Field Unit (IFU) at the Calar Alto Observatory to characterise the spatially resolved stellar populations and ionised gas content of void galaxies, together with their kinematics and dark mass assembly, along with ancillary deep optical imaging from the Isaac Newton Telescope (INT), CO emission (CO-CAVITY), and H I data (HI-CAVITY). The CO-CAVITY survey presents the first statistically significant survey of molecular gas in void galaxies. It aims to observe the CO emission lines of a around 100 CAVITY galaxies with the 30 m antenna of the Institut de Radioastronomie Millimétrique (IRAM) at Pico Veleta to characterise the molecular gas properties of void galaxies. The HI-CAVITY project has recently obtained 146.25 hours of observation with the Green Bank Telescope (GBT) in West Virginia to measure the 21 cm emission line and derive the atomic gas mass of CO-CAVITY

[1] https://cavity.caha.es/
[2] https://www.caha.es/

galaxies.

1.6 Goals

This thesis aims to study the effect of the large-scale structure on the galaxy evolution by analysing the molecular gas, SFR, SFE, SFH, and stellar metallicity of a statistically significant sample of galaxies in voids, filaments, walls, and clusters. We want to answer some questions about the void galaxies:

1. Is their molecular gas content different than in denser environments? Do their stars form with a different efficiency?
2. Are their SFHs different than in filaments, walls, and clusters?
3. Are their stellar metallicities different? What does this tell us about the way stars formed in the past?

In order to achieve these goals, we could not use the IFU data of the CAVITY project yet, but we used their sample selection, and applied full spectral fitting techniques to SDSS integrated spectra of thousands of galaxies in voids, filaments, walls, and clusters to derive their SFHs and average stellar metallicities. With respect to the molecular gas, we carried out a small (20 objects) CO pilot survey at the IRAM 30 m telescope as a preparation for the current CO-CAVITY survey with around 100 galaxies observed up to date.

1.6.1 Molecular gas

The presence (or absence) of molecular gas strongly regulates the star formation of galaxies (Leroy et al. 2008; Bigiel et al. 2011). Therefore, the molecular gas mass is a crucial parameter that allows us to quantify the potential for future star formation. However, currently there is no statistically significant sample of void galaxies with molecular gas data. Therefore, more statistics are needed to better understand how the large-scale environment affects the star formation processes and the molecular gas properties of galaxies. While the CO-CAVITY project is getting started, we present here the results of a pilot survey. We compare the molecular gas mass, SFR, and SFE in void galaxies to those galaxies in filaments and walls in order to better understand how the processes of molecular gas consumption and star formation are related to the large-scale environment.

1.6.2 Stellar populations

The study that we carry out about the SFR and molecular gas gives us information about the star formation of the galaxies in the last few Myr, and the potential of the galaxies to keep forming stars, but nothing about their past evolution. The stellar populations (i.e. stellar mass, age, and metallicity) of a galaxy give us light about its evolution. There are some works that study how the local environment affects the stellar populations of the galaxies but little is know about the large-scale environmental effect. As a preparatory study of the CAVITY project, we present the first comparison of SFHs and stellar metallicities within galaxies located in different large-scale environments. Comparing the stellar populations of galaxies in various environments, including voids, filaments, walls, and clusters, can provide valuable insights into how the large-scale environment impacts galaxy evolution.

Chapter 2

Sample selection

Contents

In this chapter we define the sample of void galaxies that we need for our study, together with the control sample of galaxies in denser environments. The size of the galaxy samples is limited to the availability of the data required for the study. This thesis is structured in two main parts: the study of molecular gas, and the stellar populations, from which we study the star formation histories and the stellar metallicities in void galaxies. Therefore, we define two different sets of galaxy samples for each part of our thesis.

For the molecular gas analysis (carried out in Chapter 3) we need galaxies with available data in SFR, molecular, and atomic gas. As sample of void galaxies we use the 78 void galaxies with atomic gas data in the Void Galaxy Survey (VGS) presented in Kreckel et al. (2012), and the 20 galaxies with molecular gas in the CO-CAVITY pilot survey (see Section 1.5), which is a sample of SDSS nearby ($0.011 < z < 0.025$) galaxies extracted from the VGS. We observe the CO emission lines of these 20 galaxies in the IRAM 30 m telescope to obtain the molecular gas data (see Section 3.1.1). The VGS galaxies have available SFR data derived from Hα emission in Beygu et al. (2016). As control sample we use 362 filament and wall galaxies with atomic gas data, and 102 galaxies with also molecular gas data. These galaxies are extracted from a combination of two H I surveys: the extended GALEX Arecibo SDSS Survey (xGASS) presented in Catinella et al. (2018), and a set of objects from the Calar Alto Legacy Integral Field Area (CALIFA) with atomic gas data collected from the literature (López-Sánchez et al. in prep.); and two H_2 surveys: the xCOLD GASS survey (Saintonge et al. 2017), and the EDGE-CALIFA survey (Bolatto et al. 2017). These surveys do not have any environmental selection criteria, so they contain galaxies in voids, filaments, walls, and cluster. We wish to compare our sample of void galaxies with galaxies in filaments and walls only, so we removed from the control sample those galaxies that inhabit voids and clusters (find more details in Section 2.1.3). The galaxies in the control sample have available SFR in the literature but are derived using different prescriptions. We explain the choice of the SFR tracer in Appendix A.2.

For the stellar population analysis (carried out throughout the chapters 4, 5 and 6) we use a sample of galaxies that has been extracted from the spectroscopic catalogue of SDSS-DR7 with redshifts $0.01 < z < 0.05$. We select as mother sample of void galaxies in our study the mother sample of the CAVITY project (see Section 1.5), with 2529 galaxies (see Section 2.2). The mother control sample is made out of 6189 galaxies in

clusters from Tempel et al. (2017), and 15000 galaxies in filaments and walls as they belong neither to voids nor to clusters (see Section 2.2.1). We consider that filaments and walls belong to the same large-scale environment (filaments & walls here after) as the number density of galaxies is very similar. After applying the spectral analysis (see Chapter 4) to these galaxies we carry out a quality control (see Section 4.5) and remove from the mother samples those galaxies with low quality spectra, Signal-to-Noise ratio (S/N) lower than 20, leaving us with 987 galaxies in voids, 6463 in filaments & walls, and 3357 in clusters for our study. Additionally, in Section 2.2.3 we define three sub-samples with the same stellar mass distribution as our sample of void galaxies.

2.1 CO-CAVITY pilot survey

2.1.1 Void Galaxy Survey

The VGS is a sample of 60 void galaxies plus 18 companions that were observed in the Westerbork Synthesis Radio Telescope (WSRT) to measure their H I 21 cm line emission. This sample has been defined from the SDSS-DR7 in a volume from redshift z = 0.003 to z = 0.030. The VGS is the first survey selected by a strictly geometric procedure based on the local spatial distribution of galaxies (Kreckel et al. 2011; Platen et al. 2011), where it is assumed that galaxies are good tracers of their surrounding density field. The relative density of a region in the Universe is calculated with the density contrast, $\delta = \Delta\rho/\rho$, where ρ is the mean density of the Universe. For the VGS, the density contrast ranges from -0.94 to -0.44 with a mean value of -0.78 (Kreckel et al. 2012), and the size of the voids spans from 16.25 Mpc to 18.64 Mpc (Kreckel et al. 2011).

The VGS galaxy selection is based on the Delaunay Tessellation Field Estimator (DTFE) algorithm (Schaap & van de Weygaert 2000; Schaap 2007; van de Weygaert & Schaap 2009), which generates a continuous density field from the spatial distribution of the SDSS galaxies. This technique keeps the anisotropic structure of the cosmic web. The WVF algorithm (Platen et al. 2007), is applied to the density field to identify the void regions. The WVF is used in geophysics to identify the basins of a landscape where the rainfall will collect. In the same way, it is applied to the DTFE density field to define the irregular and twisted voids boundaries.

The VGS galaxy selection criteria (Kreckel et al. 2011) are that

the galaxies need to be (i) located in the interior regions of voids and far from their boundaries, (ii) far from the SDSS volume limits, (iii) separated by at least $750\,\mathrm{km\,s^{-1}}$ in velocity from a foreground and background cluster to avoid Finger of God effects, and (iv) within a redshift of $0.010 < z < 0.025$ to select galaxies that are bright enough for H I observations (Kreckel et al. 2012).

The VGS has been defined without applying any colour or luminosity selection but it is affected by the SDSS completeness limit at r-Petrosian < 17.77 mag (Strauss et al. 2002; Argudo-Fernández et al. 2015). This means that the sample is progressively less sensitive to faint objects with increasing redshift. The SDSS completeness limit corresponds to an absolute magnitude of $M_r = -17.4$ mag at the maximum redshift of our sample ($z = 0.025$). For fainter objects, the sample is therefore not entirely complete. However, given the type of study that we carry out and given that the redshift range of the VGS sample is small, we do not expect this to be a severe problem for this work.

2.1.2 CO sub-sample of the VGS

We chose 20 galaxies for the CO observations (the CO-VGS sub-sample) from the galaxies in the VGS that were observed in H I by Kreckel et al. (2012). We based our selection on the SFR and $M_\star$ from the Max-Planck-Institut für Astrophysik and Johns Hopkins University (MPA-JHU) survey (Kauffmann et al. 2003; Brinchmann et al. 2004; Salim et al. 2007). We dropped 15 objects (2 main VGS objects and 13 companions) with no data for the SFR or $M_\star$ in MPA-JHU. We estimated for each galaxy the expected molecular gas mass using the measured SFR, and assuming SFE $= \mathrm{SFR}/M_{\mathrm{H_2}} = 10^{-9}\,\mathrm{yr^{-1}}$ (Saintonge et al. 2011). From the predicted $M_{\mathrm{H_2}}$, we derived the expected velocity-integrated CO(1 − 0) intensity $I_{\mathrm{CO}(1-0)}$ with the IRAM 30 m telescope adopting a Galactic CO-to-H_2 conversion factor, $\alpha_{\mathrm{CO}} = 3.2\,\mathrm{M_\odot(K\,km\,s^{-1}pc^2)^{-1}}$ (Bolatto et al. 2013). Based on this estimation, we selected the galaxies with an expected intensity of $I_{\mathrm{CO}(1-0)} \geqslant 0.6\,\mathrm{Kkm\,s^{-1}}$, a limit below which the observations become prohibitively long. tThus, we excluded those objects that are expected to be beyond the detecting capacity of the IRAM 30 m telescope. In addition, we dropped one galaxy (VGS07) with relatively low stellar mass ($10^{7.7}\,\mathrm{M_\odot}$) in order to exclude faint and low-metallicity objects for which the detection of CO is difficult and the determination of the $M_{\mathrm{H_2}}$ is affected by the uncertainties in the α_{CO} factor (Bolatto et al.

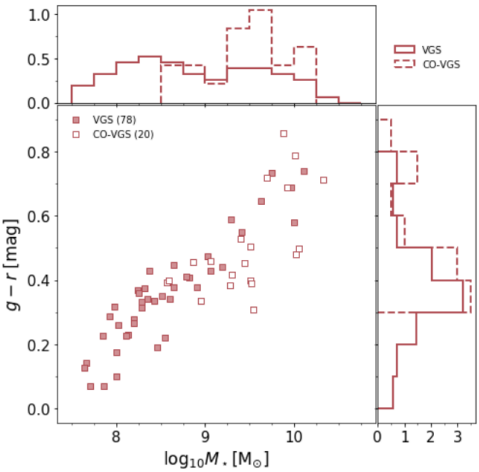

Figure 2.1: Colour vs. stellar mass diagram with normalised histograms for the VGS and the CO-VGS sub-sample. The number of galaxies for each sample is shown in the legend.

2013).

In Figure 2.1 we show the CMD of the CO-VGS and the entire VGS. The CO-VGS $M_\star$ ranges from $10^{8.5}$ to $10^{10.3}\,M_\odot$, $g-r$ colour from 0.30 to 0.86 mag, SFR from $10^{-1.0}$ to $10^{0.7}\,M_\odot\,yr^{-1}$, and redshift from z = 0.011 to z = 0.025. The CO-VGS metallicity range is $8.44 < 12 + \log(O/H) < 9.10$ (values taken from Tremonti et al. 2004). The values of only four galaxies are lower than solar (8.66). Thus α_{CO} was set to the Galactic conversion factor (without considering the helium mass) of $3.2\,M_\odot(K\,km\,s^{-1}pc^2)^{-1}$ (Bolatto et al. 2013).

We need to be aware that our selection criterion biases our sample against galaxies with a very low SFR (e.g. dwarf or elliptical galaxies). In addition, we might also miss galaxies with a low SFE that would have a higher molecular gas mass than we estimated and that might therefore be erroneously excluded from our sample.

2.1.3 Control sample

From the 1690 galaxies in the xCOLD GASS and López-Sánchez et al. (in prep.) samples, we first removed galaxies inhabiting voids and clusters by excluding objects listed in the Pan et al. (2012) void galaxy survey and the Tempel et al. (2017) group of galaxies survey (considering galaxies in groups with more than 30 members as a cluster galaxies, Abell et al. 1989).

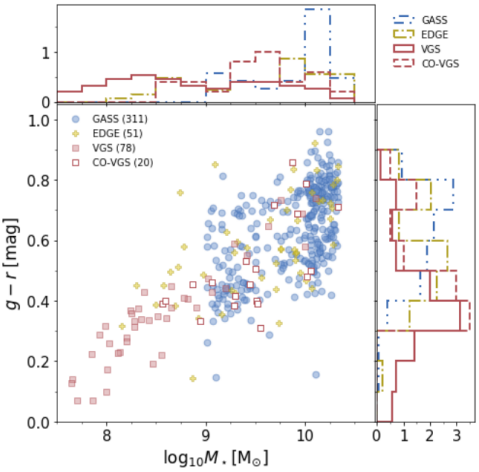

Figure 2.2: Colour vs. stellar mass diagram with normalised histograms for the VGS and the CCS. The number of galaxies for each sample is shown in the legend.

We then generated two sub-samples: one to compare with the entire VGS, and the other to compare with the CO-VGS. For the first sub-sample, called the Complete Control Sample (CCS), we selected 362 galaxies that lie within the $M_\star$ and $g-r$ colour ranges of the entire VGS ($10^{7.7} < M_\star/\mathrm{M}_\odot < 10^{10.3}$ and $0.07 < \mathrm{g-r} < 0.86$). For the second sub-sample, which we call CO Control Sample (CO-CS), we selected 102 galaxies with molecular gas data that lie within the $M_\star$, $g-r$ colour, and SFR ranges of the CO-VGS ($10^{8.5} < M_\star/\mathrm{M}_\odot < 10^{10.3}$, $0.30 < g-r < 0.86$, and $\mathrm{SFR} > 0.1\ \mathrm{M}_\odot\ \mathrm{yr}^{-1}$). Figures 2.2 and 2.3 show the colour-stellar mass distribution of the VGS and the CO-VGS, respectively. The CCS and CO-CS do not cover the VGS and CO-VGS $M_\star$ ranges below $10^{8.0}\,\mathrm{M}_\odot$ and $10^{9.0}\,\mathrm{M}_\odot$, respectively, thus the statistical comparison is only representative above these values. There are other H_2 samples with low stellar mass galaxies (Rémy-Ruyer et al. 2014; Hunt et al. 2020; Castignani et al. 2021), but they were not useful for our study because there are only very few galaxies with $10^{8.5}\,\mathrm{M}_\odot < M_\star < 10^{9.0}\,\mathrm{M}_\odot$, and the M_{H_2} values are highly dispersed. It is difficult to obtain M_{H_2} for galaxies with $M_\star < 10^{9.0}\,\mathrm{M}_\odot$ because their metallicities are low, which translates into low CO emission and high uncertainties for α_{CO}.

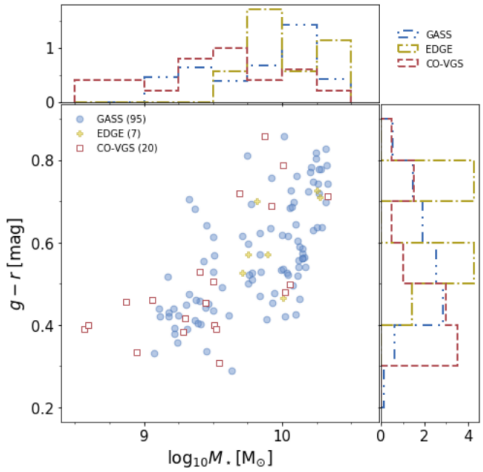

Figure 2.3: Colour vs. stellar mass diagram with normalised histograms for the CO-VGS and the CO-CS. The number of galaxies for each sample is shown in the legend.

xGASS and xCOLD GASS surveys

The xGASS (Catinella et al. 2018) is a H I survey of 1179 galaxies selected in a stellar mass range of $10^{9.0}\,\mathrm{M}_\odot < M_\star < 10^{11.5}\,\mathrm{M}_\odot$ and a redshift range of $0.01 < z < 0.05$. The xCOLD GASS (Saintonge et al. 2017) is an IRAM 30 m telescope H_2 legacy survey of 532 nearby galaxies ($0.01 < z < 0.05$) with stellar masses between $10^{9.0}$ and $10^{11.5}\,\mathrm{M}_\odot$. From the xGASS (1179 galaxies), we removed the 333 void galaxies contained in Pan et al. (2012) and the 69 galaxies classified in Tempel et al. (2017) as cluster galaxies. We selected 311 galaxies for the CCS (with H I data and lying within the $M_\star$ and $g-r$ colour ranges of the VGS). For the CO-CS, we selected 95 galaxies (with H_2 data and lying within the $M_\star$, $g-r$ colour, and SFR ranges of the CO-VGS) from xCOLD GASS and xGASS after removing void and cluster galaxies. Hereafter, we refer to the control galaxies selected from xGASS and xCOLD GASS as GASS galaxies.

EDGE-CALIFA survey

EDGE-CALIFA (Bolatto et al. 2017) is a CARMA H_2 survey of 126 galaxies selected from the CALIFA (Sánchez et al. 2012) survey that have high WISE 12 μm flux and are centred around 12 hours of right ascension. CALIFA is a diameter-selected survey ($45 < D_{25}/\mathrm{arsec} < 80$) of 600 galaxies in the redshift range of $0.005 < z < 0.030$ and the $M_\star$

range of $10^{9.4}\,M_\odot < M_\star < 10^{11.4}\,M_\odot$. The metallicity is higher than solar ($8.71 < 12 + \log(O/H) < 9.25$). We used H I data from López-Sánchez et al. (in prep.), who searched the literature for H I data for CALIFA galaxies and found valid H I data for 511 objects, we call this sample HI-CALIFA (find more details in Section 3.1.2).

For the CCS selection (which does not require CO data), we started from the entire HI-CALIFA sample (511 galaxies) and removed 239 objects with no data in MPA-JHU, 91 void galaxies contained in Pan et al. (2012), and 8 galaxies classified in Tempel et al. (2017) as cluster galaxies. Finally, we selected the objects that lied within the VGS colour and stellar mass ranges. We obtained 51 galaxies for the CCS. For the CO-CS, we started from these 51 objects and selected the galaxies with CO data in EDGE-CALIFA that lied within the CO-VGS colour, stellar mass, and SFR ranges. We obtained 7 objects for the CO-CS. Hereafter, we refer to this sample as EDGE galaxies.

2.2 CAVITY mother sample

The CAVITY survey presents a well defined selection of void galaxies, which are fully enclosed in the SDSS footprint within a redshift range from 0.01 to 0.05, and cover a wide range of stellar masses ($10^{8.5} \leq M_\star/M_\odot < 10^{11.0}$). The mother sample of the CAVITY project comprises 2529 galaxies, which is a sub-sample of the Pan et al. (2012) catalogue of SDSS void galaxies. Pan et al. (2012) applied the VoidFinder algorithm (El-Ad & Piran 1997; Hoyle & Vogeley 2002) to the distribution of SDSS galaxies with redshifts $z < 0.107$, and found 79947 void galaxies inside 1055 cosmic voids with typical density contrast $\delta = -0.94 \pm 0.03$ and radii larger than 10 h^{-1} Mpc.

The VoidFinder algorithm classifies as potential void galaxies those with their third nearest neighbour distance $d_3 > 6.3\,h^{-1}$ Mpc and remove them from the SDSS galaxy sample, leaving only galaxies in denser large-scale environments. Then, it generates a space grid of cubic cells of size $5\,h^{-1}$ Mpc, identifies the empty ones as potential voids, and fits maximal spheres inside these empty regions. Spheres overlapping more than 10% are unified in the same void, and galaxies inside these spheres are classified as void galaxies. The spheres with the same volume of the void defines its effective radius. However, voids are not perfectly spherical and some void galaxies are located beyond the effective radius of its void. There are many algorithms to find voids

and other large-scale structures such as filaments, walls, and clusters. These algorithms differ in the classification of the galaxies into different large-scale structures, specially when they are very close to the limit of the void, and some galaxies may have been potentially mis-classified as void galaxies.

The CAVITY collaboration (Pérez et al. in prep.) reduced the redshift range ($0.01 < z < 0.05$) to concentrate on nearby galaxies that are observable with PMAS-PPAK, chose 15 voids with more than 20 galaxies each to observe around 300 galaxies distributed along the entire right ascension range of the SDSS, and selected galaxies in the inner region of the voids (i.e. inside the 80% of the void's effective radius) to avoid the possible inclusion of galaxies that are inhabiting or affected by denser environments. Additionally, the CAVITY collaboration carried out a visual inspection of the galaxies, and removed from the sample the duplicated objects, and the spectra integrated in H II regions, not in the centre of the galaxy.

2.2.1 Control sample

The aim of this study is to compare the stellar populations between galaxies in voids and galaxies in denser environments. Therefore, the control sample comprises galaxies inhabiting large-scale environments in the nearby Universe that are denser than voids: filaments, walls, and clusters. We define two control samples: one of galaxies in clusters, and the other one of galaxies in filaments & walls.

The mother sample of galaxies in clusters is extracted from the Tempel et al. (2017) catalogue of groups of SDSS galaxies that are not contained in the complete catalogue of void galaxies of Pan et al. (2012), and are located within the redshift range of the CAVITY mother sample ($0.01 < z < 0.05$). Galaxies in groups with ≥ 30 members are selected as cluster galaxies (Abell et al. 1989). With these selection criteria, our mother sample of cluster galaxies contains 6189 galaxies.

The mother sample of galaxies in filaments & walls in this study is extracted from all the SDSS galaxies (109945) within the same redshift range as the CAVITY mother sample ($0.01 < z < 0.05$) that are neither in the complete catalogue of void galaxies of Pan et al. (2012) nor in the mother sample of cluster galaxies defined above. To save computational time in the stellar population analysis (see Chapter 4), we select a sub-sample of 15000 galaxies in filaments & walls preserving similar stellar mass, $g-r$ colour, and redshift distributions (two-sample

Kolmogorov–Smirnov (KS) test [1] test with p-values > 0.95) than the original sample of galaxies in filaments & walls directly extracted from SDSS.

2.2.2 Sample characteristics

These three samples are magnitude-limited due to the SDSS completeness limit at r-Petrosian <17.77 mag (Strauss et al. 2002; Argudo-Fernández et al. 2015). This means that the sample is progressively less sensitive to faint objects with increasing redshift. However, given the type of study that we carry out, and given the narrow redshift range of the CAVITY sample, we do not expect this to be a severe problem for this work.

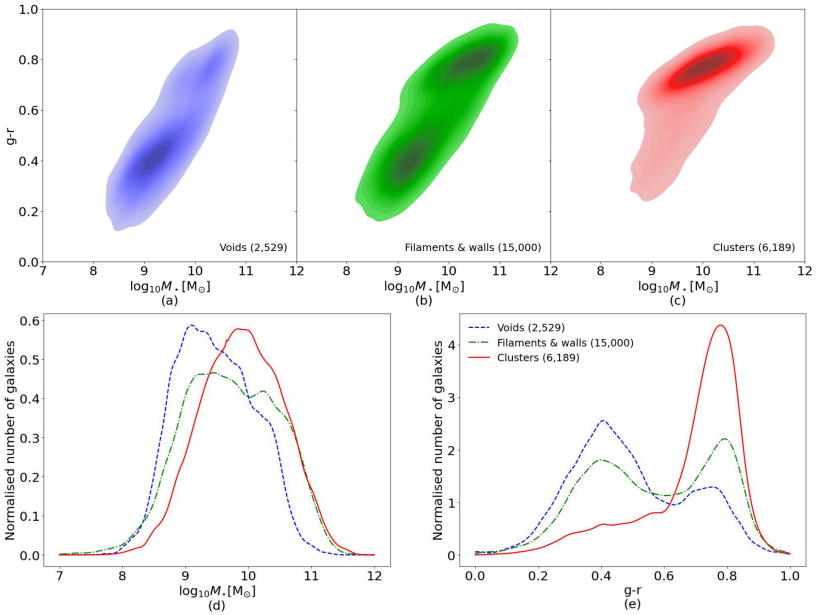

Figure 2.4: **Colour and stellar mass distribution before the quality control.** Colour vs. stellar mass diagram for galaxies in voids (a), filaments (b), and clusters (c). Normalised distributions of the stellar mass (d) and $g - r$ colour (e) for galaxies in voids (blue dashed line), filaments & walls (green dot-dashed line), and clusters (red solid line).

[1] The KS test evaluates whether two samples come from the same mother sample. A p-value below 0.05 indicates, with a reliability higher than 95%, that both samples come from different mother samples, whereas for higher p-values, no firm conclusions can be drawn.

In Figure 2.4 we compare colour and stellar mass distributions between the three samples. We see that part of the void galaxies are located in the red sequence but they mainly populate the blue cloud. This distribution is more balanced in filaments & walls where galaxies are equally distributed between the red sequence and the blue cloud. However, the majority of cluster galaxies cover the red sequence, and only a small part of them are distributed over the blue cloud. As it has been observed before (Rojas et al. 2004, 2005; Patiri et al. 2006; Park et al. 2007; Hoyle et al. 2012; Kreckel et al. 2012; Ricciardelli et al. 2014; Beygu et al. 2016; Florez et al. 2021) void galaxies are, on average, bluer and less massive than galaxies in filaments, walls, and clusters.

We carry out our analysis and quality control cuts (see Chapter 4) to remove some galaxies with bad-fitted spectra (mainly low mass objects from the blue cloud with S/N < 20) that modify the distributions (see Figure 2.5). We lose 1,542 (61%) galaxies from voids; 8,537 (57%) from filaments & walls; and 2,832 (46%) from clusters. The mean stellar mass of the removed galaxies are similar in the three environments ($10^{9.2\pm0.1}$ $M_\odot$ in voids, $10^{9.3\pm0.1}$ $M_\odot$ in filaments & walls and $10^{9.5\pm0.1}$ $M_\odot$ in clusters). Finally, after this quality control we are left with 987 galaxies in voids, 6,463 in filaments & walls, and 3,357 in clusters for our study. These are the main samples that we use in our analysis of chapters 5 and 6.

2.2.3 Stellar mass adjusted sample

As we see in Figures 2.4 and 2.5, the stellar mass distribution of these samples is not the same even after the quality control, void galaxies are on average less massive than galaxies in denser environments. Therefore, in order to minimise the effect that this might generate in our results, we define five stellar mass bins of 0.5 dex between $10^{8.5}$ and $10^{11.0}$ $M_\odot$, and we generate two control sub-samples with the same stellar mass distribution as our void galaxy sample inside every stellar mass bin. We apply the two-sample KS test with p-values above 0.95 to ensure that the accuracy with which the stellar mass distributions are matched. We have not been able to extend the bins at lower or higher stellar masses because the number of galaxies beyond these limits was not enough, in at least one of the environments, to define sub-samples with similar stellar mass distributions applying the KS test. We are left with 978 void galaxies (we lose 9 void galaxies with masses that are

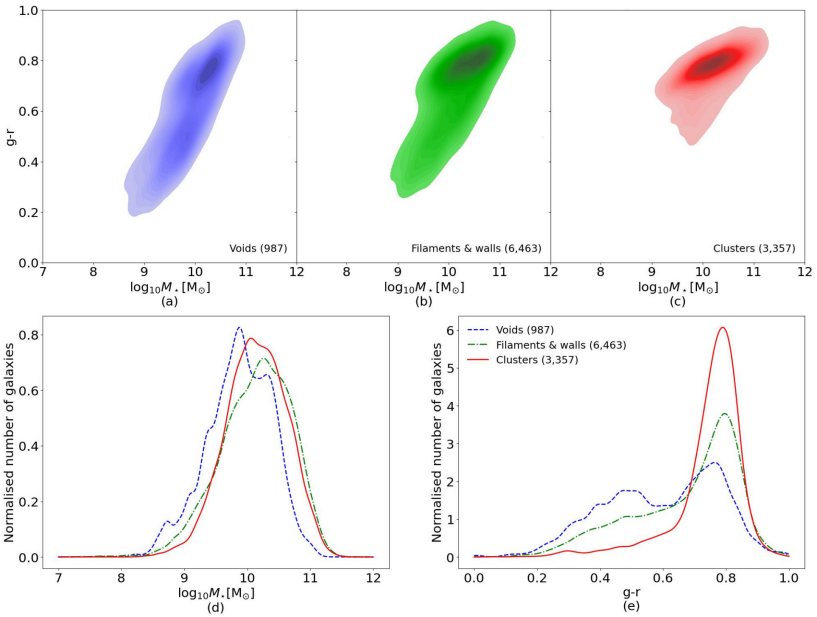

Figure 2.5: **Colour and stellar mass distribution after the quality control.** Colour vs. stellar mass diagram for galaxies in voids (a), filaments (b), and clusters (c). Normalised distributions of the stellar mass (d) and $g-r$ colour (e) for galaxies in voids (blue dashed line), filaments & walls (green dot-dashed line), and clusters (red solid line).

outside the stellar mass bins), 4800 filament & wall galaxies, and 2570 cluster galaxies. These are the samples that we use in our analysis of chapters 5 and 6, when we refer to samples with similar stellar mass distributions.

Chapter 3

Molecular gas

Contents

We present the first molecular gas mass survey of void galaxies. We compare these new data together with data for the atomic gas mass ($M_{\rm HI}$) and SFR from the literature to those of galaxies in filaments and walls in order to better understand how molecular gas and star formation are related to the large-scale environment. We observed with the IRAM 30 m telescope the CO$(1-0)$ and CO$(2-1)$ emission of the CO-CAVITY pilot survey, which comprises 20 void galaxies selected from the VGS (see Section 2.1), with a stellar mass range from $10^{8.5}$ to $10^{10.3}$M$_\odot$. We detected 15 objects in at least one CO line. We compared the molecular gas mass ($M_{\rm H_2}$), the SFE, the atomic gas mass, the molecular-to-atomic gas mass ratio, and the specific Star Formation Rate (sSFR = SFR/$M_\star$) of the void galaxies with two control samples of galaxies in filaments and walls, selected from xCOLD GASS and EDGE-CALIFA (see Section 2.1.3), for different stellar mass bins.

This chapter is based in the study that we carried out in Domínguez-Gómez et al. (2022) and is organised into four sections and three appendices. In Section 3.1 we describe the observations and data reduction of the CO-CAVITY pilot survey, together with other data obtained from literature. In Section 3.2 we carry out a comparison of different properties (such as sSFR, $M_{\rm H_2}$, SFE, $M_{\rm HI}$, and molecular-to-atomic gas mass ratio) between galaxies in voids and galaxies in filaments and walls. In Section 3.3 we discuss our results and compare them with previous studies. In Section 3.4 we summarise our conclusions. In Appendix A.1 we estimate the theoretically expected CO line ratios. In Appendix A.2 we compare different SFR tracers for galaxies in our samples. In Appendix A.3 we show the CO line spectra for the 20 observed galaxies.

3.1 Data

3.1.1 CO-CAVITY pilot survey

Optical properties and atomic gas mass

For the VGS we used photometric data from the SDSS-DR16, and spectrometric properties from the SDSS-DR16 & MPA-JHU database (Kauffmann et al. 2003; Brinchmann et al. 2004; Tremonti et al. 2004; Salim et al. 2007). In particular, we used redshift (z), apparent dereddened magnitudes in r and g bands, r-Petrosian R_{90}, and $M_\star$.

For the SFR, we did not use the MPA-JHU values because there

are systematic discrepancies between them and other SFR tracers, in particular for low SFRs (SFR $\lesssim 10^{-1.0}\,M_\odot\,yr^{-1}$) and large radii ($R_{90} \gtrsim$ 15 arcsec). A detailed analysis is given in Appendix A.2.

Instead, we used the SFR derived by Beygu et al. (2016) from Hα maps obtained at the 2.4 m Hiltner Telescope with the Echelle CCD in direct mode. The Hα fluxes measured from the calibrated maps were extinction corrected based on the Balmer decrement derived from the central 3 arcsec spectra from the MPA-JHA DR7 catalogue and, in some cases, on infrared data from WISE and the 4000 Å break, $D_n(4000)$. The SFR was then calculated following Hao et al. (2011) and Murphy et al. (2011) as[1]

$$\mathrm{SFR}[M_\odot\ yr^{-1}] = 5.4 \times 10^{-42} L_{H\alpha}[erg\,s^{-1}]. \quad (3.1)$$

The SFR ranges of the VGS ($10^{-2.7} < \mathrm{SFR}/(M_\odot\ yr^{-1}) < 10^{0.8}$) and the CO-VGS sub-sample ($10^{-2.1} < \mathrm{SFR}/(M_\odot\ yr^{-1}) < 10^{0.8}$) derived in this way are slightly different from the SFR ranges derived from the MPA-JHU SFR tracer (see Section 2.1.2).

Observations of the H I 21 cm line were obtained using the Westerbork Synthesis Radio Telescope (WSRT) for 73 of the 78 VGS galaxies. They were presented in Kreckel et al. (2012), and the reduction of these data was further explained in Kreckel et al. (2011). Kreckel et al. (2012) derived the atomic gas mass (M_{HI}) using the luminosity distance calculated from the H I redshift. We re-scaled M_{HI} to the SDSS redshift luminosity distance that we use in the present thesis. The data are listed in Tables 3.1 and 3.2 for the main galaxies in the VGS and in Tables 3.3 and 3.4 for the VGS companions.

CO observations and data reduction

The observations were carried out at the IRAM 30 m telescope in three different periods (18 - 23 June, 11 - 22 July, and 17 - 18 October 2019). We observed the $^{12}CO(1-0)$ (rest frame frequency 115.2712 GHz) emission line in parallel with the $^{12}CO(2-1)$ (rest frame frequency 230.5380 GHz) emission line.

The EMIR dual-polarisation receiver was combined with two autocorrelators: FTS (with a frequency resolution of 0.195 MHz, corresponding to a velocity resolution of 0.5 km s^{-1} at 113 GHz), and WILMA (with frequency of 2 MHz and velocity resolutions of 5.3 km s^{-1}).

[1]Note that this equation has an unit erratum ($M_\odot$ instead of $M_\odot\ yr^{-1}$) in Domínguez-Gómez et al. (2022), we correct it here.

Name	g [mag] (1)	r [mag] (2)	$g-r$ [mag] (3)	r_{25} [arcsec] (4)	$i^{(*)}$ [°] (5)
VGS01	17.87	17.42	0.45	9.8	60.0
VGS02	17.72	17.34	0.38	11.8	47.0
VGS03	17.86	17.43	0.43	8.4	55.0
VGS04	17.22	16.76	0.46	7.0	46.0
VGS05	15.68	14.94	0.74	23.0	37.0
VGS06	17.67	17.34	0.33	12.5	71.0
VGS07	17.45	17.38	0.07	11.2	50.0
VGS08	24.57	22.87	1.71	1.5	51.0
VGS09	17.71	17.48	0.23	19.4	68.0
VGS10	17.20	16.86	0.34	1.8	87.0
VGS11	16.44	15.98	0.46	19.9	18.0
VGS12	17.64	17.36	0.28	11.1	29.0
VGS13	16.77	16.30	0.47	14.4	68.0
VGS14	17.00	16.73	0.26	18.8	67.0
VGS15	15.85	15.30	0.55	31.9	-
VGS16	17.81	17.52	0.29	10.4	60.0
VGS17	20.97	21.09	-0.12	1.8	-
VGS18	17.82	17.44	0.38	17.6	82.0
VGS19	16.89	16.50	0.39	9.0	60.0
VGS20	18.15	18.01	0.14	5.2	-
VGS21	15.49	14.81	0.69	43.8	79.0
VGS22	17.81	17.50	0.31	6.6	63.0
VGS23	15.53	15.14	0.38	22.4	49.0
VGS24	15.45	14.87	0.58	16.4	35.0
VGS25	17.83	17.60	0.23	9.7	43.0
VGS26	16.74	16.33	0.42	20.0	69.0
VGS27	18.04	17.72	0.32	9.1	55.0
VGS28	18.18	17.54	0.64	19.5	54.0
VGS29	16.60	16.23	0.38	15.6	-
VGS30	18.13	17.96	0.17	18.8	77.0
VGS31	15.01	14.70	0.31	15.5	52.0
VGS32	14.57	14.12	0.45	27.0	46.0
VGS33	17.97	17.61	0.37	8.9	60.0
VGS34	16.11	15.26	0.86	16.7	50.0
VGS35	16.74	16.33	0.41	13.2	65.0
VGS36	16.74	16.41	0.33	18.2	79.0
VGS37	17.38	17.04	0.34	23.1	67.0
VGS38	17.05	16.98	0.07	16.9	39.0
VGS39	16.00	15.21	0.79	15.4	66.0
VGS40	17.25	16.82	0.43	9.0	42.0
VGS41	17.60	17.19	0.41	6.2	29.0
VGS42	16.33	15.80	0.53	14.8	58.0
VGS43	18.16	17.83	0.33	7.3	30.0
VGS44	15.20	14.80	0.40	17.1	31.0
VGS45	17.61	17.35	0.26	20.8	66.0
VGS46	17.13	16.78	0.35	14.1	71.0
VGS47	15.23	14.51	0.71	29.5	72.0
VGS48	17.61	17.02	0.59	11.4	-
VGS49	15.85	15.46	0.39	12.3	40.0
VGS50	16.00	15.32	0.69	12.6	83.0
VGS51	17.25	17.03	0.22	12.8	63.0
VGS52	17.79	17.56	0.23	16.2	70.0
VGS53	16.12	15.61	0.50	20.5	64.0
VGS54	16.80	16.15	0.65	22.5	80.0
VGS55	16.63	16.19	0.44	18.1	55.0
VGS56	16.44	15.72	0.72	14.0	59.0
VGS57	14.94	14.44	0.50	21.5	30.0
VGS58	16.05	15.65	0.40	21.3	38.0
VGS59	18.12	17.76	0.36	12.7	67.0
VGS60	16.45	15.72	0.73	19.2	81.0

Table 3.1: **Photometric properties for the VGS.** Columns (1) and (2) are the dereddened g and r-band magnitudes from SDSS. Column (3) is the dereddened $g-r$ colour. Column (4) is the radius of the galaxy at isophote 25, calculated using the r-Petrosian R_{90} in the r band from SDSS as $r_{25} = 1.7 \times R_{90}$ (see Section 3.1.1). Column (5) is the galaxy inclination from Kreckel et al. (2012). (*) We only need the inclination for galaxies observed in CO to calculate the aperture correction factor.

Name	$\log_{10} M_\star$ [$M_\odot$] (1)	$\log_{10} M_{HI}$ [$M_\odot$] (2)	$\log_{10}$ SFR [$M_\odot$ yr^{-1}] (3)	z (4)	D_L [Mpc] (5)
VGS01	8.65± 0.10	< 8.32	-1.28 ± 0.11	0.019	80.5
VGS02	8.65± 0.08	8.83 ± 0.12	-1.57 ± 0.14	0.023	98.3
VGS03	8.38± 0.09	< 8.27	-1.96 ± 0.12	0.017	73.2
VGS04	8.87± 0.08	< 8.23	-1.13 ± 0.04	0.016	70.4
VGS05	10.11± 0.09	< 8.51	-1.38 ± 0.29	0.022	97.7
VGS06	8.42± 0.06	9.20 ± 0.07	-1.17 ± 0.10	0.023	100.4
VGS07	7.71± 0.19	8.93 ± 0.04	-1.10 ± 0.03	0.016	70.5
VGS08	-	8.60 ± 0.16	-1.52 ± 0.13	0.020	85.3
VGS09	7.85± 0.05	9.03 ± 0.04	-1.43 ± 0.04	0.013	56.2
VGS10	8.35± 0.06	9.17 ± 0.06	-1.59 ± 0.02	0.016	68.4
VGS11	9.06± 0.08	9.35 ± 0.04	-2.05 ± 0.24	0.016	71.5
VGS12	8.20± 0.05	9.48 ± 0.06	-1.35 ± 0.13	0.018	77.3
VGS13	9.03± 0.08	9.11 ± 0.08	-1.14 ± 0.14	0.019	83.1
VGS14	8.20± 0.06	8.81 ± 0.07	-1.74 ± 0.07	0.013	56.9
VGS15	9.41± 0.09	-	-0.70 ± 0.32	0.019	82.9
VGS16	7.93± 0.06	< 8.06	-2.10 ± 0.05	0.013	57.6
VGS17	-	-	-1.52 ± 0.09	0.011	46.2
VGS18	8.32± 0.07	8.61 ± 0.12	-2.70 ± 0.00	0.016	71.0
VGS19	8.57± 0.08	8.50 ± 0.10	-1.25 ± 0.09	0.014	62.6
VGS20	7.66± 0.13	-	-1.15 ± 0.06	0.017	72.1
VGS21	9.97± 0.09	9.34 ± 0.07	-0.64 ± 0.34	0.017	75.3
VGS22	8.28± 0.06	< 8.42	-1.66 ± 0.06	0.019	83.3
VGS23	9.28± 0.08	9.60 ± 0.05	-0.98 ± 0.12	0.017	72.4
VGS24	10.00± 0.10	< 8.53	-0.08 ± 0.43	0.023	101.2
VGS25	8.14± 0.05	8.24 ± 0.16	-0.95 ± 0.08	0.019	82.6
VGS26	9.30± 0.11	9.18 ± 0.09	-1.10 ± 0.16	0.023	101.1
VGS27	7.98± 0.06	8.54 ± 0.09	-2.22 ± 0.00	0.015	64.7
VGS28	-	< 8.22	-	0.015	66.2
VGS29	8.91± 0.07	-	-1.05 ± 0.14	0.020	87.1
VGS30	8.00± 0.07	8.77 ± 0.07	-2.30 ± 0.17	0.019	84.5
VGS31	9.55± 0.09	9.31 ± 0.06	0.31 ± 0.00	0.021	91.0
VGS32	9.44± 0.08	9.59 ± 0.05	-0.64 ± 0.08	0.012	51.1
VGS33	8.24± 0.07	8.93 ± 0.09	-	0.018	79.2
VGS34	9.88± 0.10	9.39 ± 0.05	-	0.017	71.7
VGS35	8.82± 0.08	9.03 ± 0.05	-1.07 ± 0.16	0.017	75.1
VGS36	8.95± 0.07	9.31 ± 0.06	-0.80 ± 0.14	0.022	97.6
VGS37	8.61± 0.07	9.13 ± 0.06	-1.36 ± 0.11	0.019	84.1
VGS38	7.86± 0.10	9.03 ± 0.03	-1.30 ± 0.00	0.014	59.8
VGS39	10.01± 0.10	< 8.41	-0.85 ± 0.16	0.019	82.7
VGS40	9.07± 0.08	8.79 ± 0.10	-0.73 ± 0.10	0.024	103.4
VGS41	8.78± 0.08	< 8.46	-1.09 ± 0.12	0.023	101.9
VGS42	9.40± 0.09	8.61 ± 0.16	-0.82 ± 0.15	0.019	81.5
VGS43	8.28± 0.07	< 8.46	-1.59 ± 0.13	0.021	93.4
VGS44	9.51± 0.12	8.69 ± 0.10	-0.21 ± 0.10	0.018	76.6
VGS45	8.02± 0.06	8.55 ± 0.16	-2.22 ± 0.00	0.015	63.0
VGS46	8.51± 0.08	8.75 ± 0.13	-1.35 ± 0.04	0.016	69.0
VGS47	10.33± 0.09	9.12 ± 0.09	-0.10 ± 0.18	0.022	96.5
VGS48	9.29± 0.10	-	-1.12 ± 0.19	0.025	109.0
VGS49	9.52± 0.10	< 8.56	-0.22 ± 0.09	0.025	108.8
VGS50	9.92± 0.09	9.74 ± 0.06	-0.66 ± 0.16	0.020	88.6
VGS51	8.55± 0.05	9.30 ± 0.05	-0.31 ± 0.04	0.025	110.5
VGS52	8.11± 0.07	8.95 ± 0.11	-1.70 ± 0.20	0.018	78.2
VGS53	9.50± 0.09	8.72 ± 0.14	-0.64 ± 0.14	0.021	93.5
VGS54	9.63± 0.09	9.55 ± 0.05	-0.76 ± 0.12	0.024	104.2
VGS55	9.20± 0.07	9.25 ± 0.09	-0.83 ± 0.09	0.025	109.8
VGS56	9.69± 0.10	< 8.43	-0.63 ± 0.16	0.019	81.3
VGS57	10.06± 0.11	8.81 ± 0.10	0.23 ± 0.07	0.022	96.6
VGS58	8.59± 0.06	8.87 ± 0.04	-1.34 ± 0.08	0.012	49.8
VGS59	8.26± 0.07	< 8.41	-1.85 ± 0.06	0.019	82.7
VGS60	9.75± 0.09	8.41 ± 0.27	-0.94 ± 0.12	0.020	85.4

Table 3.2: **Spectrometric properties for the VGS.** Column (1) is the stellar mass from MPA-JHU (Kauffmann et al. 2003; Salim et al. 2007). Column (2) is the atomic gas mass from WSRT (Kreckel et al. 2012); it has been re-scaled to the luminosity distance in Column (5). Column (3) is the Hα based SFR from Beygu et al. (2016). Column (4) is the redshift from MPA-JHU. Column (5) is the luminosity distance.

Name	g [mag] (1)	r [mag] (2)	$g-r$ [mag] (3)	r_{25} [arcsec] (4)	$i^{(*)}$ [°] (5)
VGS07a	21.48	21.91	-0.43	8.5	-
VGS09a	23.46	23.52	-0.06	2.2	-
VGS10a	22.11	21.77	0.33	2.2	-
VGS26a	14.16	13.67	0.49	38.5	-
VGS30a	18.67	18.41	0.26	16.7	-
VGS31a	14.73	14.25	0.48	30.1	60.0
VGS31b	16.93	16.74	0.19	10.8	-
VGS34a	20.38	20.28	0.10	5.6	-
VGS36a	19.88	19.88	-0.00	2.5	-
VGS37a	16.57	16.22	0.35	16.9	-
VGS38a	17.69	17.57	0.13	7.8	-
VGS38b	19.03	18.86	0.17	9.8	-
VGS39a	19.39	19.44	-0.05	6.7	-
VGS51a	22.28	20.70	1.58	5.5	-
VGS53a	17.61	16.65	0.96	19.1	-
VGS54a	19.32	18.98	0.34	11.2	-
VGS56a	19.19	18.90	0.29	7.9	-
VGS57a	17.85	17.75	0.10	7.7	-

Table 3.3: **Photometric properties for the VGS companions.** Same as Figure 3.1 but for the companion galaxies inside the VGS. Column (5) is the galaxy inclination from HyperLEDA; there is no inclination data for VGS companions in Kreckel et al. (2012). (*) We only need the inclination for galaxies observed in CO to calculate the aperture correction factor.

We used the wobbler-switching method for the sky subtraction with a wobbler throw of 60-80 arcsec. This was chosen for each individual galaxy, checking their optical images (SDSS g-band) to ensure that the off-position was empty of emission.

The bandwidths of the receiver (EMIR 16 GHz) and the backends (FTS 8 GHz, and WILMA 4 GHz) are wide enough to encompass the redshifted CO lines within one centrally tuned frequency setup (even though in the case of WILMA, some of the CO(2-1) lines lie very close to the edge of the bandwidth). The CO-VGS redshift ranges from z = 0.011 to z = 0.025, the recession velocities (optical convention) from 3454 to 7446 km s^{-1}, and the redshifted frequencies range from 112 to 114 GHz for CO$(1-0)$ and from 225 to 228 GHz for CO$(2-1)$. According to this, the backends were tuned to an intermediate recession velocity of 5200 km s^{-1}, which translates into redshifted frequencies of 113.3059 GHz for CO$(1-0)$ and 226.6074 GHz for CO$(2-1)$. We used the FTS spectra in this study because of their broader bandwidth and took the WILMA spectra only as a backup.

Weather conditions were generally good for all the observations, except for 22 June, when the pointing discrepancy was up to 10 arcsec. After removing this data set, the mean system temperature was 185 K in terms of $T_{\rm A}^{*}$ (antenna temperature with atmospheric correction) for CO$(1-0)$, and 528 K for CO$(2-1)$. The pointing was checked every $\sim$ 1.5 hours by observing a close-by quasar, and its accuracy was better

Name	$\log_{10} M_\star$ [$M_\odot$] (1)	$\log_{10} M_{HI}$ [$M_\odot$] (2)	$\log_{10}$ SFR [$M_\odot$ yr^{-1}] (3)	z (4)	D_L [Mpc] (5)
VGS07a	-	8.52 ± 0.09	-	0.016	70.5
VGS09a	-	7.79 ± 0.10	-	0.013	56.2
VGS10a	-	8.93 ± 0.10	-	0.016	68.4
VGS26a	-	10.31 ± 0.04	-	0.023	101.1
VGS30a	-	8.71 ± 0.07	-	0.019	84.5
VGS31a	10.02 ± 0.14	9.26 ± 0.05	0.81 ± 0.00	0.021	91.0
VGS31b	8.47 ± 0.05	8.45 ± 0.15	-0.82 ± 0.00	0.021	91.0
VGS34a	-	7.71 ± 0.13	-	0.017	71.7
VGS36a	-	< 11.83	-	0.022	97.6
VGS37a	-	9.19 ± 0.05	-1.15 ± 0.07	0.019	84.1
VGS38a	7.65 ± 0.05	8.02 ± 0.06	-1.74 ± 0.07	0.014	59.8
VGS38b	-	8.21 ± 0.06	-2.30 ± 0.00	0.014	59.8
VGS39a	-	8.50 ± 0.05	-	0.019	82.7
VGS51a	-	8.37 ± 0.04	-	0.025	110.5
VGS53a	-	8.58 ± 0.25	-	0.021	93.5
VGS54a	-	< 11.65	-	0.024	104.2
VGS56a	-	8.25 ± 0.16	-	0.019	81.3
VGS57a	8.00 ± 0.07	8.41 ± 0.08	-	0.022	96.6

Table 3.4: **Spectrometric properties for the VGS companions.** Same as Figure 3.2 but for the comanion galaxies inside the VGS.

than 3-6 arcsec. This is acceptable for the CO(1 − 0) with a half-power beam size of 22 arcsec at our observing frequency, but is not ideal for CO(2 − 1) with a half-power beam size of 11 arcsec. The planet Mars was observed every 2-3 hours to calibrate the antenna focus.

The on-source observing time ranged from 30 minutes for the brightest sources to 2 hours for the faintest sources. The observations were generally carried out until the CO(1−0) line was detected with a signal-to-noise ratio (S/N) greater than 5, except for VGS42, for which an S/N of only 3.8 could be achieved. If not detected, the observations were stopped at a root-mean-square noise (rms) of main beam temperature ($T_{\rm mb}$) below 1.5 mK at a velocity resolution of 20 km s^{-1}.

The line temperature is expressed in terms of $T_{\rm mb} = T_{\rm A}^* \times (F_{\rm eff}/B_{\rm eff})$, where $F_{\rm eff}$ is the IRAM 30 m telescope forward efficiency, which is 0.95 for CO(1 − 0) and 0.91 for CO(2 − 1), and $B_{\rm eff}$ is the beam efficiency, which is 0.77 for CO(1 − 0) and 0.58 for CO(2 − 1).

We used the GILDAS[2] software, provided by IRAM, to reduce the CO data. We discarded bad scans from the observations. We then subtracted a linear baseline from every spectrum. In some cases, spectra from the FTS backend have platforming, that is, the baseline of the spectrum presents steps at the end of the correlator bands. We used the `FtsPlatformingCorrection5.class` program, developed by IRAM, to correct for this artefact. We then averaged the spectra and smoothed them to a spectral resolution of 20 km s^{-1}. The final spectra are presented in Figs. A.3.1 and A.3.2.

[2]http://www.iram.fr/IRAMFR/GILDAS

We derived the emission line intensity ($I_{\rm CO}$) as the velocity-integrated $T_{\rm mb}$ within the zero-level line width (ΔV), which was determined visually for each averaged spectrum,

$$I_{\rm CO} = \int_{\Delta V} T_{\rm mb}(V) {\rm d}V \quad . \tag{3.2}$$

For non-detections, upper limits were defined as

$$I_{\rm CO} < 3 \times rms \times \sqrt{\delta V \Delta V},$$

where δV is the channel width in km s^{-1}, and ΔV was set to the mean value of the detections, which is 300 km s^{-1} for CO$(1-0)$ and 240 km s^{-1} for CO$(2-1)$. The 20 observed CO intensities and their statistical errors, calculated as $rms \times \sqrt{\delta V \Delta V}$, are listed in Table 3.5. In addition to the statistical error, we took a typical calibration error of 15% for CO$(1-0)$ and 30% for CO$(2-1)$ into account, estimated by Lisenfeld et al. (2019) from a comparison of the observation of four strong sources on different days. The CO$(1-0)$ line was detected (S/N > 3) for 13 galaxies and the CO$(2-1)$ line for 14 galaxies.

Aperture correction

The IRAM 30 m telescope beam of CO$(1-0)$ (22 arcsec) covers the entire galaxy in most objects of our sample. In order to correct for a small fraction of missing flux, we calculated an aperture correction following the procedure of Lisenfeld et al. (2011). The resulting aperture correction factor ($f_{\rm ap}$), listed in Table 3.6, has values between 1.1 and 1.5, and its mean value is 1.3.

The method assumes a molecular disc following an exponential profile with an exponential scale length $r_{\rm e} = 0.2 \times r_{25}$. Since r_{25} is not available in HyperLEDA[3] (Paturel et al. 1991) for all the objects and some values looked erroneous after visual inspection, we used the r-Petrosian R_{90} from SDSS. We compared R_{90} and r_{25} for the objects for which both values exist, and find the ratio $r_{25}/R_{90} = (1.7 \pm 0.5)$. We thus use R_{90} and the relation $r_{25} = 1.7 \times R_{90}$. In order to calculate $f_{\rm ap}$, we furthermore need to know the inclination (i) of the galaxy, which we took from Kreckel et al. (2012), who performed a photometric analysis of the VGS. The values are listed in Tab. 3.1. An inclination is available in the literature for all galaxies in the CO-VGS sample.

[3] http://leda.univ-lyon1.fr

Name	$I_{CO(1-0)}$ [K km s^{-1}]	rms [mK]	S/N	$\Delta V_{CO(1-0)}$ [km s^{-1}]	$I_{CO(2-1)}$ [K km s^{-1}]	rms [mK]	S/N	$\Delta V_{CO(2-1)}$ [km s^{-1}]
	(1)	(2)	(3)	(4)	(5)	(6)	(7)	(8)
VGS04	< 0.34	1.4	-	300	< 0.82	3.9	-	240
VGS11	< 0.31	1.3	-	300	1.15 ± 0.26	2.8	4.4	440
VGS19	< 0.35	1.5	-	300	< 0.68	3.2	-	240
VGS23	0.60 ± 0.10	1.3	6.0	290	1.36 ± 0.20	2.5	7.0	300
VGS26	< 0.25	1.0	-	300	< 0.58	2.8	-	240
VGS31	0.57 ± 0.10	1.4	5.9	250	1.39 ± 0.20	2.7	6.9	260
VGS31a	2.65 ± 0.20	2.3	13.6	350	2.15 ± 0.34	5.2	6.3	210
VGS32	2.20 ± 0.16	2.5	13.8	200	1.59 ± 0.28	4.4	5.6	200
VGS34	3.22 ± 0.22	2.6	14.3	360	3.38 ± 0.42	4.9	8.1	350
VGS36	< 0.32	1.3	-	300	< 0.54	2.6	-	240
VGS39	0.60 ± 0.11	1.2	5.4	380	0.89 ± 0.24	2.5	3.8	420
VGS42	0.58 ± 0.16	2.0	3.8	310	< 0.70	3.3	-	240
VGS44	0.55 ± 0.09	1.6	6.3	150	1.48 ± 0.17	2.6	8.8	200
VGS47	2.28 ± 0.17	1.8	13.8	420	1.30 ± 0.25	3.3	5.2	280
VGS49	0.87 ± 0.13	1.6	6.5	350	0.64 ± 0.19	3.3	3.4	160
VGS50	< 0.35	1.5	-	300	1.21 ± 0.24	2.6	5.0	420
VGS53	0.60 ± 0.09	1.2	6.6	300	0.72 ± 0.21	3.2	3.4	200
VGS56	0.79 ± 0.11	1.3	7.1	350	1.25 ± 0.21	2.6	6.1	300
VGS57	3.19 ± 0.16	2.0	20.5	300	4.38 ± 0.23	3.5	19.2	200
VGS58	< 0.29	1.2	-	300	< 0.42	2.0	-	240

Table 3.5: **CO emission line intensities for the CO-VGS.** (1) Velocity-integrated intensity and its statistical error of the CO$(1-0)$ emission line. (2) Root-mean-square noise of the CO$(1-0)$ emission line spectrum at a velocity resolution of 20 km s^{-1}. (3) Signal-to-noise ratio of the CO$(1-0)$ emission line. (4) Spectral zero-level line width of the CO$(1-0)$ emission line. For non-detections, we set it to the mean value of detections (300 km s^{-1}). (5)-(8) The same for the CO$(2-1)$ emission line. For non-detections in CO$(2-1)$, we set the spectral zero-level line width of the emission line (8) to the mean value of detections (240 km s^{-1}).

Molecular gas mass

With the (main beam) temperature-to-flux conversion factor

$$K_{\rm i-s} = 5\ Jy\ K^{-1}$$

of the IRAM 30 m telescope, the CO velocity integrated flux density is

$$S_{\rm CO}\Delta V\,[{\rm Jy\,km\,s^{-1}}] = K_{\rm i-s} \times I_{\rm CO}\,[{\rm K\,km\,s^{-1}}].$$

Following Solomon et al. (1997), we calculated the CO(1 − 0) luminosity as

$$L'_{\rm CO}[{\rm K\,km\,s^{-1}\,pc^2}] = 3.25\times10^7 S_{\rm CO}\Delta V \nu_{\rm rest}^{-2} D_{\rm L}^2 (1+{\rm z})^{-1} \quad ,$$

where $\nu_{\rm rest}$ is the emission line rest frequency in GHz, $D_{\rm L}$ is the luminosity distance in Mpc, and z is the optical redshift from MPA-JHU.

Finally, we calculated the molecular gas mass as $M_{\rm H_2} = \alpha_{\rm CO} L_{\rm CO}$, where $\alpha_{\rm CO}$ is the CO-to-H_2 conversion factor. We considered the Galactic $\alpha_{\rm CO} = 3.2\,{\rm M_\odot}\,({\rm K\,km\,s^{-1}\,pc^2})^{-1}$ (Bolatto et al. 2013), without correction for helium, as a constant value for the CO-VGS galaxies. Two galaxies (VGS11 and VGS50) are undetected in CO(1 − 0), but detected in CO(2 − 1). This is not unusual for objects that are smaller than the CO(1-0) beam, for which the beam dilution is less severe for $I_{\rm CO(2-1)}$ than for $I_{\rm CO(1-0)}$ because the CO(2-1) beam size is smaller (see Sect. 3.2.6 and Appendix A.1 for a detailed discussion of the influence of the beam size). For these cases, we estimated the CO(1 − 0) velocity-integrated intensity using the theoretical value of $R_{\rm 21theo} = I_{\rm CO(2-1)}/I_{\rm CO(1-0)}$, calculated in Appendix A.1. We adopted an intrinsic brightness ratio of $T_{\rm Bc2-1}/T_{\rm Bc1-0} = 0.8$ (Leroy et al. 2009), and based on the corresponding values of $r_{\rm e}$ and i for each galaxy, we derived $R_{\rm 21theo} = 3.0$ and 2.8 for VGS11 and VGS50, respectively. The resulting molecular gas masses are listed in Table 3.6.

3.1.2 Control sample

As we did for the VGS, we use for the control sample photometric data from the SDSS-DR16, and spectrometric properties from the SDSS-DR16 & MPA-JHU database (Kauffmann et al. 2003; Brinchmann et al. 2004; Tremonti et al. 2004; Salim et al. 2007). In particular, we used redshift (z), apparent dereddened magnitudes in r and g bands, r-Petrosian R_{90}, and $M_\star$. Find more details about the control sample selection in Section 2.1.3.

Name	$\log_{10} M_{H_2}$ [$M_\odot$] (1)	f_{ap} (2)
VGS04	< 7.83	1.05
VGS11$^{(*)}$	8.13 ± 0.16	1.43
VGS19	< 7.76	1.07
VGS23	8.23 ± 0.10	1.40
VGS26	< 8.08	1.25
VGS31	8.34 ± 0.10	1.20
VGS31a	9.12 ± 0.07	1.57
VGS32	8.54 ± 0.07	1.57
VGS34	8.90 ± 0.07	1.23
VGS36	< 8.14	1.19
VGS39	8.26 ± 0.10	1.16
VGS42	8.24 ± 0.13	1.17
VGS44	8.21 ± 0.09	1.30
VGS47	9.07 ± 0.07	1.46
VGS49	8.66 ± 0.09	1.15
VGS50$^{(*)}$	8.22 ± 0.16	1.10
VGS53	8.41 ± 0.09	1.28
VGS56	8.36 ± 0.09	1.15
VGS57	9.22 ± 0.07	1.45
VGS58	< 7.60	1.41

Table 3.6: **Molecular gas mass.** Column (1) is the molecular gas mass and total error. Column (2) is the aperture correction factor. (*) The molecular gas mass of these galaxies has been derived from the CO($2-1$) line emission intensity and the theoretical CO($2-1$)-to-CO($1-0$) line ratio estimated in Appendix A.1.

xGASS and xCOLD-GASS surveys

The metallicity range of the galaxies in xCOLD GASS is around solar ($8.46 < 12 + \log(O/H) < 9.22$, obtained by cross-matching the sample with Tremonti et al. 2004). Saintonge et al. (2017) observed the xCOLD-GASS galaxies in the IRAM 30 m telescope and applied a CO-to-H_2 conversion factor, α_{CO}, calibrated by Accurso et al. (2017), which is metallicity-dependent and has a second-order dependence on the offset of a galaxy from the star-forming main sequence. In order to provide a fair comparison between our void sample and xCOLD-GASS, we re-scaled the molecular gas mass of the xCOLD-GASS galaxies to the same value of the CO-to-H_2 conversion factor as used for our void sample (a constant $\alpha_{CO} = 3.2\,M_\odot\,(K\,km\,s^{-1}\,pc^2)^{-1}$, corresponding to

the Galactic value, not taking into account the presence of helium)[4]. The angular size of the galaxies are small enough to fit almost completely inside the IRAM 30 m telescope beam width. Only a small aperture correction of a mean $f_{\rm ap} \sim 1.17$ is required. For the aperture correction, they followed the procedure defined in Lisenfeld et al. (2011), as we did for the CO-VGS, with a difference in the exponential scale. They considered an exponential H_2 distribution with a half-light radius corresponding to the radius enclosing 50% of the star formation as measured in the SDSS/GALEX photometry, whereas we describe the exponential distribution of the H_2 with the exponential scale factor $r_{\rm e} = 0.2 \times r_{25}$. We do not expect this relatively small difference to have any impact on our results because the aperture corrections, especially for the CO-VGS sample, are small. Tables 3.7 and 3.8 compare the *rms* and the $I_{\rm CO}$ between xCOLD GASS and the CO-VGS; the detection levels are similar.

rms [mK]

Sample	Detections			Non-Detections		
	min	max	mean	min	max	mean
CO-VGS	1.2	2.6	1.7	1.0	1.5	1.3
xCOLD GASS	0.8	4.2	1.8	0.7	3.2	1.3

Table 3.7: Comparison of the *rms* between CO-VGS and xCOLD GASS.

$I_{\rm CO}$[K km s^{-1}]

Sample	Detections		
	min	max	mean
CO-VGS	0.5	3.2	1.4
xCOLD GASS	0.1	17.8	1.7

Table 3.8: Comparison of the $I_{\rm CO}$ between CO-VGS and xCOLD GASS.

EDGE-CALIFA survey

In EDGE-CALIFA, $M_{\rm H_2}$ was derived considering a constant Galactic CO-to-H_2 conversion factor $\alpha_{\rm CO} = 4.6\,{\rm M}_\odot\,({\rm K\,km\,s^{-1}\,pc^2})^{-1}$, including the mass correction for the presence of helium. In this work, we

[4]The $\alpha_{\rm CO}$ factor was not re-scaled in Domínguez-Gómez et al. (2022) but it was later applied in a corrigendum (Domínguez-Gómez et al. 2023). The conclusions of the study did not change.

rescaled the molecular gas mass of the EDGE-CALIFA galaxies considering $\alpha_{CO} = 3.2\,M_\odot\,(K\,km\,s^{-1}\,pc^2)^{-1}$, not including the helium correction, for a consistent comparison with the other surveys.

CARMA is an interferometer and is therefore not sensitive to emission above a certain spatial scale, which means that an extended flux component can be missed. Bolatto et al. (2017) compared galaxies observed by both the CARMA interferometer and the single-dish IRAM 30 m telescope and concluded that missing flux is not an important problem in the CARMA EDGE-CALIFA observations.

We used H I data from López-Sánchez et al. (in prep.), who searched the literature for H I data for CALIFA galaxies and found valid H I data for 511 objects (HI-CALIFA), the large majority coming from single-dish observations. Most of the data come from three large surveys: Springob et al. (2005) (305 objects, 60%), Huchtmeier & Richter (1989) (95 objects, 19%), and Theureau et al. (2004) (39 objects, 8%). The remaining galaxies come from 27 references that each provide H I data for between 1 and 14 objects.

3.2 Results

In this section, we compare the gas mass, star formation rate, and stellar mass of void galaxies to those galaxies in filaments and walls. We carry out this comparison for different sub-samples (find more details of the sample selection in Section 2.1). The CCS is compared with the entire VGS for properties not involving CO, such as M_{HI} and sSFR. The CO-VGS is compared with the CO-CS for properties related to CO emission lines such as M_{H_2}, molecular-to-atomic gas mass ratio (M_{H_2}/M_{HI}), and SFE, which are not available for the entire VGS. Furthermore, we present all comparisons for the entire samples and also for sub-samples containing only Star-Forming (SF) galaxies, which are close to the SFMS. The reason for this limitation is that the VGS galaxies are, partly by selection, mainly SF galaxies and only a few of them fall below the SFMS. The control sample, on the other hand, contains many galaxies with a very low sSFR (see Fig. 3.1-left). In order to compare the same type of objects, we exclude quiescent galaxies that are situated well below the SFMS. We adopt the prescription of the SFMS derived in Saintonge et al. (2016) (their eq. 5) for the COLD GASS sample and we derive from it a main sequence in the sSFR ($sSFR_{MS}$) by division with $M_\star$. For our SF sub-sample we then select the ob-

jects that are above the limit $\log_{10}(\mathrm{sSFR}/\mathrm{sSFR_{MS}}) \geq -0.8$, which is represented as the dashed line in Fig. 3.1. In this way, we remove very low star-forming galaxies from the VGS and from the control sample. We call this selection the SF sub-sample. Additionally, we select spiral galaxies using the morphological parameter, t > 0, from HyperLEDA and performed the entire analysis for the spiral sub-sample. We obtained consistent results for the SF and the spiral sub-sample.

We define three mass bins to compare the CO-VGS and CO-CS as a function of stellar mass:

$$10^{9.0}\mathrm{M}_\odot \leq M_\star < 10^{9.5}\mathrm{M}_\odot,$$

$$10^{9.5}\mathrm{M}_\odot \leq M_\star < 10^{10.0}\mathrm{M}_\odot,$$

$$10^{10.0}\mathrm{M}_\odot \leq M_\star \leq 10^{10.5}\mathrm{M}_\odot,$$

and the entire mass range,

$$10^{9.0}\mathrm{M}_\odot \leq M_\star \leq 10^{10.5}\mathrm{M}_\odot.$$

For the VGS and the CCS, we define two additional mass bins:

$$10^{8.0}\mathrm{M}_\odot \leq M_\star < 10^{8.5}\mathrm{M}_\odot,$$

$$10^{8.5}\mathrm{M}_\odot \leq M_\star < 10^{9.0}\mathrm{M}_\odot,$$

and the entire mass range,

$$10^{8.0}\mathrm{M}_\odot \leq M_\star \leq 10^{10.5}\mathrm{M}_\odot.$$

We then calculate the mean and median values in every stellar mass bin for both the VGS and the control sample. There are many non-detections for the molecular and atomic gas mass. In order to keep the high statistics, we use the Kaplan-Meier estimator (Kaplan & Meier 1958), which calculates the mean value taking upper limits into account. As an additional test, we apply the KS-test in every stellar bin considering upper limits as detections. The KS test indicates only marginal differences between the samples when the p-value $\lesssim 0.05$, but it denotes high contrast for much lower p-values. We show the corresponding values and the difference between the VGS and the control sample in Tables 3.9-3.15.

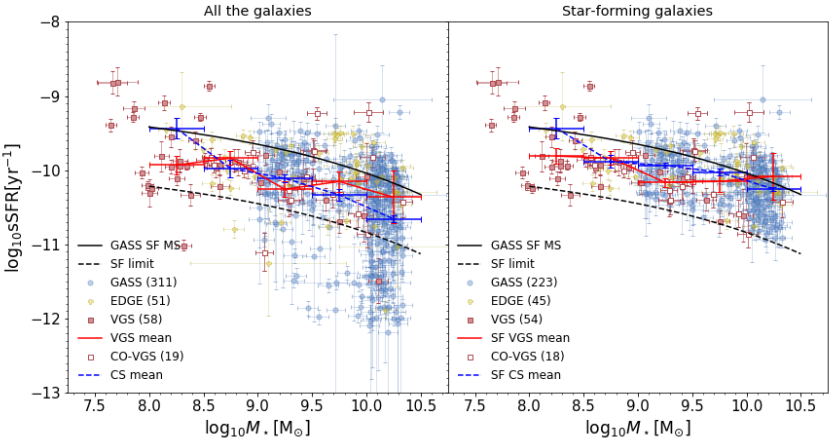

Figure 3.1: Specific star formation rate as a function of stellar mass for the VGS and CCS with all the galaxies (left), and only star-forming galaxies (right). The mean sSFR per $M_\star$ bin is shown with a red symbol (connected by a solid red line to guide the eye) for the VGS, and with a blue symbol (and dashed blue line) for the CCS. The error bar in $M_\star$ represents the width of the stellar mass bin. The GASS sSFR main sequence is represented as solid black line. This is a fit to the main-sequence galaxies carried out by Saintonge et al. (2017). The dashed black line is the limit chosen by us to select star-forming galaxies (see Sect. 3.2).

3.2.1 Specific star formation rate

The sSFR (Figure 3.1 and Table 3.9) shows a decreasing trend with $M_\star$ for the comparison sample and the VGS, even though it is more pronounced for the comparison sample. The mean values of both samples lie below the main sequence that was fitted by Saintonge et al. (2016), which is expected because this fit was made by taking only the star-forming ridge of galaxies into account. It therefore excluded passive galaxies with a low sSFR. Therefore, the agreement between the mean values of the CCS and the main sequence fit is much better for our SF sub-sample (right panel). Interestingly, in this case, there is no significant difference between the void and the comparison sample, except for stellar masses between $10^{9.0}$ and $10^{9.5}\mathrm{M}_\odot$, where the mean sSFR of the VGS is lower than the CCS ($|\sigma| > 3$ and KS p-value < 0.05), and the lowest mass bin, where the CCS only contains 3 objects, however.

$\log_{10}$ sSFR[yr^{-1}]

	$\log_{10} M_\star$[M$_\odot$] range (1)		VGS n/n$_{up}$ (2)	VGS mean (3)	VGS median (4)	CCS n/n$_{up}$ (5)	CCS mean (6)	CCS median (7)	VGS - CCS Δmean (8)	VGS - CCS σ (9)	VGS - CCS KS (10)
ALL	8.0	8.5	14/1	-9.93 ± 0.12	-9.94	3/0	-9.43 ± 0.14	-9.45	-0.50 ± 0.18	-	-
	8.5	9.0	12/0	-9.84 ± 0.09	-9.89	10/0	-9.98 ± 0.12	-9.96	0.14 ± 0.15	0.94	0.23
	9.0	9.5	10/0	-10.26 ± 0.10	-10.16	85/0	-10.11 ± 0.05	-10.02	-0.15 ± 0.12	-1.27	0.06
	9.5	10.0	10/1	-10.15 ± 0.14	-10.14	69/0	-10.33 ± 0.08	-10.17	0.18 ± 0.16	1.11	0.71
	10.0	10.5	5/0	-10.36 ± 0.35	-10.43	195/0	-10.66 ± 0.05	-10.49	0.29 ± 0.36	0.82	0.50
	8.0	10.5	51/2	-10.06 ± 0.07	-10.0	362/0	-10.44 ± 0.04	-10.28	0.38 ± 0.08	4.91	2×10^{-3}
SF	8.0	8.5	12/0	-9.81 ± 0.10	-9.87	3/0	-9.43 ± 0.14	-9.45	-0.38 ± 0.17	-	-
	8.5	9.0	12/0	-9.84 ± 0.09	-9.89	9/0	-9.88 ± 0.09	-9.96	0.05 ± 0.12	0.38	0.42
	9.0	9.5	9/0	-10.16 ± 0.06	-10.16	71/0	-9.94 ± 0.03	-9.92	-0.23 ± 0.07	-3.33	0.02
	9.5	10.0	10/0	-10.15 ± 0.14	-10.14	54/0	-10.03 ± 0.05	-10.04	-0.12 ± 0.15	-0.84	0.54
	10.0	10.5	4/0	-10.08 ± 0.31	-9.82	131/0	-10.25 ± 0.03	-10.22	0.17 ± 0.31	0.55	0.38
	8.0	10.5	47/0	-9.98 ± 0.06	-9.95	268/0	-10.10 ± 0.02	-10.10	0.12 ± 0.06	1.93	0.07

Table 3.9: **Specific star formation rate.** (1) Stellar mass range of the bin. (2) n: Number of VGS galaxies in the bin. n$_{up}$: Number of upper limits of VGS galaxies in the bin. (3) Mean logarithm of the specific star formation rate and its error of the VGS galaxies in the bin. (4) Median logarithm of the specific star formation rate of the VGS galaxies in the bin. (5) - (7) The same for the CCS sample. (8) Difference of the mean logarithmic of the specific star formation rate between VGS and CCS (Δmean) and its error (err(Δmean)). (9) $\sigma = \Delta\text{mean}/\text{err}(\Delta\text{mean})$, only reported when there are at least four objects in each sample. (10) p-value of the Kolmogorov-Smirnov test.

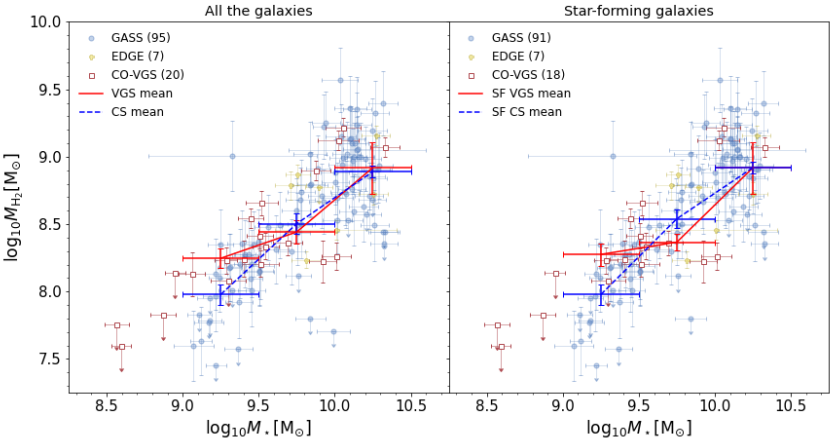

Figure 3.2: Molecular gas mass as a function of stellar mass for the CO-VGS and CO-CS with all the galaxies (left) and only star-forming galaxies (right). The mean $M_{\rm H_2}$ per $M_\star$ bin is shown with a red symbol (connected by a solid red line to guide the eye) for the CO-VGS, and with a blue symbol (and dashed blue line) for the CO-CS. The error bar in $M_\star$ represents the width of the stellar mass bin.

3.2.2 Molecular gas mass

The molecular gas mass shows an increasing trend with $M_\star$ for the void and the comparison samples (Figure 3.2 and Table 3.10). In general, the mean values of the CO-VGS and CO-CS samples agree within the errors, except for the low $M_\star$ bin, where the mean $M_{\rm H_2}$ for void galaxies (for all the galaxies and also for SF galaxies) is slightly higher ($|\sigma| \sim 2.6$) than for galaxies in filaments and walls. However, the KS p-value in this stellar mass bin is > 0.20, and we can not confirm that the CO-VGS and the CO-CS come from different mother samples. The difference is marginal ($|\sigma| < 2$ and KS p-values > 0.10) in the other stellar mass for all the galaxies and also for SF galaxies.

The molecular gas mass fraction ($M_{\rm H_2}/M_\star$) shows a decreasing trend with $M_\star$ for the void and the comparison samples (Figure 3.3 and Table 3.11). There is no significant difference between the two samples ($|\sigma| < 2$), except for the low stellar mass bin, where voids galaxies have slightly higher molecular gas fraction for the complete sample ($|\sigma| \sim 2.92$) and also for the SF sub-sample ($|\sigma| \sim 2.47$). However, the KS p-value in this stellar mass bin is > 0.1, so we can not confirm that the CO-VGS and the CO-CS come from different mother

	$\log_{10} M_\star[M_\odot]$ range		$\log_{10} M_{H_2}[M_\odot]$ CO-VGS			CO-CS			CO-VGS - CO-CS		
			n/n_{up}	mean	median	n/n_{up}	mean	median	Δmean	σ	KS
	(1)		(2)	(3)	(4)	(5)	(6)	(7)	(8)	(9)	(10)
ALL	9.0	9.5	5/1	8.25 ± 0.07	8.23	26/8	7.98 ± 0.08	8.09	0.27 ± 0.11	2.56	0.24
	9.5	10.0	7/0	8.44 ± 0.09	8.36	29/4	8.50 ± 0.07	8.49	-0.06 ± 0.11	-0.53	0.34
	10.0	10.5	4/0	8.92 ± 0.19	9.12	47/6	8.89 ± 0.04	8.94	0.03 ± 0.20	0.15	0.28
	9.0	10.5	16/1	8.5 ± 0.09	8.36	102/18	8.52 ± 0.05	8.6	-0.02 ± 0.11	-0.19	0.21
SF	9.0	9.5	4/1	8.28 ± 0.08	8.24	26/8	7.98 ± 0.08	8.09	0.30 ± 0.11	2.63	0.30
	9.5	10.0	6/0	8.37 ± 0.06	8.34	28/3	8.54 ± 0.07	8.50	-0.17 ± 0.09	-1.90	0.10
	10.0	10.5	4/0	8.92 ± 0.19	9.12	44/4	8.92 ± 0.04	8.94	<0.01 ± 0.20	<0.01	0.35
	9.0	10.5	14/1	8.5 ± 0.1	8.34	98/15	8.54 ± 0.05	8.67	-0.04 ± 0.11	-0.38	0.2

Table 3.10: **Molecular gas mass.** (1) Stellar mass range of the bin. (2) Number of CO-VGS galaxies in the bin. n_{up}: Number of upper limits of CO-VGS galaxies in the bin. (3) Mean logarithm of the molecular gas mass and its error of the CO-VGS galaxies in the bin. (4) Median logarithm of the molecular gas mass of the CO-VGS galaxies in the bin. (5) - (7) The same for the CO-CS sample. (8) Difference of the mean logarithmic of the molecular gas mass between CO-VGS and CO-CS (Δmean) and its error (err(Δmean)). (9) $\sigma = \Delta\text{mean}/\text{err}(\Delta\text{mean})$. (10) p-value of the Kolmogorov-Smirnov test.

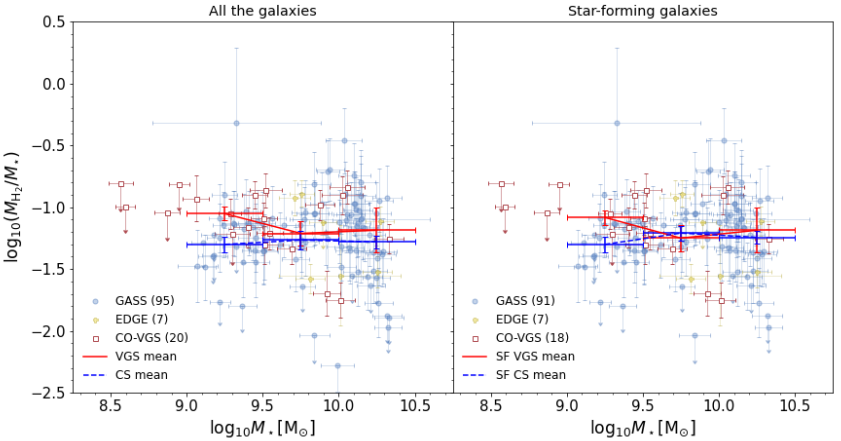

Figure 3.3: Molecular gas mass fraction as a function of stellar mass for the CO-VGS and CO-CS with all the galaxies (left) and only star-forming galaxies (right). The mean $M_{H_2}/M_\star$ per $M_\star$ bin is shown with a red symbol (connected by a solid red line to guide the eye) for the CO-VGS, and with a blue symbol (and dashed blue line) for the CO-CS. The error bar in $M_\star$ represents the width of the stellar mass bin.

samples.

In summary, we conclude that we find no significant difference for M_{H_2} or $M_{H_2}/M_\star$ between CO-VGS and CO-CS. For both samples, we find increasing trends of M_{H_2} with $M_\star$.

3.2.3 Star formation efficiency

The SFE (Figure 3.4 and Table 3.12) shows a decreasing trend with $M_\star$ for the comparison sample. This trend is followed by the void galaxies for the intermediate and upper $M_\star$ bin, where the mean values agree within 1 σ. However, in the lowest-mass bin, void galaxies have a significantly ($|\sigma| > 4$ and KS p-value < 0.001) lower mean SFE for the entire sample and for the SF sub-sample. The number of galaxies in this bin is relatively low (four to six galaxies), and it needs to be confirmed with a larger sample size.

3.2.4 Atomic gas mass

The atomic gas mass fraction ($M_{HI}/M_\star$, Figure 3.5 and Table 3.13) shows a strongly decreasing trend with $M_\star$ for both the VGS and

$\log_{10}(M_{H_2}/M_\star)$

	$\log_{10} M_\star[M_\odot]$ range		CO-VGS			CO-CS			CO-VGS - CO-CS		
			n/n_{up}	mean	median	n/n_{up}	mean	median	Δmean	σ	KS
	(1)		(2)	(3)	(4)	(5)	(6)	(7)	(8)	(9)	(10)
ALL	9.0	9.5	5/1	-1.05 ± 0.06	-1.05	26/8	-1.30 ± 0.06	-1.25	0.25 ± 0.09	2.92	0.12
	9.5	10.0	7/0	-1.21 ± 0.10	-1.21	29/4	-1.27 ± 0.08	-1.21	0.05 ± 0.12	0.44	1.00
	10.0	10.5	4/0	-1.19 ± 0.18	-0.90	47/6	-1.28 ± 0.05	-1.19	0.09 ± 0.19	0.50	0.43
	9.0	10.5	16/1	-1.17 ± 0.07	-1.09	102/18	-1.32 ± 0.04	-1.22	0.14 ± 0.08	1.72	0.4
SF	9.0	9.5	4/1	-1.08 ± 0.06	-1.05	26/8	-1.30 ± 0.06	-1.25	0.22 ± 0.09	2.47	0.19
	9.5	10.0	6/0	-1.25 ± 0.10	-1.30	28/3	-1.21 ± 0.06	-1.15	-0.04 ± 0.12	-0.34	0.95
	10.0	10.5	4/0	-1.19 ± 0.18	-0.90	44/4	-1.24 ± 0.05	-1.17	0.06 ± 0.19	0.31	0.49
	9.0	10.5	14/1	-1.2 ± 0.08	-1.21	98/15	-1.26 ± 0.04	-1.19	0.06 ± 0.09	0.67	0.76

Table 3.11: **Molecular gas mass fraction.** (1) Stellar mass range of the bin. (2) Number of CO-VGS galaxies in the bin. n_{up}: Number of upper limits of CO-VGS galaxies in the bin. (3) Mean logarithm of the molecular gas mass fraction and its error of the CO-VGS galaxies in the bin. (4) Median logarithm of the molecular gas mass fraction of the CO-VGS galaxies in the bin. (5) - (7) The same for the CO-CS sample. (8) Difference of the mean logarithmic of the molecular gas mass fraction between CO-VGS and CO-CS (Δmean) and its error (err(Δmean)). (9) $\sigma = \Delta$mean/err(Δmean). (10) p-value of the Kolmogorov-Smirnov test applied inside the bin to compare the CO-VGS and the CO-CS.

$\log_{10}$ SFE[yr^{-1}]

	$\log_{10} M_\star$[M$_\odot$] range		CO-VGS			CO-CS			CO-VGS - CO-CS		
			n/n$_{up}$	mean	median	n/n$_{up}$	mean	median	Δmean	σ	KS
	(1)		(2)	(3)	(4)	(5)	(6)	(7)	(8)	(9)	(10)
ALL	9.0	9.5	5/0	-9.34 $\pm$ 0.19	-9.18	26/0	-8.49 $\pm$ 0.07	-8.44	-0.84 $\pm$ 0.20	-4.18	<0.01
	9.5	10.0	6/1	-8.71 $\pm$ 0.15	-8.87	29/0	-8.77 $\pm$ 0.07	-8.77	0.06 $\pm$ 0.17	0.36	0.50
	10.0	10.5	4/0	-8.90 $\pm$ 0.17	-9.12	47/0	-8.96 $\pm$ 0.05	-8.91	0.06 $\pm$ 0.18	0.35	0.87
	9.0	10.5	15/1	-8.95 $\pm$ 0.13	-8.99	102/0	-8.78 $\pm$ 0.04	-8.78	-0.17 $\pm$ 0.13	-1.29	0.11
SF	9.0	9.5	4/0	-9.13 $\pm$ 0.04	-9.18	26/0	-8.49 $\pm$ 0.07	-8.44	-0.63 $\pm$ 0.08	-8.02	<0.01
	9.5	10.0	6/0	-8.71 $\pm$ 0.15	-8.87	28/0	-8.79 $\pm$ 0.07	-8.79	0.08 $\pm$ 0.16	0.48	0.74
	10.0	10.5	4/0	-8.90 $\pm$ 0.17	-9.12	44/0	-8.95 $\pm$ 0.05	-8.91	0.06 $\pm$ 0.18	0.31	0.89
	9.0	10.5	14/0	-8.86 $\pm$ 0.1	-8.99	98/0	-8.78 $\pm$ 0.04	-8.78	-0.08 $\pm$ 0.11	-0.78	0.07

Table 3.12: **Star formation efficiency.** (1) Stellar mass range of the bin. (2) Number of CO-VGS galaxies in the bin. n$_{up}$: Number of upper limits of CO-VGS galaxies in the bin. (3) Mean logarithm of the star formation efficiency and its error of the CO-VGS galaxies in the bin. (4) Median logarithm of the star formation efficiency of the CO-VGS galaxies in the bin. (5) - (7) The same for the CO-CS sample. (8) Difference of the mean logarithmic of the star formation efficiency between CO-VGS and CO-CS (Δmean) and its error (err(Δmean)). (9) $\sigma = \Delta$mean/err(Δmean). (10) p-value of the Kolmogorov-Smirnov test.

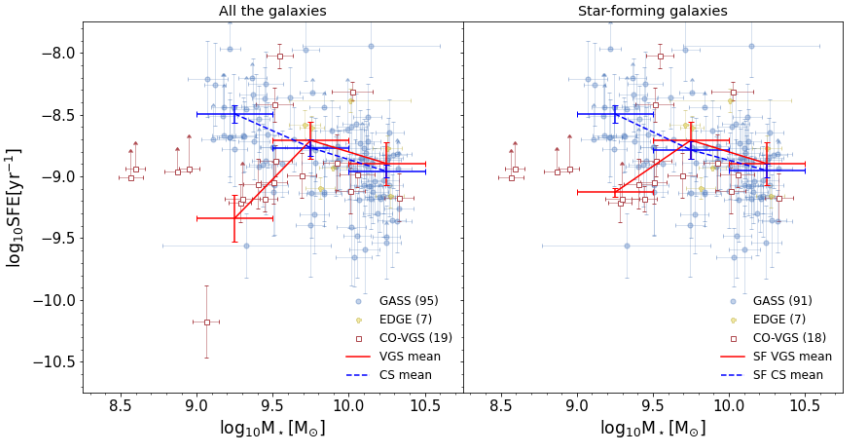

Figure 3.4: Star formation efficiency as a function of stellar mass for the CO-VGS and CO-CS with all the galaxies (left) and only star-forming galaxies (right). The mean SFE per $M_\star$ bin is shown with a red symbol (connected by a solid red line to guide the eye) for the CO-VGS, and with a blue symbol (and dashed blue line) for the CO-CS. The error bar in $M_\star$ represents the width of the stellar mass bin.

CCS. We can directly compare the VGS to the comparison sample for $M_\star > 10^{8.0}$ $M_\odot$, and the trend for the VGS galaxies seems to follow the trend of the CCS very well.

In general, the mean values of void and control galaxies agree reasonably well, except for galaxies with $M_\star > 10^{9.0}$ $M_\odot$, which show indications for a steeper slope for the VGS. In the SF sub-sample, the mean $M_{\rm HI}/M_\star$ of the VGS is lower than the CCS for $10^{9.5} < M_\star/M_\odot < 10^{10.5}$, but the difference is statistically marginal ($|\sigma| \lesssim 3$ and KS p-value $\gtrsim 0.05$). Furthermore, for the highest stellar mass bin ($10^{10.0} < M_\star/M_\odot < 10^{10.5}$), it is based on a very low number of galaxies (four).

3.2.5 Molecular-to-atomic gas mass ratio

The molecular-to-atomic gas mass ratio (Figure 3.6 and Table 3.14) shows an increasing trend with $M_\star$ for the void and the comparison samples. In the low and intermediate stellar mass bins, the mean values of the VGS and comparison sample are in agreement within 1 σ, whereas in the high stellar mass bin, the mean value for the VGS is considerably higher. However, this difference has to be taken with caution because of the low number of VGS galaxies (three) in this bin.

$\log_{10}(M_{\rm HI}/M_\star)$

	$\log_{10} M_\star[\mathrm{M}_\odot]$ range		VGS			CCS			VGS - CCS		
			n/n_{up}	mean	median	n/n_{up}	mean	median	Δmean	σ	KS
	(1)		(2)	(3)	(4)	(5)	(6)	(7)	(8)	(9)	(10)
ALL	8.0	8.5	15/4	0.44 ± 0.11	0.53	3/0	0.33 ± 0.08	0.29	0.11 ± 0.13	-	-
	8.5	9.0	11/4	0.05 ± 0.14	0.21	10/0	0.10 ± 0.23	0.31	-0.05 ± 0.27	-0.20	0.98
	9.0	9.5	8/2	-0.04 ± 0.12	0.06	85/13	-0.39 ± 0.07	-0.22	0.36 ± 0.14	2.54	0.09
	9.5	10.0	11/3	-0.81 ± 0.15	-0.79	69/12	-0.58 ± 0.08	-0.40	-0.23 ± 0.17	-1.33	0.33
	10.0	10.5	5/2	-1.28 ± 0.14	-1.25	195/56	-1.05 ± 0.05	-0.95	-0.23 ± 0.14	-1.62	0.24
	8.0	10.5	50/15	-0.27 ± 0.12	-0.08	362/81	-0.77 ± 0.04	-0.71	0.51 ± 0.12	4.10	6×10^{-7}
SF	8.0	8.5	12/4	0.40 ± 0.13	0.53	3/0	0.33 ± 0.08	0.29	0.07 ± 0.15	-	-
	8.5	9.0	11/4	0.05 ± 0.14	0.21	9/0	0.31 ± 0.12	0.31	-0.26 ± 0.19	-1.41	0.85
	9.0	9.5	7/2	-0.08 ± 0.13	0.06	71/5	-0.22 ± 0.07	-0.06	0.14 ± 0.14	0.95	0.40
	9.5	10.0	10/3	-0.84 ± 0.17	-0.79	54/3	-0.35 ± 0.07	-0.28	-0.49 ± 0.18	-2.75	0.03
	10.0	10.5	4/1	-1.20 ± 0.15	-1.21	131/11	-0.77 ± 0.04	-0.72	-0.44 ± 0.15	-2.85	0.08
	8.0	10.5	44/14	-0.30 ± 0.12	-0.12	268/19	-0.50 ± 0.04	-0.44	0.20 ± 0.13	1.52	5×10^{-4}

Table 3.13: **Atomic gas mass fraction.** (1) Stellar mass range of the bin. (2) Number of VGS galaxies in the bin. n_{up}: Number of upper limits of VGS galaxies in the bin. (3) Mean logarithm of the atomic gas mass fraction and its error of the VGS galaxies in the bin. (4) Median logarithm of the atomic gas mass fraction of the VGS galaxies in the bin. (5) - (7) The same for the CCS sample. (8) Difference of the mean logarithmic of the atomic gas mass fraction between VGS and CCS (Δmean) and its error (err(Δmean)). (9) $\sigma = \Delta\mathrm{mean}/\mathrm{err}(\Delta\mathrm{mean})$, only reported when there are at least 4 objects in each sample. (10) p-value of the Kolmogorov-Smirnov test.

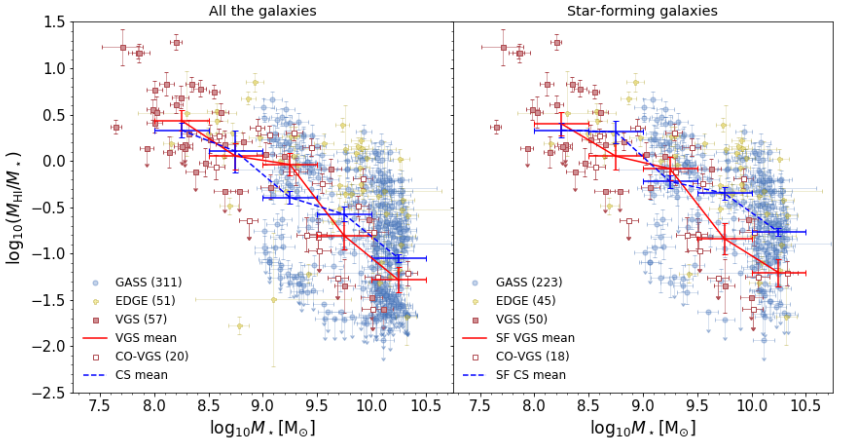

Figure 3.5: Atomic gas mass fraction as a function of stellar mass for the VGS and CCS with all the galaxies (left) and only star-forming galaxies (right). The mean $M_{\rm HI}/M_\star$ per $M_\star$ bin is shown with a red symbol (connected by a solid red line to guide the eye) for the VGS, and with a blue symbol (and dashed blue line) for the CCS. The error bar in $M_\star$ represents the width of the stellar mass bin.

Because the Kaplan-Meier estimator can only deal with upper or lower limits but not with both, we included only the upper limits (i.e. upper limits in $M_{\rm H_2}$ and detections in $M_{\rm HI}$) in the calculation of the mean. We also carried out this analysis with only lower limits (i.e. upper limits in $M_{\rm HI}$ and detection in $M_{\rm H_2}$) and obtained consistent results.

3.2.6 CO(2 − 1)-to-CO(1 − 0) line ratio

The left panel of Fig. 3.7 shows the relation between CO(2 − 1) and CO(1 − 0) for the CO-VGS together with the xCOLD GASS comparison sample. For 15 CO-VGS galaxies, we obtained a detection in at least one line, so that we can calculate the mean value of the line ratio $R_{21} = I_{\rm CO(2-1)}/I_{\rm CO(1-0)}$ (listed in Table 3.15, together with the corresponding value for the xCOLD GASS sample). The mean values for the CO-VGS and xCOLD GASS samples are the same (within the errors). The mean values are not aperture-corrected, and therefore we have to take into account the different beam sizes of CO(1 − 0) and CO(2 − 1) when the ratios are interpreted.

To interpret R_{21} (Fig. 3.7 right), we have to consider two param-

$\log_{10}(M_{H_2}/M_{HI})$ (Upper limits)

	$\log_{10} M_\star[M_\odot]$ range		CO-VGS			CO-CS			CO-VGS - CO-CS		
			n/n_{up}	mean	median	n/n_{up}	mean	median	Δmean	σ	KS
	(1)		(2)	(3)	(4)	(5)	(6)	(7)	(8)	(9)	(10)
ALL	9.0	9.5	5/1	-1.06 ± 0.16	-1.22	25/8	-1.34 ± 0.07	-1.27	0.28 ± 0.18	1.58	0.84
	9.5	10.0	5/0	-0.75 ± 0.20	-0.50	27/3	-0.83 ± 0.08	-0.92	0.07 ± 0.21	0.35	0.25
	10.0	10.5	3/0	0.08 ± 0.14	-0.05	45/6	-0.62 ± 0.07	-0.68	0.70 ± 0.15	-	-
	9.0	10.5	13/1	-0.69 ± 0.16	-0.5	97/17	-0.88 ± 0.05	-0.92	0.19 ± 0.17	1.14	0.05
SF	9.0	9.5	4/1	-1.04 ± 0.20	-1.05	25/8	-1.34 ± 0.07	-1.27	0.30 ± 0.22	1.40	0.51
	9.5	10.0	4/0	-0.82 ± 0.23	-0.48	27/3	-0.83 ± 0.08	-0.92	0.01 ± 0.25	0.04	0.35
	10.0	10.5	3/0	0.08 ± 0.14	-0.05	43/4	-0.59 ± 0.07	-0.65	0.66 ± 0.15	-	-
	9.0	10.5	11/1	-0.66 ± 0.18	-0.48	95/15	-0.87 ± 0.05	-0.92	0.21 ± 0.19	1.07	0.05

Table 3.14: **Molecular-to-atomic gas mass ratio.** Means have been calculated taking upper limits into account, but not lower limits. (1) Stellar mass range of the bin. (2) Number of CO-VGS galaxies in the bin. n_{up}: Number of upper limits of CO-VGS galaxies in the bin. (3) Mean logarithm of the molecular-to-atomic gas mass ratio and its error of the CO-VGS galaxies in the bin. (4) Median logarithm of the molecular-to-atomic gas mass ratio of the CO-VGS galaxies in the bin. (5) - (7) The same for the CO-CS sample. (8) Difference of the mean logarithmic of the molecular-to-atomic gas mass ratio between CO-VGS and CO-CS (Δmean) and its error (err(Δmean)). (9) $\sigma = \Delta\text{mean}/\text{err}(\Delta\text{mean})$, only reported when there are at least four objects in each sample. (10) p-value of the Kolmogorov-Smirnov test.

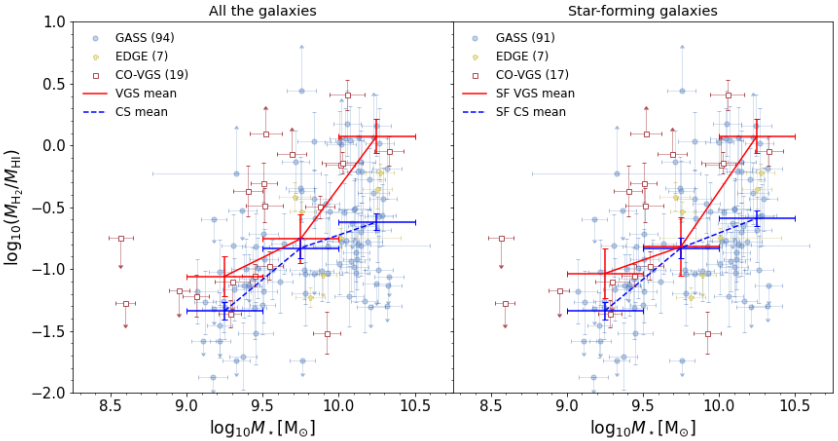

Figure 3.6: Molecular-to-atomic gas mass ratio as function of stellar mass for the CO-VGS and the CO-CS with all the galaxies (left) and only star-forming galaxies (right). The mean $M_{\rm H_2}/M_{\rm HI}$ per $M_\star$ bin is calculated taking upper limits into account but not lower ones, and it is shown with a red symbol (connected by a solid red line to guide the eye) for the CO-VGS, and with a blue symbol (and dashed blue line) for the CO-CS. The error bar in $M_\star$ represents the width of the stellar mass bin.

eters in addition to the excitation temperature of the gas: the source size relative to the beam, and the opacity of the molecular gas. For optically thick thermalised emission with a point-like distribution, we expect a ratio $R_{21} = (\Theta_{1-0}/\Theta_{2-1})^2 = 4$, with Θ_{1-0} and Θ_{2-1} being the Full Width at Half Maximum (FWHM) of the CO(1−0) and CO(2−1) beam, respectively. On the other hand, for a source that is more extended than the beams, we expect $R_{21} \sim 0.6-1$ for optically thick gas in thermal equilibrium, where R_{21} depends on the temperature of the gas, and $R_{21} > 1$ for optically thin gas.

In order to better quantify the combined effect of sources size and intrinsic brightness temperature, we calculated the theoretical line ratio, $R_{21\rm theo}$ (see Appendix A.1) by modelling the CO emission with the same 2D exponential distributions as used for the aperture correction and adopting the IRAM 30 m telescope beam as a Gaussian function, with values for the FWHM of $\Theta_{1-0} = 22$ arcsec and $\Theta_{2-1} = 11$ arcsec. We compare the observed R_{21} empirical values with the theoretical $R_{21\rm theo}$ values for different intrinsic brightness temperature ratios of the source ($\bar{T}_{\rm Bc2-1}/\bar{T}_{\rm Bc1-0} = 1$, 0.7 and 0.5) in the right panel of Figure 3.7. For optically thick gas in thermal equilibrium, an intrinsic brightness

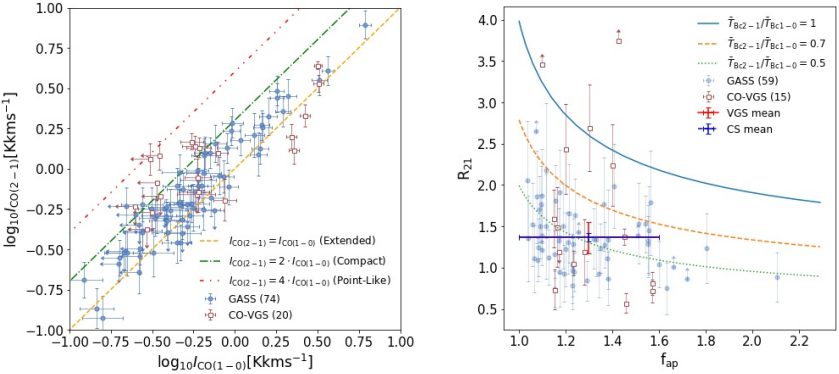

Figure 3.7: Correlation between the CO emission line intensities. (Left) $I_{\mathrm{CO}(2-1)}$ and $I_{\mathrm{CO}(1-0)}$ emission line comparison for CO-VGS and xCOLD GASS galaxies. (Right) Emission line ratio ($R_{21} = I_{\mathrm{CO}(2-1)}/I_{\mathrm{CO}(1-0)}$) as a function of the aperture-correction factor (f_{ap}) for CO-VGS and xCOLD GASS galaxies.

ratio of 0.6 corresponds to an excitation temperature of $\sim$ 5 K, 0.8 to $\sim$ 10 K, and 0.9 to $\sim$ 21 K; higher excitation temperatures yield a brightness temperature ratio $\sim$ 1 (Leroy et al. 2009). The observed R_{21} in general follows the predicted trend of a decreasing value with f_{ap} well (which is an increasing function with galactic size). This indicates that the aperture correction we used is correct. For the void and comparison sample, the main part of the values of R_{21} lies below the line of $\bar{T}_{\mathrm{Bc2-1}}/\bar{T}_{\mathrm{Bc1-0}} = 0.7$, suggesting that the molecular gas is cold (< 10 K). Interestingly, many galaxies have $\bar{T}_{\mathrm{Bc2-1}}/\bar{T}_{\mathrm{Bc1-0}} < 0.5$, which might indicate the presence of low-density sub-thermally excited gas that is not in thermal equilibrium (Leroy et al. 2009; den Brok et al. 2021).

3.3 Discussion

The molecular gas masses for 20 objects presented in this thesis are the largest sample of void galaxies with molecular gas data so far. This enables us to statistically compare the properties of void galaxies to those galaxies in filaments and walls.

Our results show no significant difference in the mean $M_{\mathrm{H_2}}$ and $M_{\mathrm{H_2}}/M_\star$ for different mass bins compared to the control sample. The exception is the intermediate stellar mass bin, especially in the SF subsample, where $M_{\mathrm{H_2}}$ in void galaxies might be lower than for galaxies

$R_{21} = I_{CO(2-1)}/I_{CO(1-0)}$

Galaxies considered (1)	CO-VGS nº (2)	CO-VGS mean (3)	CO-VGS median (4)	CO-CS nº (5)	CO-CS mean (6)	CO-CS median (7)	CO-VGS - CO-CS Δmean (8)	CO-VGS - CO-CS σ (9)	CO-VGS - CO-CS KS (10)
Upper lim.	13/1	1.37 ± 0.19	1.19	50/0	1.37 ± 0.05	1.34	-0.00 ± 0.19	-0.01	1×10^{-3}
Lower lim.	14/1	1.74 ± 0.28	1.49	54/7	1.41 ± 0.05	1.34	0.33 ± 0.28	1.18	0.02

Table 3.15: **CO(2 − 1) − to − CO(1 − 0) line ratio.** In the mean, only galaxies with an aperture correction of $f_{ap} = 1.1 - 1.6$ were considered in order to make a consistent comparison. (1) Upper row: Only detections and upper limits were taken into account. Lower row: Only detections and lower limits were taken into account. (2) n: Number of CO-VGS galaxies in the bin. n_{up}: Number of upper limits of CO-VGS galaxies in the bin. (3) Mean emission line ratio of the CO-VGS galaxies in the bin taking lower limits into account. (4) Median emission line ratio of the CO-VGS galaxies in the bin. (5) - (7) The same for the CO-CS sample. (8) Difference of the mean emission line ratio between CO-VGS and CO-CS (Δmean) and its error (err(Δmean)). (9) σ = Δmean/err(Δmean). (10) p-value of the Kolmogorov-Smirnov test.

in filaments and walls. Our mean value for $M_{H_2}/M_\star$ of the SF sample ($\log_{10} M_{H_2}/M_\star = -1.2$) agrees with the values found by Castignani et al. (2021) for field and filament galaxies ($\log_{10} M_{H_2}/M_\star = -1.3$).

For the SFE, the CO-VGS and control sample also agree well. The SFE is lower for the CO-VGS in the lowest-mass bin, but the number of objects is small in this bin. The SFE of four VGS galaxies with stellar masses just below $10^{9.0}$M$_\odot$ agrees better with the mean SFE of the comparison sample for the lowest stellar mass bin ($M_\star$ between $10^{9.0}$ and $10^{9.5}$M$_\odot$). This indicates that the low mean SFE that we find for the CO-VGS in the low stellar mass bin needs to be confirmed for a larger sample of void galaxies before any firm conclusions can be drawn.

The atomic gas mass fraction in the void galaxies follows the trend of the control sample for $M_\star < 10^{9.0}$ M$_\odot$ quite well and has lower values for higher $M_\star$, drawing a steeper trend for void galaxies with $M_\star > 10^{9.0}$ M$_\odot$. This agrees with Kreckel et al. (2012), who found evidence for a slight lack of M_{HI} for $M_\star \gtrsim 10^{9.0}$ M$_\odot$ in void galaxies (for the same void galaxies as in our study, but for a different control sample). In contrast, Florez et al. (2021) found a small enhancement of M_{HI} in void galaxies (up to ~ 0.2 dex), especially for galaxies with $M_\star < 10^{9.5}$ M$_\odot$, for a sample of ~ 900 void galaxies and a control sample of ~ 8500 galaxies.

Castignani et al. (2021) found for late-type galaxies that the atomic gas mass fraction decreases with the local density on average from field ($\log_{10} M_{HI}/M_\star = -0.47$) and filaments ($\log_{10} M_{HI}/M_\star = -0.52$) to clusters ($\log_{10} M_{HI}/M_\star = -1.10$), which means that galaxies might be stripped of their gas while falling from field and filaments into clusters, or they might be affected by tidal interactions (Chung et al. 2021). We find similar average values in filaments ($\log_{10} M_{HI}/M_\star = -0.50$) and slightly higher values in voids ($\log_{10} M_{HI}/M_\star = -0.30$ for SF galaxies), where the density is lower (Kreckel et al. 2012; Pan et al. 2012), following the same trend. However, we find the opposite result for massive galaxies ($M_\star > 10^{9.5}$ M$_\odot$), where the atomic gas mass fraction is lower in void galaxies ($\sim 3\sigma$). If this discrepancy is confirmed for a larger number of void galaxies, it suggests that (because gas-stripping processes, such as ram pressure or frequent interactions, are unusual in voids) the lower atomic gas mass in massive void galaxies might be due to a gas deficiency in the inter-galactic medium of voids, or that slower gas accretion processes take place in void galaxies.

The mean molecular-to-atomic gas mass ratio is consistent with

that of the control sample, except for the highest stellar mass bin ($M_\star > 10^{10.0}$ $M_\odot$). As we do not find differences with the mass of the molecular gas between samples, the result for the highest-mass bin seems to be driven by the lower atomic gas mass of high-mass void galaxies with respect to the control sample. It may also be driven by the low number of VGS galaxies (three) in this stellar mass bin, however.

The mean sSFR values of the VGS are very close to the mean values of the CCS for the entire sample and for the SF sample. The mean value of the VGS is up to $|\sigma| \sim 3$ below that of the CCS for one individual mass bin, but no trends with stellar mass are visible. We thus do not find evidence for a general significant difference of the sSFR between the void and the control sample, and in particular, we do not find any evidence at all for an enhancement of the sSFR.

When we compare our results to those from the literature, we find that a number of other studies found no differences in the sSFR of void galaxies either (Patiri et al. 2006; Kreckel et al. 2012; Ricciardelli et al. 2014). Others found that voids are populated by galaxies with higher sSFR (Rojas et al. 2005; Beygu et al. 2016; Florez et al. 2021), however. The direct comparison is not straightforward, however, because the sample environment might play a role; for instance, Beygu et al. (2016) only use field and isolated galaxies for their comparison sample, but in the present work, we used the xCOLD GASS sample, which is a representative sample of SDSS galaxies in filaments and walls, after removing galaxies inhabiting voids or clusters. Furthermore, there seems to be a clear dependence on the SFR tracer that is used. In Appendix A.2 we show a comparison between the different SFR tracers we used for our control samples: Hα maps were used for the VGS galaxies (Beygu et al. 2016) and the HI-CALIFA sample (Catalán-Torrecilla et al. 2015), whereas the SFR of the xCOLD GASS sample was derived from Near-UltraViolet (NUV) and Mid-InfraRed (MIR) emission (Saintonge et al. 2017). In addition, the SFR from the MPA-JHU is frequently used in the literature (Patiri et al. 2006; Kreckel et al. 2012; Ricciardelli et al. 2014; Rojas et al. 2005) and is available for the VGS and the control samples. Our comparison in Appendix A.2 shows that the MPA-JHU SFR systematically gives higher SFRs for the void galaxies compared to the other methods, and that the effect increases for lower SFRs (Figure A.2.1). The comparison between the MPA-JHU and other SFR tracers for the xCOLD GASS and EDGE-CALIFA galaxies shows that this trend continues to higher

SFRs and suggests that the MPA-JHU progressively underestimates the SFRs with increasing SFR. These results might reflect a problem in the aperture correction (Duarte Puertas et al. 2017) as MPA-JHU seems to overestimate the SFR for compact galaxies such as the VGS (values of $R_{90} \sim 4 - 15$ arcsec) and underestimates the SFR for larger galaxies such the EDGE-CALIFA galaxies ($R_{90} \sim 20 - 45$ arcsec; see also Figure A.2.2, where we compare the different SFR tracers as a function of the apparent size of the galaxies). The SFR tracers used in our comparison are more robust (see Figure A.2.3). Thus, the use of different SFR tracers might explain the disagreement of our result compared to Patiri et al. (2006); Kreckel et al. (2012); Ricciardelli et al. (2014) and Rojas et al. (2005), who used the MPA-JHU SFR.

All this makes it difficult to draw any strong conclusion about the apparent disagreement with previous works, but it indicates that a revision of the subject is required that takes a careful look at the comparison sample and the SFR tracer used for the comparison. This is beyond the scope of this study, especially because we still lack enough number statistics to carry out a more detailed study. This is one of the scopes of CO-CAVITY, which will enhance the statistics.

There is no numerical prediction about the molecular gas content of void galaxies. Our finding of similar molecular gas masses or molecular gas mass fractions between void galaxies and the comparison sample is a clear constraint for future simulations of galaxy evolution in voids. Some numerical simulations (Cen 2011) predict that the cold-gas inflow rate at redshift z = 0 will be higher for void than for cluster galaxies, even more so in the low-mass range, but there are no predictions about the colder star-forming phase. These simulations predict a clearly higher sSFR for void galaxies with masses $10^{9}.0\,\mathrm{M}_{\odot} < M_{\star} < 10^{10.0}\,\mathrm{M}_{\odot}$ and only marginally higher for a higher mass range. Again, it is not straightforward to compare this prediction with our results, not only due to the low number statistics, but also because the simulations compare void galaxies with cluster galaxies and our comparison sample includes non-void environments and no cluster galaxies.

3.4 Conclusions

We observe the CO(1 − 0) and CO(2 − 1) emission lines of 20 void galaxies from the VGS with the IRAM 30 m telescope. The CO(1 − 0) line is detected for 13 galaxies and the CO(2 − 1) for 14 galaxies, al-

lowing us to derive the molecular gas mass for 15 detected galaxies and calculate upper limits for 5 non-detected galaxies. This represents the largest CO sample of void galaxies up to date.

We select a comparison sample from the xCOLD GASS and EDGE-CALIFA samples, which have available data for stellar mass, star formation rate, atomic gas mass, and molecular gas mass. Most of the VGS galaxies are star-forming main-sequence galaxies, but the control sample has many quiesicent galaxies with a low sSFR. To take this into account, we define star-forming sub-samples for the VGS and the control sample by selection galaxies close to the star-forming main sequence and carry out the entire analysis for these sub-samples as well. Based on these data and samples, we study the sSFR, the molecular gas mass, the molecular gas mass fraction, the SFE, the atomic gas mass fraction, and the molecular-to-atomic gas mass ratio by comparing the mean values of the void galaxies in different stellar mass bins to those of the control samples. The main conclusions are listed below.

1. We do not find any clear difference for the molecular gas mass or molecular gas mass fraction between void galaxies and the comparison sample. Void galaxies seem to have the same molecular gas fraction as galaxies in filaments and walls.

2. We do not find any evidence for differences in the SFE, except for the lowest-mass bin ($10^{9.0}\mathrm{M}_{\odot} \leq M_{\star} < 10^{9.5}$ $\mathrm{M}_{\odot}$), in which the SFE of void galaxies is significantly ($|\sigma| > 4$) below that of the control sample. However, due to the low number of galaxies in this sub-sample (four to five objects), the results need to be confirmed for a larger sample.

3. There is some evidence for a lower atomic gas mass fraction and a higher molecular-to-atomic gas mass ratio in void galaxies for $M_{\star} > 10^{9.5}$ and $M_{\star} > 10^{10.0}$ $\mathrm{M}_{\odot}$, respectively. The mean values for lower stellar masses are the same as for the control sample within the errors. Again, the results for the higher stellar masses need to be confirmed for larger sample because they are derived from a low number of galaxies (three to five objects).

4. We do not find any clear difference in the sSFR between void galaxies and the control sample, and in particular, we do not find an enhancement for void galaxies.

5. The CO$(2-1)$-to-CO$(1-0)$ line ratio does not show any clear difference between void galaxies and the control sample.

Our study was based on a small number of galaxies, and some of our conclusions are based on low number statistics. CO-CAVITY, together with CAVITY, plans to overcome this limitation by providing observational data of the star formation and ionized and neutral gas for a sample of several hundred void galaxies.

Chapter 4

Stellar population spectral analysis

Contents

In this chapter we carry out a non-parametric full spectral fitting analysis to derive the star formation histories and stellar metallicities of the void galaxies in the CAVITY mother sample (see Section 2.2), together with a comparison sample of galaxies in filaments & walls, and clusters (see Section 2.2.1). This spectral analysis recovers the stellar Line-Of-Sight Velocity Distribution (LOSVD), gas emission lines, and generates combinations of stellar population models that best fit the observed spectra of the galaxies in a wavelength range from 3750 to 5450 Å. From these combinations of models we can estimate the masses, ages, and metallicities of the stars within the galaxies.

For the analysed data we use optical spectra from the SDSS-DR7 (Abazajian et al. 2009), see Section 4.1. As stellar models we use the Extended Medium resolution INT Library of Empirical Spectra (E-MILES) templates (Sánchez-Blázquez et al. 2006; Falcón-Barroso et al. 2011; Vazdekis et al. 2015, 2016, see Section 4.2). With the Penalized Pixel-Fitting (pPXF) algorithm (Cappellari & Emsellem 2004; Cappellari 2017, 2022) we generate combinations of stellar population models (E-MILES) and pure Gaussian emission line templates that best fit the observed spectra of the galaxies, recovering the stellar LOSVD and gas emission (see Section 4.3). Afterwards we apply the STEllar Content and Kinematics from high resolution galactic spectra via Maximum A Posteriori (STECKMAP) algorithm (Ocvirk et al. 2006b,a) to recover the stellar populations (stellar masses, ages, and metallicities) of the galaxies by fitting combinations of E-MILES models (as for pPXF) to the clean spectra of the galaxies (only emission from the stars, without the emission lines previously fitted by pPXF), assuming fixed stellar LOSVDs (previously derived with pPXF), see Section 4.4. In Section 4.5 we describe the quality control that we apply to the results of our spectral analysis.

4.1 SDSS-DR7 spectra

The SDSS-DR7 (Abazajian et al. 2009) contains optical spectra for 1.6 million objects, including 930,000 galaxies, 120,000 quasars, and 460,000 stars observed at the Apache Point Observatory (APO) 2.5 m telescope. The SDSS spectra have a wavelength coverage from 3,800 to 9,200 Å, logarithmic wavelength sampling with a pixel separation of $69\,\mathrm{km\,s^{-1}}$ ($\Delta \log_{10}(\lambda) = 10^{-4}\,\mathrm{dex}$), and a variable spectral power resolution ranging from $\mathrm{R} \sim 1,500$ at 3,800 Å to $\mathrm{R} \sim 2,500$ at

9,000 Å. The instrumental dispersion of the SDSS spectra is variable (FWHM $\sim 2.00 - 3.00$ Å) inside the fitting wavelength range of our analysis ($3,750 - 5,450$ Å), and it is different for every galaxy. This is taken into account later in the analysis. The SDSS-DR7 spectra is integrated (fibre aperture with 3 arcsec diameter) in the very centre of the galaxies, from 0.3 to 1.6 kpc for the redshift range ($0.01 < z < 0.05$) of our sample of galaxies.

4.2 E-MILES stellar models

The E-MILES (Sánchez-Blázquez et al. 2006; Falcón-Barroso et al. 2011; Vazdekis et al. 2015, 2016) are Single-age Single-metallicity stellar Population (SSP) spectral templates generated assuming the BaSTI isochrones (Pietrinferni et al. 2004) and Kroupa universal IMF (Kroupa 2001). We expect that a change in the IMF would shift (García-Benito et al. 2019) our results, such as the age of the recovered stellar populations. However, as we assume the same IMF for the three large-scale environments, it will affect our SFHs equally regardless of the environment, and thus, relative differences between voids, filaments & walls and clusters should remain. These models cover a wavelength range from 1,680 to 50,000 Å with linear wavelength sampling with a pixel separation of 1.00 Å and a variable instrumental dispersion of FWHM between 2.51 and 23.57 Å, which is constant (2.51 Å) inside the fitting wavelength range ($3,750 - 5,450$ Å) of our analysis.

4.3 pPXF

The pPXF (Cappellari & Emsellem 2004; Cappellari 2017, 2022) algorithm implements a non-parametric full spectral fitting technique to recover the LOSVD of stars and emission lines. We assume Gaussian-Hermite LOSVD for the stars, and pure Gaussian LOSVD for the ionised gas. This algorithm uses stellar and gas spectral templates, chooses a combination of them, and convolves them with the LOSVD that best fit the spectra of the galaxies (see an example in Figure 4.1). We use the E-MILES stellar templates and, for the emission lines, we place several lines in the same template with fixed relative fluxes of emission-line doublets or Balmer series. The E-MILES stellar templates are synthetic or have been observed with different instruments than the one used to observe the spectra of the galaxies. This means

that the wavelength sampling and instrumental dispersion of the stellar templates (linear sampling and FWHM = 2.51 Å of instrumental dispersion) are different compared to the spectra of the galaxies (logarithmic and FWHM $\sim 2.00-3.00$ Å, respectively). Logarithmic sampling is preferable for pPXF because the LOSVD is constant with wavelength. We then re-sample the templates from linear to logarithmic wavelength sampling. We also need the templates and the spectra of the galaxies to have the same instrumental dispersion, so the line-width differences between them are only due to the LOSVD. Depending on the galaxy, the instrumental dispersion might be higher (up to 3.00 Å) or lower (down to 2.00 Å) than it is for the templates (2.51 Å), we then convolve both the templates and the spectrum of the galaxy to have the same instrumental dispersion, 3.00 Å. Furthermore, the possible under-sampling and the S/N of the spectrum play an important role in the limitations of pPXF to well determine the LOSVD.

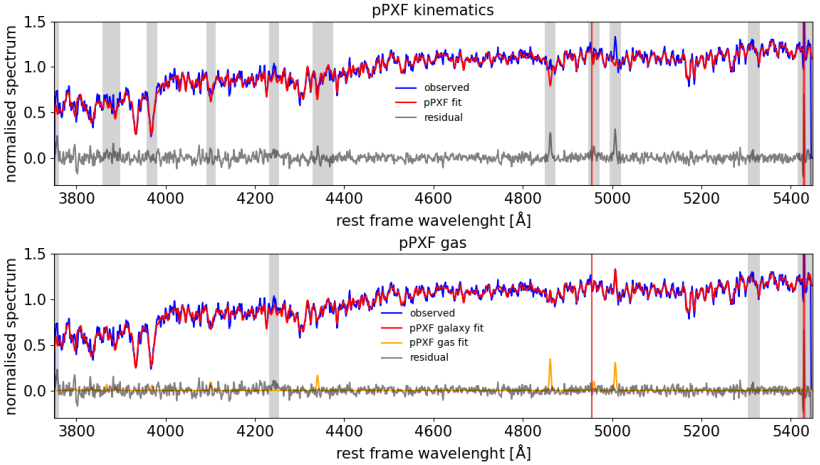

Figure 4.1: Example of the pPXF spectral fit for the galaxy CAVITY59013. The observed spectrum is in blue, the fitted spectrum by pPXF is in red, and the residual spectrum is in grey. In the upper panel we show the spectral fit of the stellar LOSVD by pPXF. Here we mask the gas and sky emission lines (grey vertical bands), and bad pixels (red vertical lines). pPXF fits the stellar populations to recover their LOSVD. The emission lines remain in the residual spectrum. In the lower panel we show the spectral fit of the gas emission lines. Here we only mask the sky emission lines, and bad pixels. pPXF fit both the setellar populations, and the emission lines (orange), with independent LOSVDs for stars, hydrogen Balmer lines, and the rest of gas emission lines. The emission lines do not remain in the residual spectrum.

The capability of pPXF to recover the LOSVD is limited by the under-sampling. When it works in pixel space and the velocity disper-

sion is lower than 2 pixels (138km s^{-1} for SDSS spectra), the Gaussian-Hermite parameter estimations increasingly scatter and shift from the real values (Cappellari & Emsellem 2004). However, when pPXF works in Fourier space, where the LOSVD is not under-sampled anymore, this problem is solved for the first and second order Gaussian-Hermite parameters (V, σ), but the third and forth (h_3, h_4) keep shifting towards zero, although the scatter is reduced (Cappellari & Emsellem 2004; Cappellari 2017). This means that the LOSVD is approximated as a pure gaussian distribution for low velocity dispersions. We expect emission lines to be narrow and under-sampled so we directly recover the LOSVD of the emission lines as pure gaussians, placing several lines in the same template with fixed relative fluxes of emission-line doublets or Balmer series.

Another potential problem for pPXF to recover the LOSVD is the age-dependent kinematics. Different stellar populations usually have different LOSVD, older stars in a virialised bulge, or younger stars in a rotating disc, for instance. In our study we use integrated spectra from the very centre of the galaxies. The median apparent radius of our samples is $R_{90r} \sim 8.3$ arcsec and the diameter of the SDSS spectrograph fibre is 3 arcsec, integrating around the 18% of the radius of the galaxy. We do not expect the age-dependent kinematics to affect our study.

Additionally, pPXF can simultaneously fit both stellar and gas kinematics, however, this is not recommended when recovering the LOSVD. In general, it its more recommended to obtain the stellar kinematics by masking the gas emission lines (together with sky emission lines and bad pixels reported in the the SDSS spectrum header), including additive polynomials to reduce template mismatch. Otherwise, the gas emission lines fluxes and their LOSVD are recovered from a separated pPXF fitting at fixed stellar kinematics, including multiplicative polynomials to prevent changes in the line strength of the absorption features in the templates (Cappellari & Emsellem 2004). The simultaneous fitting is useful to recover the stellar population. However, in this work we use another algorithm (STECKMAP) for this purpose.

4.4 STECKMAP

The STECKMAP (Ocvirk et al. 2006b,a) algorithm recovers the stellar populations of a galaxy as a combination of SSPs that are fitted to the observed spectrum of the galaxies, after removing the emission

lines and assuming fixed stellar LOSVD (both previously derived with pPXF); see an example of the spectral fit of STECKMAP in Figure 4.2. From this combination of SSPs we derive the stellar mass fraction, metallicity, and age of the currently living stars of the galaxy. We estimate the errors as the standard deviation of 5 Monte Carlo solutions of STECKMAP.

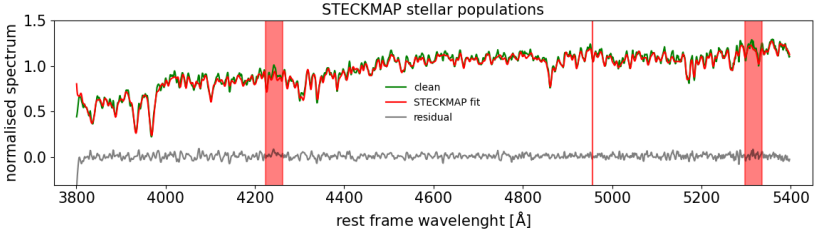

Figure 4.2: Example of the STECKMAP spectral fit for the galaxy CAVITY59013. The clean spectrum (observed spectrum without the emission lines, previously fitted by pPXF) is in green, the fitted spectrum by STECKMAP is in red, and the residual spectrum is in grey. Here we only mask the sky emission lines, and bad pixels (red vertical bands). STECKMAP only fits the stellar populations for a fixed LOSVD, previously fitted by pPXF.

The recovered stellar populations are affected by the age-metallicity degeneracy of the stars (Worthey 1994), and young metal-poor galaxies might have been classified as old metal-rich. This effect is due to the fact that old stars with low metallicities have similar spectra as young stars with high metallicities. This might be a problem for STECKMAP when it tries to fit stellar models with two-dimensional (2D) stellar age and metallicity distribution $\Lambda(t, Z)$ even for high quality spectra ($S/N < 500$). The age-metallicity degeneracy is stronger for old stellar populations than it is for younger ones, this means that the spectrum of a young star changes faster in time than an older one. For this reason we use a logarithmic age binning for the SFHs, having large age bins for old stellar populations and narrower bins for younger ones. STECKMAP can only tell these small spectral differences for really high S/N ratios (≥ 500). However, this data quality is not reachable for extra-galactic observations, so they give a solution by using SSPs.

The age-metallicity degeneracy is not a major problem applying STECKMAP when it assigns only one age and one metallicity (i.e. SSP stellar models, not a 2D distribution anymore) to the stellar population, having $\Lambda(t)$ and $Z(t)$. Then, according to the STECKMAP quality tests (Ocvirk et al. 2006b,a), we expect age and metallicity errors lower than 0.08 dex for a $S/N \sim 20$, a spectral power resolution of $R \sim 2500$, and

10 Monte Carlo solutions. These errors decrease (down to 0.02 dex for age, and 0.04 for metallicity) when the S/N increases (up to 200), but do not change significantly for lower (down to R $\sim$ 1000) or higher (up to R $\sim$ 10000) spectral power resolutions. Then, although we run fewer Monte Carlo solutions (5 per galaxy), the SDSS spectral power resolution is around R $\sim$ 2000 in the fitting wavelength range that we use in this study, and the minimum S/N of our sample selection is 20 with many galaxies above this value. We then expect to have age and metallicity errors not much higher than 0.08 dex for individual galaxies (up to 0.11 dex $\sim$ 0.08 dex/$\sqrt{5/10}$ in some cases). However, in our study, we do not compare individual galaxies but the mean of hundreds of them (more than 100 galaxies per stellar mass bin), so we expect that the errors for the mean age and metallicity will be below 0.01 dex $\sim$ 0.08 dex/$\sqrt{100}$.

Additionally, Sánchez-Blázquez et al. (2011) analysed the effect of the age-metallicity degeneracy for STECKMAP using synthetic spectra of ages 1 and 10 Gyr and solar metallicity (0 dex), and compared with other spectral index techniques. It can be seen in their Figure 7 that the age-metallicity degeneracy effect is much more reduced in the case of STECKMAP (ages of $\sim 1.00\pm0.04$ Gy and $\sim 11\pm1$ Gy, respectively, and metallicities of $\sim 0.02\pm0.04$ dex) than in the case of spectral indices (ages of $\sim 1.0\pm0.1$ Gy and $\sim 10\pm5$ Gy, respectively, and metallicities of $\sim -0.1\pm0.2$ dex).

4.5 Quality control

After applying this analysis to our samples of galaxies in voids (2,545 objects), filaments & walls (15,000), and clusters (6,189), we carry out a quality control to identify and remove the bad-fitted spectra. The quality of the outcome of the spectral fitting techniques is affected by the S/N of the continuum ($6000-6100$ Å, rest frame) and the intensity of the emission lines, among others. A good indicator of the quality of the spectral fit is the residual spectrum, which is the difference between the observed and fitted spectrum. If the residuals are large, it may mean that the observed spectrum is noisy, or that the fitted spectrum is not a perfect match to the observed one. In Figure 4.3a we show the standard deviation of the fit residual normalised by the level of continuum over Hβ ($\sigma_{\rm res}$(Hβ)/Cont) vs. the S/N of the continuum, the equivalent width of Hβ (ΔH$\beta_{\rm eq}$) is colour-coded. Here we see how

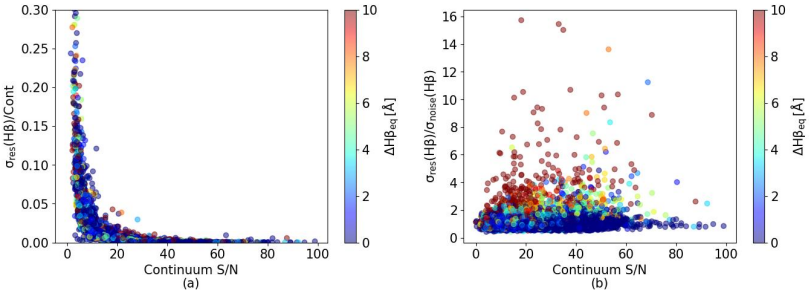

Figure 4.3: **Fit residuals vs. spectral signal-to-noise, and emission lines.** (a) Standard deviation of the spectral fit residual ($\sigma_{\rm res}$(Hβ)) normalised by the level of the continuum (Cont) around Hβ vs. S/N of the continuum. (b) Residual-to-noise ratio as ($\sigma_{\rm res}$(Hβ)) normalised by standard deviation of noise in the continuum next to Hβ ($\sigma_{\rm noise}$(Hβ)) vs. the S/N of the continuum. The Hβ equivalent with (ΔH$\beta_{\rm eq}$) is colour-coded in both panels.

the fit quality (stellar and gas emission) is affected by the S/N. The level of fit residual, relative to the continuum, decreases with S/N. We remove from our sample a fraction of galaxies (61% in voids, 57% in filaments & walls, and 46% in clusters) with S/N$<$ 20, for which the residuals are higher than 2% of the continuum level. This selection by S/N removes from our samples mainly low-mass galaxies. In order to check that this does not introduce any bias in our study, we define sub-samples with the same stellar mass distribution (see Section 2.2.3).

Some galaxies have a high S/N ($>$ 20) spectrum, and residuals lower than 2% of the continuum level but larger than the level of noise. This is due to a bad fit of the gas emission lines. The pPXF algorithm is not efficient fitting very intense, asymmetric, or non-gaussian emission lines and may generate high fit residuals. These residuals are small compared to the continuum (below 2%) in bright galaxies but may be higher than the level of noise. These residuals may leave wavy features in the clean spectrum that consequently affect the STECKMAP fit and lead to recover wrong stellar populations. In Figure 4.3b we show the residual-to-noise ratio as the standard deviation of the residual over Hβ normalised by standard deviation of noise in the continuum also over Hβ ($\sigma_{\rm res}$(Hβ)/$\sigma_{\rm noise}$(Hβ)), vs. the S/N of the continuum, ΔH$\beta_{\rm eq}$ is colour-coded. Here we see that some bright galaxies (with intense emission lines in general) have the level of residual much higher than the level of noise. After a careful visual inspection, we confirm that these galaxies have featured residuals due to asymmetric, wide, or non-gaussian emission lines that pPXF is not able to fit

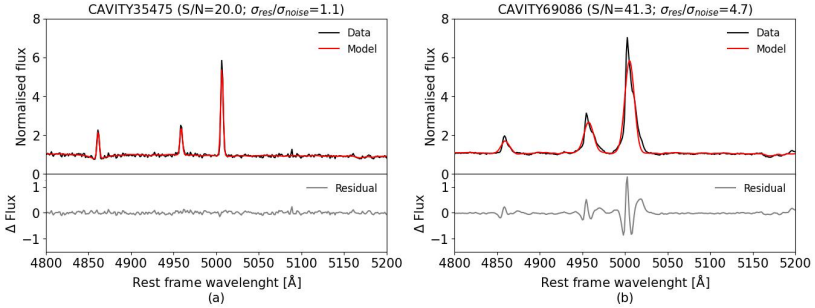

Figure 4.4: **Examples of pPXF spectral fit of emission lines.** (a) Good fit example of a galaxy with signal-to-noise ratio of S/N = 20.0 and residual-to-noise ratio of $\sigma_{\rm res}/\sigma_{\rm noise} = 1.1$. (b) Bad fit example of a galaxy with S/N = 41.3 and $\sigma_{\rm res}/\sigma_{\rm noise} = 4.7$. The black and red lines represent the observed and the fitted spectrum of the galaxy, respectively. The grey lines represent the fit residuals.

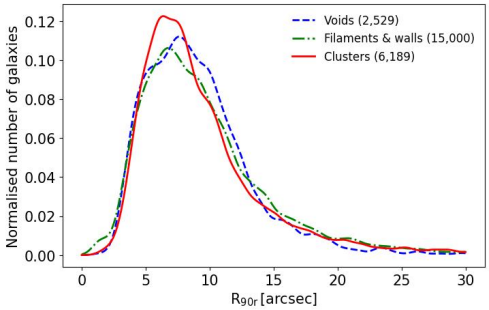

Figure 4.5: **Distribution of apparent radius.** Normalised number of galaxies as a function of the apparent radius (R_{90r} from SDSS) for galaxies in voids (blue dashed line), filaments & walls (green dot-dashed line), and clusters (red solid line) before the quality control. The apparent radius of the galaxies is represented by the petrosian radius containing the 90% of the total flux of the galaxy in r band (SDSS, Ahumada et al. 2020).

properly (see good and bad fit examples in Figure 4.4). We consider that $\sigma_{\rm res}(\mathrm{H}\beta)/\sigma_{\rm noise}(\mathrm{H}\beta) \leq 2.0$ provides good quality fit, and we remove from our samples small fractions of galaxies (5% in voids, 8% in filaments & walls, and 7% in clusters) with a high S/N (> 20) spectrum and residuals twice higher than the level of noise over Hβ after subtracting the emission lines. These small percentages of removed galaxies does not introduce any bias in our analysis.

In addition, as the final step in our quality control, we take into account the aperture effect in the SDSS spectra. The optical spectra from SDSS are integrated over the central region of the galaxies (fibre aperture with 3 arcsec diameter). This might introduce a bias for samples covering a large redshift range where this aperture would cover only the inner region of the nearby objects, but a large fraction of the galaxy for the distant ones. However, the redshift range of our samples is rather

narrow ($0.01 - 0.05$), and their apparent size (r-Petrosian radius, R_{90r}, from SDSS) distributions are very similar for the three environments (see Figure 4.5), with absolute apertures ranging from 0.3 to 1.6 kpc. In order to minimise a possible size effect in our study, we remove from our samples a small fraction (1% in voids, 4% in filaments & walls, and 5% in clusters) of galaxies with $R_{90r} > 20$ arcsec, for which the spectrum would be relatively more influenced by the fibre aperture. The aperture effect only affects our study in the sense that our results are only valid for the centre of the galaxies. After this quality control we are left with 987 galaxies in voids, 6463 in filaments & walls, and 3357 in clusters, which are the samples of study in chapters 5 and 6.

Chapter 5

Star formation histories

Contents

Here we characterise the SFH of thousands of galaxies inhabiting the three large-scale environments: voids, filaments & walls, and clusters (see Chapter 2 for a further description of the sample selection). We derive the SFHs applying a combination of tested full spectral fitting techniques codes (pPXF and STECKMAP, Cappellari & Emsellem 2004; Cappellari 2017, 2022; Ocvirk et al. 2006b,a) to the optical spectra from SDSS Data Release 7 (Abazajian et al. 2009) using the E-MILES (Sánchez-Blázquez et al. 2006; Falcón-Barroso et al. 2011; Vazdekis et al. 2015, 2016) stellar model templates (see Chapter 4 for a complete description of the spectral data and analysis).

The stellar populations recovered by STECKMAP (see Section 4.4) are characterised by the mass, age, and metallicity of the stars within the galaxy. However, it does not consider the stars that are already dead. We apply a correction factor (which depends on the age and metallicity of each stellar population and is provided by the MILES group [1]) to the current stellar mass fractions, in order to take into account the stars that were formed at a given cosmic look-back time but are not alive any more. For this purpose we follow the prescriptions in Vazdekis et al. (1996); Blakeslee et al. (2001); Vazdekis et al. (2010), using BaSTI isochrones (Pietrinferni et al. 2004) and Kroupa IMF (Kroupa 2001). Finally, from these stellar population ages, and corrected stellar mass fractions, we derive the SFH of a galaxy, as the stellar mass fraction formed at a given look-back time (see examples of SFHs in Figure 5.1 for two individual galaxies), where 0 Gyr is the present. As representative quantities of the stellar mass assembly rate, we define the assembly times of 50% (T_{50}) and 70% (T_{70}) of the stellar mass (dotted lines in right panel of Figure 5.1), for which we find that the difference in SFH are maximal. By definition, $T_{100} = 0$ Gyr means that the galaxy forms 100% of its stellar mass today, and T_{70} and T_{50} are correlated, i.e. if T_{50} is higher in a sample, the T_{70} is also higher. We repeat this for the 5 Monte Carlo solutions from STECKMAP to estimate the errors as the standard deviation.

This chapter is based on Domínguez-Gómez et al. (in press) and is organised in four sections. In Section 5.1 we present the SFH bimodality. In Section 5.2 we compare the mass assembly time of galaxies in different large-scale environments for a given stellar mass. In Section 5.3 we discuss our results and suggest several physical processes that might have caused the SFH differences that we find between galaxies

[1] http://research.iac.es/proyecto/miles/pages/predicted-masses-and-photometric-observables-based-on-photometric-libraries.php

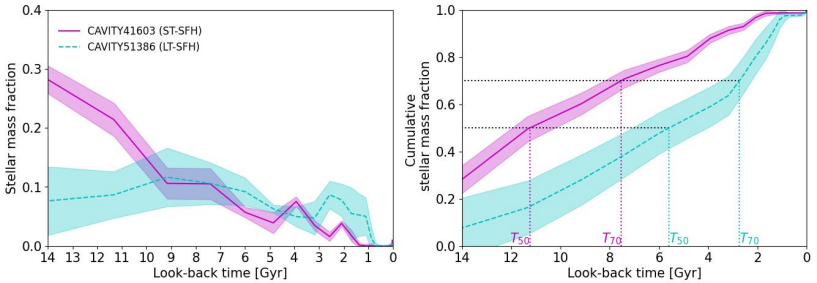

Figure 5.1: **Examples of star formation histories.** SFHs (left panel), and cumulative SFHs (right panel) for galaxies CAVITY59013 (solid magenta line) and CAVITY66461 (dashed cyan line), which have ST-SFH and LT-SFH types, respectively. The shaded regions represent the errors of the stellar mass fraction of the SFH. The dotted lines in right panel represent the assembly times of the 50% (T_{50}) and 70% (T_{70}) of the stellar mass.

in different large-scale environments. We summarise our conclusion in Section 5.4.

5.1 SFH bimodality

We show in Figure 5.2 the average cumulative SFH of galaxies in voids (blue dashed line), filament & walls (green dot-dashed line), and clusters (red solid line). The standard error of the mean (s.e.m.) of the average SFH is smaller than the thickness of the line. Dotted lines represent the assembly times of 50% (T_{50}) and 70% (T_{70}) of the stellar mass. We find that, on average, galaxies in voids assemble 50% and 70% of their stellar mass later than in filaments & walls by 1.03 ± 0.06 and 1.20 ± 0.05 Gyr, respectively, and much later than in clusters (by 1.91 ± 0.06 and 2.43 ± 0.05 Gyr). In addition, we show in Figure 5.3 the distribution of the cumulative SFH at 12.5 Gyr. We find that the SFHs at early times describe a bimodal distribution around the average in the three large-scale environments. We then classify the SFHs in two types: the Short-Timescale SFH (ST-SFH) is characterised by a high star formation (∼27% of the total stellar mass, the peak of the distributions) happening at the earliest time, while the Long-Timescale SFH (LT-SFH) has a star formation happening more uniformly over time. The distinction between these two types of SFHs allows us to evaluate the role of the large-scale environment in star formation, comparing the shape of the SFHs and assembly times between all three large-scale environments, and also paying attention to the probability of finding

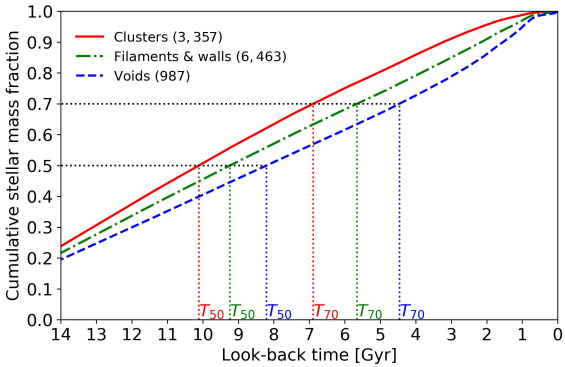

Figure 5.2: **Average cumulative star formation history.** Cumulative stellar mass fraction formed at a given look-back time, for galaxies in voids (blue dashed line), filaments & walls (green dot-dashed line), and clusters (red solid line). The used samples take into account the selection criteria applied by the quality control analysis (see Section 4.5) and are based on different stellar mass distributions (see Section 2.2.2). The dotted lines depict the average assembly times of 50% (T_{50}) and 70% (T_{70}) of the stellar mass. In general, the standard error of the mean (s.e.m., 1σ) is smaller than the line width of the curves. The number of galaxies are represented in the legend for each large-scale environment.

each SFH type in voids, filaments & walls, and clusters (see Figure 5.1 for the exact shape and differences between two ST-SFH and LT-SFH example galaxies).

Although it might be tempting to associate the SFH bi-modality with the current galaxy colour, and morphology, the SFH types do not clearly correlate with the bimodal colour or morphology distributions. We analyse the fraction of galaxies with different SFH types, colours, and morphologies to determine if there is a correlation between the SFH type of a galaxy and its current colour or morphology. We use the g and r dereddened magnitudes from the SDSS to define the colour of the galaxies as $g-r$. Here we define that galaxies with $g-r \leq 0.7$ mag are blue, and galaxies with $g-r > 0.7$ mag are red. We also use the T-type parameter from Domínguez Sánchez et al. (2018) to define the morphology of the SDSS galaxies. Galaxies with T-type < 0 are elliptical and galaxies with T-type > 0 are spiral.

We show in Figure 5.4 the fraction of spiral and elliptical galaxies (upper panels), or blue and red galaxies (lower panels) with ST-SFH and LT-SFH types after the quality control (see Section 4.5): for all the galaxies (left column), galaxies in voids (centre-left column), galaxies in filaments & walls (centre-right column), and galaxies in clusters (right

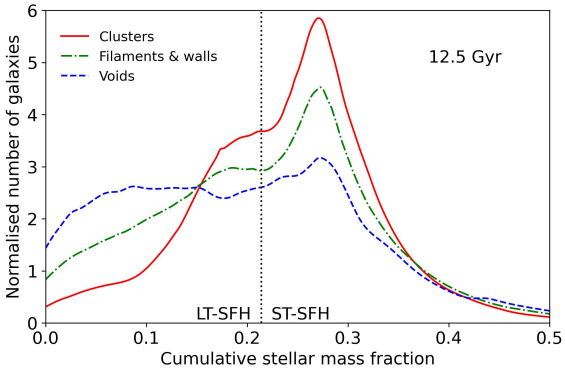

Figure 5.3: **Bimodal distributions of the cumulative star formation histories at 12.5 Gyr.** Normalised number of galaxies vs. the cumulative stellar mass fraction. The used samples take into account the selection criteria applied by the quality control analysis (see Section 4.5) and are based on different stellar mass distributions (see Section 2.2.2). The SFHs are classified into ST-SFH or LT-SFH using the vertical dotted line at 21.4% (relative minimum of the sample of galaxies in filament & walls and the inflexion point of the sample of galaxies in clusters) of the stellar mass as a classification criterion, which splits the distributions into two areas, which represent the probability of a galaxy to have one of the SFH types in each large-scale environment.

column). Not all the galaxies in our samples have an estimation of the T-type morphological parameter, reducing the number statistics for the morphological study (see the number of galaxies over each panel of Figure 5.4). In Figure 5.5 we show the same comparison for the galaxy samples with the same stellar mass distribution (see Section 2.2.3), for which we find similar results.

In general, considering all the galaxies regardless of their large-scale environment, we find that galaxies are more likely to be elliptical with ST-SFH (34.0%), or spiral with LT-SFH (27.9%). However, there is also a significant fraction of elliptical galaxies with LT-SFH (16.4%), and spiral galaxies with ST-SFH (21.6%). The probability of a galaxy to be spiral with a LT-SFH (27.9%) is very similar to be spiral with a ST-SFH (21.6%). Voids galaxies are more likely to be spiral with a LT-SFH (40.9%). However, the probabilities of a void galaxy to be elliptical with a LT-SFH (15.0%) or with a ST-SFH (19.8%) are comparable. The probabilities of a void galaxy to be spiral with a ST-SFH (24.3%) or to be elliptical also with a ST-SFH (19.8%) are comparable as well. Cluster galaxies are more likely to be elliptical with a ST-SFH (46.4%). However, the probabilities of a cluster galaxy to be spiral with a LT-SFH (18.2%) or with a ST-SFH (16.4%) are very

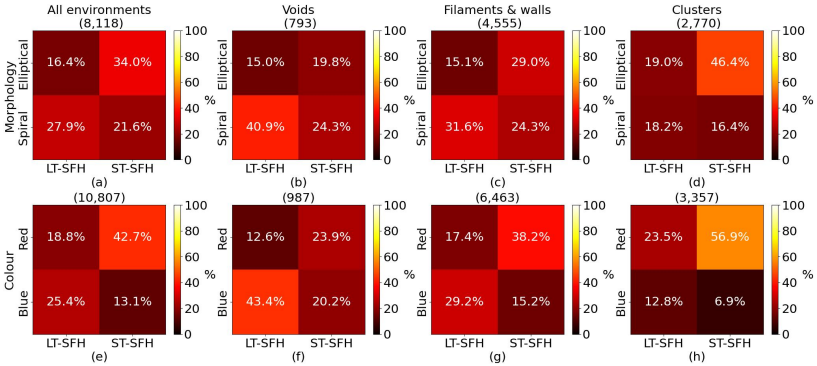

Figure 5.4: **Correlation between the star formation history type, current morphology and colour of the galaxy.** Fraction of spiral and elliptical galaxies, or blue and red galaxies with LT-SFH and ST-SFH types is shown for all the environments together (a, e), for voids (b, f), filaments & walls (c, g), and clusters (d, h), with the same stellar mass distribution. The number of galaxies is shown between brackets over each panel. Galaxies are blue if their $g - r < 0.7$, red if $g - r > 0.7$, spiral if T-type> 0 (Domínguez Sánchez et al. 2018), and elliptical if T-type< 0. Galaxies with ST-SFH are more likely to be elliptical or red. On the contrary, galaxies with LT-SFH are more likely to be spiral or blue. However, there is a significant fraction galaxies with ST-SFHs that are blue or spiral, and galaxies with LT-SFHs that are red or elliptical.

close. The probabilities of a cluster galaxy to be spiral with a LT-SFH (18.3%) or to be elliptical also with a LT-SFH (19.8%) are also similar. Galaxies in filaments & walls follow the general case (left panels).

We find a similar relation between the SFH type and the current colour of the galaxies. If we consider all the galaxies regardless of their large-scale environment, we find that galaxies are more likely to be red with a ST-SFH (42.7%) or blue with a LT-SFH (25.4%) but there is a significant fraction of red galaxies with a LT-SFH (18.8%), and blue galaxies with a ST-SFH (13.1%). Void galaxies are more likely to be blue with a LT-SFH (43.4%). However, the probabilities of a void galaxy to be blue with a ST-SFH (20.2%) or red also with a ST-SFH (23.9%) are comparable. Cluster galaxies are very likely to be red with ST-SFH (56.9%) but there is a significant fraction of red cluster galaxies with a LT-SFH (23.5%). Galaxies in filaments & walls follow the general case (left panels).

Although there is certain relation, we conclude that the SFH type do not clearly correlates with the current colour or morphology of the galaxy. The SFH type determine the evolution of a galaxy in general, along its entire life. However, the colour and morphology are associated with current properties of the galaxy, which should not be that strongly

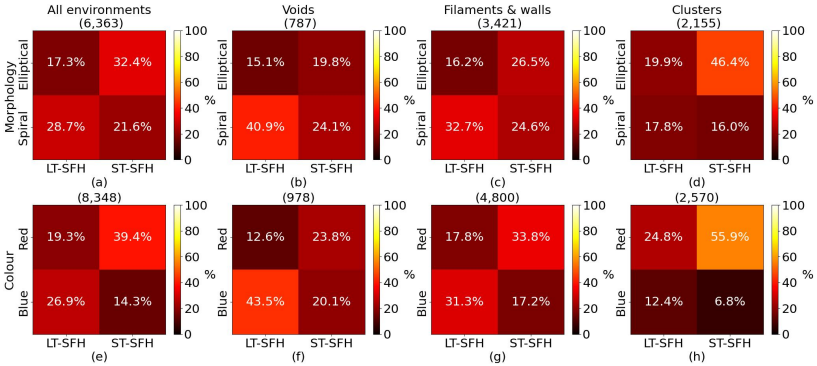

Figure 5.5: Same as Figure 5.4 for the samples with the same stellar mass distribution

affected by the overall SFH type (shape) but by the most recent stages of the SFH or the current environmental state or physical conditions (gas content, interactions, gas accretion, etc.).

We show in Figure 5.6 the average cumulative SFH of galaxies with ST-SFHs (thin lines) and galaxies with LT-SFHs (thick lines). We find that galaxies with ST-SFHs assembled on average 30% of their stellar mass at early times ($\sim$ 12.5 Gyr ago), and decrease their star formation later in their lives. Galaxies with LT-SFHs, however, have assembled a lower stellar mass fraction ($\sim$15%) at early times. By definition, ST-SFH galaxies assemble their stellar mass earlier than LT-SFH. It is more likely for a void galaxy to have a LT-SFH ($51.7 \pm 0.9\%$) than for those in filaments & walls ($44.5 \pm 0.3\%$) or clusters ($36.1 \pm 0.5\%$, see legends in Figure 5.6). Galaxies with ST-SFHs, on average, assemble their stellar mass at similar rates in the three large-scale environments. Galaxies with LT-SFHs, on average, assemble 50% and 70% of their stellar mass slower in voids than in filaments & walls by 1.05 ± 0.09 and 0.86 ± 0.06 Gyr, respectively; and much slower than in clusters (by 2.38 ± 0.10 and 2.22 ± 0.07 Gyr). These might be the main reasons why we find in Figure 5.2 that galaxies, on average, assemble their stellar mass later in voids than in denser large-scale environments. However, the stellar mass distributions of these galaxy samples depend on the large-scale environment (Rojas et al. 2005), galaxies in voids are on average less massive than galaxies in denser large-scale environments (see Figures 2.4 and 2.5), and it is necessary to test how these differences affect our results carrying out further comparisons for a given stellar mass.

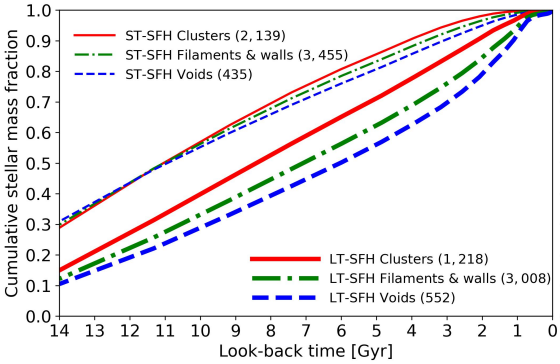

Figure 5.6: **Two types of star formation histories.** Cumulative stellar mass fraction formed at a given look-back time (in Giga years, Gyr) for galaxies with ST-SFH (thin lines) and LT-SFH (thick lines), in voids (blue dashed lines), filaments & walls (green dot-dashed lines), and clusters (red solid lines). The used samples take into account the selection criteria applied by the quality control analysis (see Section 4.5) and are based on different stellar mass distributions (see Section 2.2.2). In general, the s.e.m. (1σ) is smaller than the line width of the curves. The number of galaxies for each large-scale environment and SFH type are given in the legends.

5.2 Assembly time vs. stellar mass

We define three new sub-samples with the same stellar mass distribution (see Section 2.2.3). We show in in Figure 5.7 the median assembly times (T_{50} in the upper panels, and T_{50} in the lower panels), as a function of the stellar mass, for all the galaxies regardless of their SFH type (left panels), galaxies with ST-SFHs (middle panels), and galaxies with LT-SFHs (right panels). Galaxies in voids are represented by blue triangles, galaxies in filaments & walls by green squares, and galaxies in clusters by red circles. We find in Figure 5.7 (a) and (d) that, regardless of their SFH type, cluster galaxies, on average, assemble their stellar mass faster than galaxies in voids, and filaments & walls at any given stellar mass, except for very high stellar masses ($10^{10.5} \leq M_{\star}[\mathrm{M}_{\odot}] \leq 10^{11.0}$) where galaxies assemble their stellar mass at the same time in all the three large-scale environments. Very low-mass ($10^{8.5} \leq M_{\star}[\mathrm{M}_{\odot}] \leq 10^{9.0}$) and high-mass ($10^{10.0} \leq M_{\star}[\mathrm{M}_{\odot}] \leq 10^{11.0}$) galaxies, on average, assemble 50% and 70% of their stellar mass at the same rate in voids and filaments & walls. Low-mass ($10^{9.0} \leq M_{\star}[\mathrm{M}_{\odot}] \leq 10^{9.5}$) galaxies also have similar T_{50} values in voids and filaments & walls. However, they are later affected by their large-scale environment in this stellar mass bin

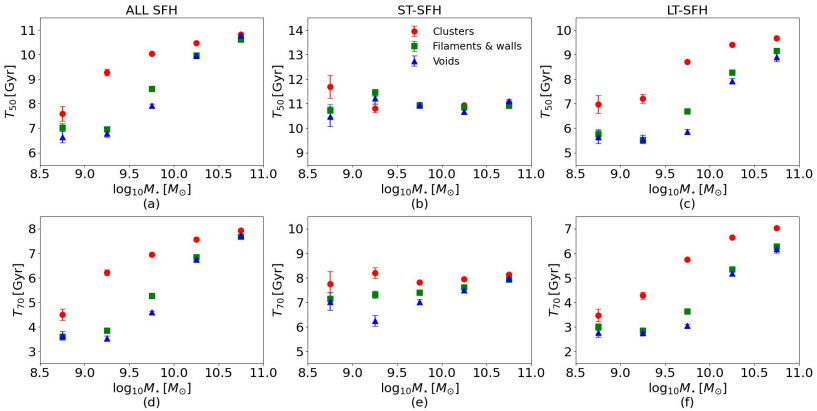

Figure 5.7: **Median assembly times vs. stellar mass.** Assembly time (in Giga years, Gyr) of 50% (T_{50}) and 70% (T_{70}) of the stellar mass for all the SFH types (a and d, respectively), galaxies with ST-SFH (b and e), and LT-SFH (c, f), in voids (blue triangles), filaments & walls (green squares), and clusters (red circles). The used samples take into account the selection criteria applied by the quality control analysis and are based on the same stellar mass distributions inside every stellar mass bin. The error bars represent the s.e.m. (1σ). The values and errors represented in this figure are shown in Table 5.1, together with the number (and fraction of the SFH types) of galaxies in each large-scale environment and stellar mass bin.

($10^{9.0} \leq M_\star[\mathrm{M}_\odot] \leq 10^{9.5}$), slightly delaying the T_{70} in void galaxies compared to galaxies in filaments & walls by 0.27 ± 0.13 Gyr. Galaxies with intermediate stellar masses ($10^{9.5} \leq M_\star[\mathrm{M}_\odot] \leq 10^{10.0}$) assemble both 50% and 70% of their stellar mass slower in voids than in filaments & walls by 0.69 ± 0.09 and 0.66 ± 0.07 Gyr, respectively.

Figures 5.7 (b) to (f) show the same info as Figure 5.7 (a) and (d) but distinguishing between ST-SFH and LT-SFH. We find in Figure 5.7 (b) that galaxies with ST-SFHs assemble 50% of their stellar mass at nearly the same time ($\sim$ 11 Gyr) independently of the large-scale environment and the stellar mass. However, at the lowest stellar mass bin, the number of galaxies is statistically low (8, 24, and 9 galaxies) for a strong conclusion. We also find in Figure 5.7 (e) that galaxies with ST-SFHs are later affected by their large-scale environment, delaying the T_{70} in void galaxies compared to galaxies in filaments & walls, and much more compared to galaxies in clusters. This delay is more relevant for low-mass ($10^{9.0} \leq M_\star[\mathrm{M}_\odot] \leq 10^{9.5}$) and intermediate-mass ($10^{9.5} \leq M_\star[\mathrm{M}_\odot] \leq 10^{10.0}$) galaxies, where void galaxies assemble 70% of their stellar mass slower than galaxies in filaments & walls by 1.07 ± 0.27 Gyr and 0.37 ± 0.12 Gyr, respectively; and much slower

than galaxies in clusters by 1.94 ± 0.31 Gyr and 0.79 ± 0.12 Gyr. The T_{70} barely depends on the stellar mass for galaxies with ST-SFHs in clusters (~ 8 Gyr) but it does for those in voids and filaments & walls. Massive ($10^{10.5} \leq M_{\star}[\mathrm{M}_{\odot}] \leq 10^{11.0}$) galaxies with ST-SFHs assemble 70% of their stellar mass faster than low-mass ($10^{9.0} \leq M_{\star}[\mathrm{M}_{\odot}] \leq 10^{9.5}$) galaxies in filaments & walls by 0.61 ± 0.15 Gyr, and much faster in voids by 1.72 ± 0.23 Gyr.

The stellar mass assembly rate of galaxies with LT-SFHs continuously depends on their large-scale environment and stellar mass. We find in Figure 5.7 (c) that massive ($10^{10.5} \leq M_{\star}[\mathrm{M}_{\odot}] \leq 10^{11.0}$) galaxies with LT-SFHs assemble 50% and 70% of their stellar mass faster than low-mass ($10^{9.0} \leq M_{\star}[\mathrm{M}_{\odot}] \leq 10^{9.5}$) galaxies: by 3.35 ± 0.25 Gyr in voids, by 3.63 ± 0.13 Gyr in filaments & walls, and by 2.47 ± 0.36 Gyr in clusters. Cluster galaxies with LT-SFHs assemble 50% and 70% of their stellar mass faster than galaxies in voids and filaments & walls at any given stellar mass. Void galaxies with LT-SFHs assemble 50% of their stellar mass slower than galaxies in filaments & walls at intermediate stellar masses ($10^{9.5} \leq M_{\star}[\mathrm{M}_{\odot}] \leq 10^{10.0}$), and slightly slower at high stellar masses ($10^{10.0} \leq M_{\star}[\mathrm{M}_{\odot}] \leq 10^{10.5}$) by 0.84 ± 0.11 Gyr, and 0.36 ± 0.10 Gyr, respectively. However, these differences only remain later (at T_{70}) in their evolution by 0.60 ± 0.08 Gyr at intermediate stellar masses. Void and filament & wall galaxies with LT-SFHs assemble 50% and 70% of their stellar mass at similar rates at lower ($M_{\star}[\mathrm{M}_{\odot}] < 10^{9.5}$) or higher ($M_{\star}[\mathrm{M}_{\odot}] > 10^{10.5}$) stellar masses.

5.3 Discussion

We find in Figure 5.7 (b) that galaxies with ST-SFHs, on average, have formed 50% of their stars very early (~ 11 Gyr ago), independently of their large-scale environment and stellar mass. This suggests that, in the early Universe, the density contrasts between the upcoming large-scale environments were not strong enough to create a difference in the assembly rate between the galaxies that were forming at that time. The assembly time differences that we find for galaxies with ST-SFHs are only imprinted later on in their evolution (e.g. T_{70}, see Figure 5.7 (e)), when the large-scale environment does play a role.

Whereas galaxies in clusters with ST-SFH exhibit similar assembly times for any given stellar mass ($T_{70} \sim 8$ Gyr), void and filament & wall galaxies, at some point, slow down their evolution compared to

$\log_{10} M_\star$[$M_\odot$]	Voids n(%)	Voids T_{50} [Gyr]	Voids T_{70} [Gyr]	Filaments & walls n(%)	Filaments & walls T_{50} [Gyr]	Filaments & walls T_{70} [Gyr]	Clusters n(%)	Clusters T_{50} [Gyr]	Clusters T_{70} [Gyr]
(a) All SFH									
8.5-9.0	56	6.64±0.23	3.64±0.17	105	7.03±0.16	3.60±0.12	30	7.59±0.29	4.50±0.24
9.0-9.5	159	6.79±0.14	3.53±0.11	326	6.95±0.09	3.84±0.07	100	9.27±0.13	6.22±0.12
9.5-10.0	363	7.92±0.08	4.60±0.06	1500	8.61±0.04	5.26±0.03	855	10.03±0.04	6.94±0.04
10.0-10.5	309	9.95±0.06	6.74±0.05	2199	9.97±0.02	6.84±0.02	1212	10.47±0.02	7.57±0.02
10.5-11.0	91	10.79±0.07	7.73±0.07	670	10.62±0.03	7.69±0.03	373	10.82±0.03	7.93±0.03
(b) ST-SFH									
8.5-9.0	8(14%)	10.47±0.39	7.04±0.36	24(23%)	10.72±0.26	7.15±0.25	9(30%)	11.69±0.47	7.75±0.51
9.0-9.5	40(25%)	11.23±0.24	6.25±0.22	80(25%)	11.45±0.14	7.32±0.15	39(39%)	10.81±0.18	8.19±0.22
9.5-10.0	127(35%)	10.94±0.11	7.02±0.11	602(40%)	10.92±0.05	7.39±0.05	463(54%)	10.96±0.05	7.81±0.05
10.0-10.5	187(61%)	10.67±0.07	7.50±0.07	1263(57%)	10.86±0.03	7.61±0.03	820(68%)	10.94±0.03	7.94±0.03
10.5-11.0	68(75%)	11.10±0.07	7.97±0.08	476(71%)	10.93±0.03	7.93±0.03	282(76%)	11.05±0.03	8.12±0.03
(c) LT-SFH									
8.5-9.0	48(86%)	5.64±0.26	2.77±0.19	81(77%)	5.76±0.20	3.00±0.14	21(70%)	6.97±0.36	3.47±0.26
9.0-9.5	119(75%)	5.55±0.17	2.76±0.12	246(75%)	5.52±0.11	2.85±0.08	61(61%)	7.20±0.18	4.28±0.14
9.5-10.0	236(65%)	5.86±0.10	3.04±0.07	898(60%)	6.69±0.05	3.64±0.04	392(46%)	8.71±0.06	5.74±0.05
10.0-10.5	122(39%)	7.92±0.10	5.19±0.08	936(43%)	8.28±0.04	5.34±0.03	392(32%)	9.40±0.04	6.64±0.04
10.5-11.0	23(25%)	8.90±0.19	6.17±0.16	194(29%)	9.15±0.06	6.28±0.05	91(24%)	9.67±0.06	7.03±0.07

Table 5.1: **Median assembly times.** Assembly time of 50% (T_{50}) and 70% (T_{70}) of the stellar mass for all the SFH types (a), galaxies with ST-SFH (b), and LT-SFH (c), in voids, filaments & walls, and clusters. The used samples take into account the selection criteria applied by the quality control analysis (see Section 4.5) and are based on the same stellar mass distributions inside every stellar mass bin (see Section 2.2.3). The error represent the s.e.m. (1σ). The number of galaxies (n) in each environment and stellar mass bin is shown together with the fraction (%) of each SFH type inside every stellar mass bin and environment. These are the values represented in Figure 5.7.

cluster galaxies, more significantly at low stellar masses than at high stellar masses. This might indicate that low-mass galaxies with ST-SFHs were formed at early times as their massive counterparts but have been later affected by the large-scale environmental density, slowing down their SFH. However, at very low stellar masses the number of galaxies (8, 24, and 9 galaxies) is less statistically significant than at higher stellar masses. High-mass galaxies with ST-SFHs have been less affected by their large-scale environment. This might be due to early mergers (even in voids, whose galaxies are not necessarily isolated, as they can be found in groups and in mergers Szomoru et al. 1996; Kreckel et al. 2012; Beygu et al. 2013), or the effect of more massive dark matter halos. Moreover, the fraction of ST-SFH low-mass galaxies (see Table 5.1) is much lower than the fraction of ST-SFH high-mass galaxies, which suggests that galaxies that were assembled quickly at the very beginning of the Universe (ST-SFH) are more likely to be massive galaxies now, to have gathered mass by consecutive mergers, to have more massive dark matter halos, to run out of gas, and to quench.

Galaxies with LT-SFHs have assembled their stellar mass later than those with ST-SFHs by 1.09 to 5.88 Gyr depending on the large-scale environment, assembly time, and stellar mass. This delay might have been enough for the LT-SFH to be affected by the large-scale environment since very early, in contrast with ST-SFH. We find in Figure 5.7 (c and f) that void galaxies with LT-SFHs evolve slower than galaxies in clusters at any given stellar mass, and slightly slower than galaxies in filaments & walls at intermediate stellar masses. The evolution of cluster galaxies with LT-SFH are accelerated, at any given stellar mass, by the higher density and higher probability of undergoing interactions in their large-scale environment compared to galaxies in voids, and filament & walls. In the same way, galaxies in filaments & walls evolve faster than galaxies in voids, indicating that evolution at later times is influenced by the large-scale structure, more significantly at intermediate stellar masses than at high and low stellar masses. At high stellar masses galaxies might have been more affected by local interactions or their massive dark matter halos than by the large-scale environments. Low-mass galaxies might have been captured as satellites of more massive galaxies, being more affected by local processes and by the central galaxies of their system than by their large-scale environment. Additionally, the lack of assembly time differences at low stellar masses may be understood within the Halo Occupation Distribution (HOD)

paradigm.

According to the HOD paradigm, galaxies in voids have higher halo mass ($\sim$ 10 %, Alfaro et al. 2020) than in denser environments for a given stellar mass. This, together with the lower probability of finding high-mass galaxies in voids, makes low-mass galaxies in voids more likely to be the central objects of a system. However, low-mass galaxies in voids, which would have presumably evolved slower than galaxies in filaments & walls due to their large-scale environment, might have compensated for these SFH differences by accelerating their star formation due to their higher halo masses.

We observe differences in the evolution of galaxies comparing their SFHs for different large-scale environments, SFH types, and stellar masses. Although the mechanics that generate these differences are not clear yet, we can identify several processes that might have triggered these SFH differences between galaxies in different large-scale environments. Differences in the halo-to-stellar mass ratio, the AGNs activity, and the gas accretion between the three large-scale environments might be some of the reasons why the SFHs in void galaxies are, on average, slower than in filaments & walls, and much slower than in clusters.

Previous cosmological simulation analysis (Artale et al. 2018; Alfaro et al. 2020; Habouzit et al. 2020; Rosas-Guevara et al. 2022) find that the halo-to-stellar mass ratio is higher in void galaxies compared to galaxies in denser large-scale environments, suggesting that galaxies in voids evolve slower than in filaments, walls, and clusters. Regarding the effect of AGNs, some observational studies found statistical evidences for a larger fraction of AGNs (Constantin et al. 2008; Ceccarelli et al. 2022), and massive BHs (Ceccarelli et al. 2022) in voids. However, there is no consensus on the effect of the large-scale structure over the nuclear activity in galaxies yet, as Argudo-Fernández et al. (2018) found the opposite result for quenched isolated galaxies, and other studies did not find significant differences in the fraction of AGNs (Amiri et al. 2019, observation) or in the BH-to-galaxy mass ratio (Habouzit et al. 2020, simulation) between different large-scale environments. There is no agreement on how the large-scale environment affects the nuclear activity of the galaxies, and it is controversial to consider AGNs as a possible mechanism that triggered the SFH differences that we find.

A simulation analysis (Kereš et al. 2005) found that there are mainly two modes of gas accretion in galaxies. In the cold accretion mode, the gas flows along the filaments into the galaxy. It dominates in low den-

sity large-scale environments, low stellar mass galaxies, and at high redshifts. In the hot accretion mode, the virialised gas around the galaxy falls into it while it cools down. It dominates in cluster large-scale environments, massive galaxies, and at low redshifts. This suggests that the gas accretion has been different throughout the SFH between galaxies in voids and galaxies in denser large-scale environments, and this might have introduced current gas content differences between them. Some other observational studies (Szomoru et al. 1996; Florez et al. 2021) did not find any atomic gas mass differences between voids and galaxies in denser large-scale environments but others (Kreckel et al. 2012; Domínguez-Gómez et al. 2022; Rosas-Guevara et al. 2022) found a tentative lack of atomic gas in void galaxies at stellar masses above $10^{9.5}$ $M_{\odot}$, the same range where we find the LT-SFH differences. However, a lack of atomic gas in galaxies does not necessarily imply a lack of molecular gas (Kenney & Young 1986; Sage et al. 1997; Das et al. 2015; Cortese et al. 2016; Grossi et al. 2016; Domínguez-Gómez et al. 2022), from which the stars are formed.

5.4 Conclusions

In this study we analyse the optical spectra of thousands of galaxies in the cosmic voids, filaments & walls, and clusters and derive their SFHs. We find that:

1. Void galaxies, on average, assemble their stellar mass slower than galaxies in filaments & walls, and much slower than galaxies in clusters.

2. There are two types of SFHs: ST-SFH and LT-SFH. Both of them populate the three large-scale environments with different probabilities.

3. Galaxies with ST-SFHs are more common in clusters. At early times, they evolve at a similar rate, largely independent of their large-scale environment or stellar mass. However, they are later affected by their large-scale environment, more significantly at low stellar masses than at high stellar masses, slowing down the evolution of void galaxies compared to filaments & walls and much more compared to clusters.

4. Galaxies with LT-SFHs are more common in voids. They evolve slower at low stellar masses than at higher stellar masses and, by definition, they evolve slower than galaxies with ST-SFHs at any given stellar mass. Cluster galaxies with LT-SFH evolve faster than galaxies in voids, and filaments & walls, at any given stellar mass. Finally, although low-mass and very high-mass galaxies with LT-SFHs, on average, evolve at the same rate in voids and filaments & walls, void galaxies, on average, assemble their stellar mass slightly slower than galaxies in filaments & walls at intermediate stellar masses.

What internal or external mechanisms are at play for low-mass and very high-mass galaxies that cancel large-scale environmental effects? What makes intermediate and high-mass galaxies in voids evolve clearly different to any other galaxy along their whole history? Here we give new observational constraints in terms of assembly time of galaxies in different large-scale environments as well as pose new questions to be answered by the numerical simulations in our quest of a better understanding of galaxy evolution.

Chapter 6

Stellar metallicities

Contents

In this chapter we present the first comparison of the stellar mass-metallicity relation ($MZ_\star R$) between galaxies in voids, filaments, walls, and clusters with different SFH types, morphologies, and colours, for stellar masses from $10^{8.0}$ to $10^{11.5}$ $M_\odot$ and redshift $0.01 < z < 0.05$. We apply non-parametric full spectral fitting techniques (pPXF and STECKMAP, see Section 4 for a complete description of the spectral analysis) to 10807 spectra of galaxies from the SDSS-DR7 (987 in voids, 6463 in filaments and walls, and 3357 in clusters, see Section 2.2 for a more detailed description of the sample selection) and derive their mass-weighted average stellar metallicity ($[M/H]_M$). We aim to better understand how the large-scale structure affects galaxy evolution by studying the stellar mass-metallicity relation of thousands of galaxies, which allows us to make a statistically sound comparison between galaxies in voids, filaments, walls, and clusters.

The stellar populations recovered by STECKMAP are characterised by their stellar mass, stellar age, and the metallicity of the gas from which the stars formed, providing an estimation of the type of stars that currently form a galaxy. In the E-MILES models, the metallicity is defined as the fraction of metals (Z) normalised to the solar value ($Z_\odot = 0.0198$) as $[M/H] = \log_{10}(Z/Z_\odot)$. We can then derive the mass-weighted average stellar metallicity of the galaxy as:

$$[M/H]_M = \frac{\sum M_\star [M/H]_\star}{\sum M_\star} \tag{6.1}$$

where $M_\star$ and $[M/H]_\star$ are the mass and metallicity of the stellar populations that form the galaxy, respectively, which are obtained through spectral fit. The BaSTI theoretical isochrones that are used by the E-MILES models cover the metallicity range $-2.27 \leq [M/H] \leq 0.4$. We find that the stellar metallicity values of some galaxies saturate at the upper boundary of the stellar models. The central parts of galaxies can be metal-rich, $0.30 < [M/H] < 0.47$ (González Delgado et al. 2015, see Section B therein), with values higher than the stellar models, leading to a saturation effect. In this work we derive the stellar metallicities of the centre (3 arcsec diameter) of nearby galaxies ($0.01 < z < 0.05$) using the integrated spectrum in the innermost regions of the galaxies (aperture from 0.3 to 1.6 kpc). For some galaxies, the stars in these inner regions are very metal rich and their average stellar metallicity reach the limit of the stellar models.

This effect is also found by Gallazzi et al. (2005), see Figure 8 therein. However, they obtain stellar metallicity average values that

are lower than ours because they analyse a sample of galaxies with a wider redshift range ($0.005 < z < 0.22$) and the SDSS spectra that they use are integrated over more external regions of the galaxies, where the stars are metal-poorer than in the centre. In our results, the fraction of galaxies with this saturation issue in each stellar mass bin, SFH type, and environment is lower than 10%, except for filament & wall and cluster galaxies with ST-SFHs at high stellar masses ($M_\star > 10^{10.5}$ $M_\odot$), for which the fraction of saturated galaxies is around 20%. There is no saturation for void galaxies. The saturation effect is conservative as it reduces the average stellar metallicity of filament & wall and cluster massive galaxies but does not affect void galaxies, diluting the stellar metallicity differences that we find at high stellar masses.

The metallicity of a galaxy is strongly influenced by its SFH (Tantalo & Chiosi 2002). A high star formation rate quickly enriches the ISM and the stars that will form from it. Therefore, the effect of the SFH has to be considered in our analysis of the stellar metallicities. We analysed (in Chapter 5) the SFHs as the fraction of stellar mass that was formed at a given look-back time. We found that there are two main SFH types (ST-SFH and LT-SFH). For a given SFH type, galaxies in voids, on average, formed their stars slower than in filaments & walls at intermediate stellar masses, and much slower than in clusters at any given stellar mass. The SFH differences between galaxies in the three large-scale environments might have affected the stellar metallicities diversely in voids, filaments & walls, and clusters. Therefore, in this chapter we analyse the effect of the large-scale environment on the stellar metallicities of the galaxies for different SFH types.

It might be intuitive to associate the ST-SFH type with red elliptical galaxies, and the LT-SFH type with blue spiral galaxies. However, we show in Section 5.1 that the SFH type of a galaxy clearly correlates neither with its colour nor its morphology (see figures 5.4 and 5.5). Therefore, we also analyse the $MZ_\star R$ for different morphologies and colours. We use the g and r dereddened magnitudes from SDSS to define the colour of the galaxies as $g - r$, and the T-type parameter from Domínguez Sánchez et al. (2018) to characterise the morphology of the SDSS galaxies. We consider that galaxies with T-type < 0 are elliptical and galaxies with T-type > 0 are spiral (Domínguez Sánchez et al. 2018), and here we define galaxies with $g - r \leq 0.7$ mag as blue, and $g - r > 0.7$ mag as red. Note that the SDSS g and r magnitudes are integrated over the entire galaxy, but the stellar populations are recovered from the very centre of the galaxy, where the stars are redder

than the average colour $g - r$ of the whole galaxy.

This chapter is based on Domínguez-Gómez et al. (submitted) and is organised in seven sections and three appendices. In Section 6.1 we present the average stellar metallicity distribution of galaxies in different large-scale environments and stellar mass bins. In the following sections, we compare the $MZ_\star R$ between galaxies in different large-scale environments (Section 6.2) for different SFH types (Section 6.3), morphology (Section 6.4) and colours (Section 6.5). In Section 6.6 we discuss our results and compare with previous studies. In Section 6.7 we summarise our conclusions. In Appendix B.1 we extend our study to galaxy samples with the same stellar mass distribution. In Appendix B.2 we show similar results for the luminosity-weighted metallicities. In Appendix B.3 we present the tables with our $MZ_\star R$ results.

6.1 Average stellar metallicity distribution

We show in Figure 6.1 the normalised distribution of $[M/H]_M$ for galaxies in voids (blue dashed line), filaments & walls (green dot-dashed line), and clusters (red solid line) in three stellar mass bins. There are some small peaks at $[M/H]_M \sim 0.4$, which are produced by the saturation of our results at the metallicity upper limit of the E-MILES SSPs. The distributions exhibit a sharp cut-off at higher values (around 0.5) due to the broadening effect caused by the metallicity errors. We find that the stellar metallicity distribution is similar for galaxies in voids and galaxies in filaments & walls. However, cluster galaxies are distributed at much higher metallicities. These differences might be affected by their different stellar mass distributions and star formation history types. Void galaxies are on average less massive (see Section 2.2.2) and form their stars slower than galaxies in denser environments (see Chapter 5). We then carry out comparisons for different stellar mass bins, SFH types, morphologies, and colours. In addition, in Appendix B.1 we repeat the same analysis for sub-samples with the same stellar mass distribution, where we find similar results.

6.2 Stellar mass effect

We show in Figure 6.2 the $MZ_\star R$ for all the galaxies regardless of their SFH type (left column) in voids (first row), filaments & walls (second

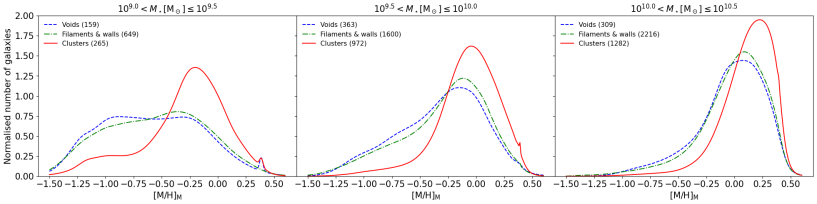

Figure 6.1: Mass-weighted average stellar metallicity ($[M/H]_M$) distribution of our samples of galaxies in voids (blue dashed line), filaments & walls (green dot-dashed line), and clusters (red solid line) for three stellar mass bins as labelled. The number of galaxies in each sample is showed in the legend. The peaks at ~ 0.4 is due to the metallicity limit of the E-MILES stellar models. The distribution sharply ends at higher values (~ 0.5) than this limit due to the widening by the errors.

row), and clusters (third row). We define stellar mass bins of 0.5 dex from $10^{8.0}$ to $10^{11.5}$ $M_\odot$, and obtain the $MZ_\star R$ (thick lines) as the 50^{th} percentile of the distribution of galaxies inside each stellar mass bin. We estimate the error of the $MZ_\star R$ (shaded areas) as the s.e.m. inside each stellar mass bin. In addition, we calculate the 16^{th} and the 84^{th} percentiles (thin lines) to visualise the dispersion of values. We compare the $MZ_\star R$ between the three environments in the fourth row, together with the $MZ_\star R$ from Gallazzi et al. (2005) as a reference. In the fifth row we show the $MZ_\star R$ differences between galaxies in voids and filaments & walls, and also between galaxies in voids and clusters. In Table B.1 we report the 50^{th} (together with the s.e.m.), 16^{th} and the 84^{th} percentiles of the $MZ_\star R$ for the different large-scale environments and SFH types. We report in Table B.2 the differences of the 50^{th} percentile between voids and filaments & walls, and also between voids and clusters.

In the left column panels of Figure 6.2 we find that galaxies in voids have on average slightly lower stellar metallicities than galaxies in filaments & walls, and much lower than galaxies in clusters for any given stellar mass regardless of their star formation history type. These differences are more significant at low stellar masses than at high stellar masses, at which the difference might have been diluted by the effect of the metallicity saturation (see introductory section in this chapter). The stellar metallicity in void galaxies is slightly lower than in filaments & and walls by 0.108 ± 0.019 ($5.7\ \sigma$) at low stellar masses ($\sim 10^{9.25}$ $M_\odot$) to 0.031 ± 0.009 ($3.4\ \sigma$) at intermediate stellar masses ($\sim 10^{10.25}$ $M_\odot$). Void galaxies have lower stellar metallicities than cluster galaxies by 0.40 ± 0.02 ($20.0\ \sigma$) at low stellar masses ($\sim 10^{9.25}$ $M_\odot$) to 0.084 ± 0.013 ($6.5\ \sigma$) at high stellar masses ($\sim 10^{10.75}$ $M_\odot$). Our re-

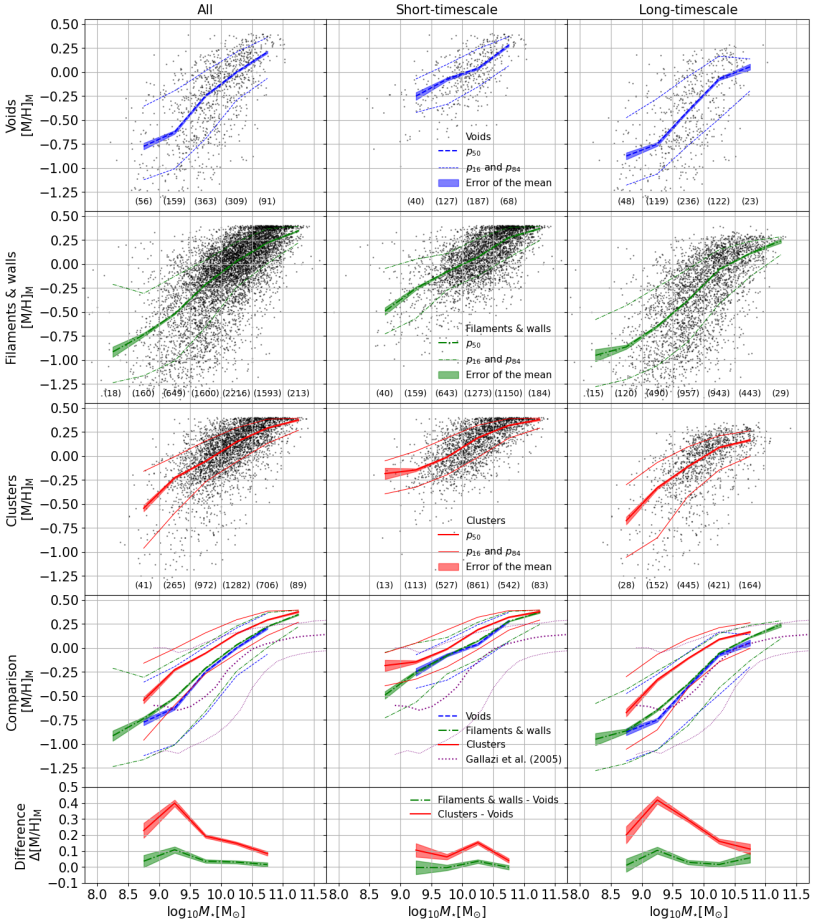

Figure 6.2: Stellar mass-metallicity relation ($MZ_\star R$). Mass-weighted average stellar metallicity ($[M/H]_M$) as a function of stellar mass for the galaxies regardless of their SFH type (left column), galaxies with short-timescale star formation histories (ST-SFH, centre column), and galaxies with long-timescale star formation histories (LT-SFH, right column); in voids (first row), filaments & walls (second row), and clusters (third row). The $MZ_\star R$ (blue dashed lines for voids, green dot-dashed lines for filaments & walls, and red solid lines for clusters) is derived as the 50^{th} percentile (thick lines) inside each stellar mass bin of 0.5 dex. The number of galaxies inside each stellar mass bin is shown in brackets at the bottom of the panels. The shade areas represent the standard error of the mean (s.e.m.), and the 16^{th} and 84^{th} percentiles (thin lines) the dispersion of the $MZ_\star R$. The fourth row shows a comparison of the $MZ_\star R$ between galaxies voids, filaments & walls and clusters, together with the $MZ_\star R$ from Gallazzi et al. (2005) as a reference. In the fifth row we show the differences of the $MZ_\star R$ (lines), together with the error of the difference (shaded areas). See values reported in tables B.1 and B.2.

sults at very low ($\sim 10^{8.25}$ $M_\odot$) or very high ($\sim 10^{11.25}$ $M_\odot$) stellar masses are not statistically significant due to the low number of galaxies in voids (4) and clusters (2). In our conclusions we only consider stellar mass bins with more than 10 galaxies.

The $MZ_\star R$ derived by Gallazzi et al. (2005) is in general below what we obtain. They derived the stellar metallicity from the SDSS-DR2 spectra in the centre (3 arcsesc aperture) of 175128 galaxies. They use the same type of spectral data as we do in this analysis. However, the redshift range of their galaxy sample ($0.005 < z < 0.22$) is much wider than ours ($0.01 < z < 0.05$). On average, the apparent size of their galaxies is smaller than ours. Therefore, the spectrum of their galaxies is integrated over more external regions, where the stellar populations are younger an metal-poorer. The spectra of our galaxies are integrated in smaller regions from the centre, where the stars are older and metal-richer. At low stellar masses ($< 10^{9.5}$ $M_\odot$) our $MZ_\star R$ is similar to theirs. This might be due to the completeness limit of the sample as the number of low-mass galaxies decreases with redshift. Therefore, the low-mass galaxies in their sample might be at similar redshifts as low-mass galaxies in our samples, and the aperture effect explained above is negligible.

6.3 Star formation history effect

In Figure 6.2 (centre and right columns panels) we show how the SFH type (ST-SFH and LT-SFH, respectively) of the galaxies affects the $MZ_\star R$ and compare galaxies in voids, filaments & walls, and clusters. We find that ST-SFH galaxies have higher stellar metallicities than LT-SFH galaxies for a given stellar mass in the three environments. This, together with the fact that it is more likely for galaxies in voids to have a LT-SFH ($51.7 \pm 0.9\%$) than for galaxies in filaments & walls ($44.5 \pm 0.3\%$), and galaxies in cluster ($36.1 \pm 0.5\%$), can explain that void galaxies have on average slightly lower metallicities than galaxies in filaments & walls, and much lower than galaxies in clusters when we compare all the galaxies regardless of their SFH type in Figure 6.2 (left column panels).

We now go in more detail and analyse the stellar metallicity differences for two different SFH types. Galaxies with ST-SFHs have similar stellar metallicities (within the errors) in voids and filaments & walls, except for intermediate stellar masses ($\sim 10^{10.25}$ $M_\odot$) where

void galaxies have slightly lower stellar metallicities, by 0.035 ± 0.011 ($3.2\ \sigma$). Galaxies with ST-SFHs in voids have lower stellar metallicities than in clusters by 0.152 ± 0.011 ($13.8\ \sigma$) at $M_\star \sim 10^{10.25}$ $M_\odot$ or by 0.063 ± 0.017 ($3.7\ \sigma$) at $M_\star \sim 10^{9.75}$ $M_\odot$. Galaxies with LT-SFHs have similar stellar metallicities (within the errors) in voids and filaments & walls, except for low stellar masses ($\sim 10^{9.25}$ $M_\odot$) where void galaxies have slightly lower stellar metallicities, by 0.104 ± 0.021 ($5.0\ \sigma$). Galaxies with LT-SFHs in voids have lower stellar metallicities than in clusters. These differences are more significant at low stellar masses ($\sim 10^{9.25}$ $M_\odot$), by 0.419 ± 0.024 ($17.5\ \sigma$), than at high stellar masses ($\sim 10^{10.75}$ $M_\odot$), by 0.11 ± 0.03 ($3.7\ \sigma$). The differences that we find for galaxies with LT-SFHs are similar to what we find for all the galaxies regardless of their SFH type in Figure 6.2 (left column panels). However, the differences that we find for galaxies with ST-SFHs are less significant. This means that the stellar metallicity differences that we find between galaxies in different environments, regardless of their SFH type, are mainly due to the galaxies with LT-SFHs, while the contribution of galaxies with ST-SFH is not significant.

6.4 Morphology effect

In Figure 6.3 (left and right columns panels) we show the $MZ_\star R$ for different morphological types (elliptical and spiral, respectively) and compare galaxies in voids, filaments & walls, and clusters. We report in tables B.3 and B.4 the percentiles (50^{th} with the s.e.m., 16^{th}, and 84^{th}) of the $MZ_\star R$, and the 50^{th} percentile differences between galaxies located in the three large-scale environments. We find that elliptical galaxies have higher stellar metallicities than spiral galaxies in all environments and at all stellar masses. However, galaxies have similar stellar metallicities (within the errors) in voids and filaments & walls for the two morphological types and for any given stellar mass, except for intermediate stellar masses ($\sim 10^{9.75}$ $M_\odot$) where void galaxies have slightly lower stellar metallicities, by 0.057 ± 0.017 ($3.4\ \sigma$) for elliptical galaxies, and by 0.071 ± 0.016 ($4.4\ \sigma$) for spiral galaxies. Void galaxies have lower stellar metallicities than cluster galaxies in the two morphological types. These differences are more significant at low stellar masses ($\sim 10^{9.25}$ $M_\odot$), by 0.26 ± 0.04 ($6.5\ \sigma$) for elliptical galaxies, and by 0.27 ± 0.03 ($9.0\ \sigma$) for spiral galaxies; than at high stellar masses ($\sim 10^{10.25}$ $M_\odot$), by 0.075 ± 0.012 ($6.2\ \sigma$) for elliptical galaxies, and by

0.077 ± 0.017 (4.5 σ) for spiral galaxies.

The differences that we find for elliptical galaxies, and for spiral galaxies, are similar to what we find for galaxies with LT-SFHs in Figure 6.2 (right column panels). This occurs more clearly for spiral than for elliptical galaxies. The stellar metallicity differences that we find between the three environments for spiral galaxies are similar to what we find for LT-SFHs due to the fraction of spiral galaxies with LT-SFHs (62.7% in voids, 56.5% in filaments & walls, 52.6% in clusters, see Figure 5.4). A similar effect happens for elliptical galaxies, which also have similar stellar metallicity differences between environments as LT-SFH galaxies, but much more diluted by the higher fraction of elliptical galaxies with ST-SFHs (56.8% in voids, 65.8% in filaments & walls, 70.9% in clusters).

6.5 Colour effect

In Figure 6.4 we show the relation between colour and the $MZ_{\star}R$, and compare galaxies in voids, filaments & walls, and clusters. The $MZ_{\star}R$ and their differences between environments are reported in table B.5 and B.6. We find that red galaxies (left panels in Figure 6.4) have higher stellar metallicities than blue galaxies (right panels) for a given stellar mass. However, galaxies have similar stellar metallicities (within the errors) in voids and filaments & walls for the two colours and for any given stellar mass, except for low stellar masses ($\sim 10^{9.25}$ $M_{\odot}$) where blue galaxies in voids have slightly lower stellar metallicities than blue galaxies in filaments & walls by 0.091 ± 0.020 (4.5 σ). Red galaxies in voids have slightly lower stellar metallicities than red galaxies in clusters by 0.103 ± 0.016 (6.4 σ) at intermediate stellar masses ($\sim 10^{9.75}$ $M_{\odot}$) to 0.066 ± 0.013 (5.1 σ) at high stellar masses ($\sim 10^{10.75}$ $M_{\odot}$). Blue galaxies in voids have lower stellar metallicities than blue galaxies in clusters by 0.315 ± 0.023 (13.7 σ) at low stellar masses ($\sim 10^{9.25}$ $M_{\odot}$) to 0.150 ± 0.015 (10.0 σ) at intermediate stellar masses ($\sim 10^{9.75}$ $M_{\odot}$).

The stellar metallicity differences of blue galaxies (see right column panels in Figure 6.4) look very similar to what we find for galaxies with LT-SFH (right column panels in Figure 6.2) but in a narrower stellar mass range. Blue galaxies in voids have lower stellar metallicities than in clusters for stellar masses between $10^{8.75}$ $M_{\odot}$ and $10^{9.75}$ $M_{\odot}$. For LT-SFHs galaxies, these differences between voids and clusters remain up to $10^{10.25}$ $M_{\odot}$. On the contrary, the stellar metallicity differences

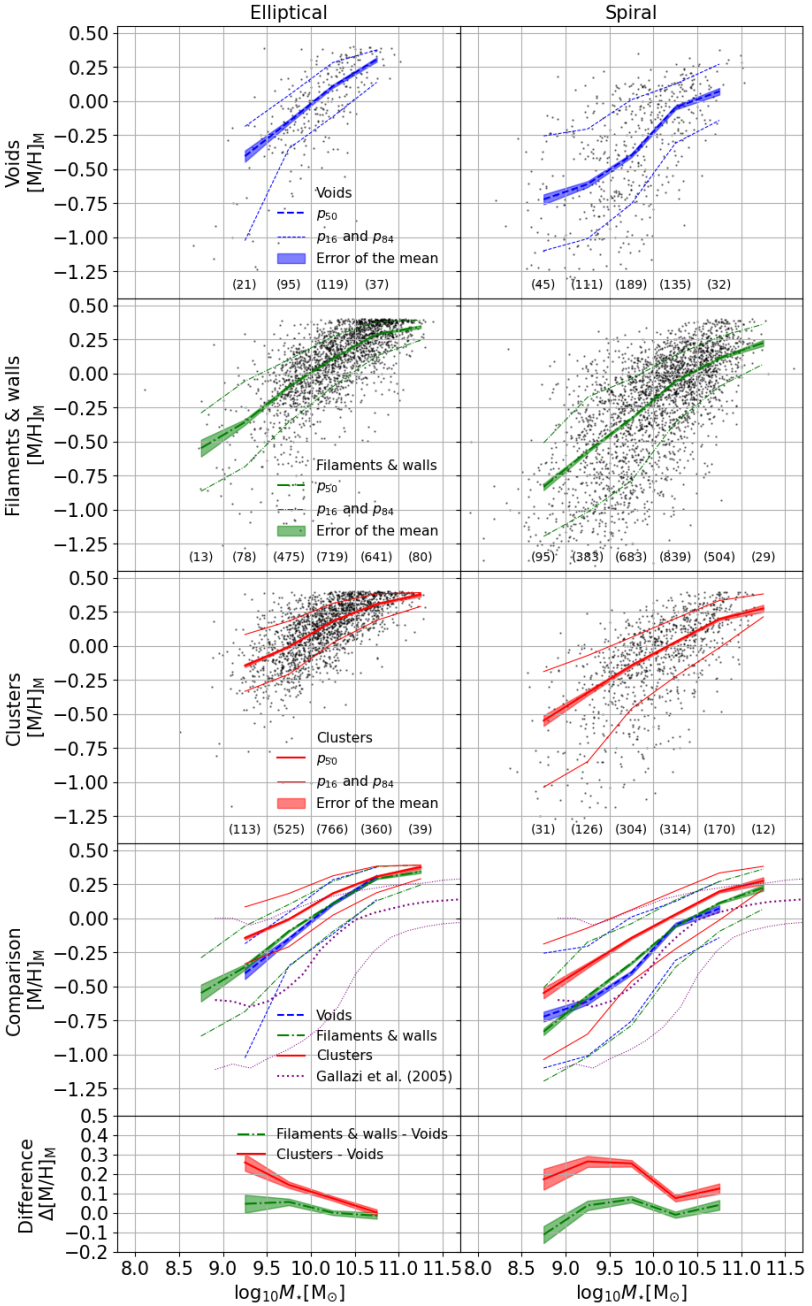

Figure 6.3: Same as Figure 6.2 but for elliptical (left column) and spiral galaxies (right column). See values reported in tables B.3 and B.4.

that we find for red galaxies are less significant, similar to what we find for ST-SFH. This happens because a high fraction of red galaxies have a ST-SFH and a high fraction of blue galaxies have a LT-SFH ($\sim$ 65 − 70%, see Figure 5.4).

Comparing blue galaxies between different large-scale environments is not straightforward as the colour distribution is not the same (similar challenge applies to red galaxies). Introducing an alternative classification of blue and red galaxies may change our results. However, we show in Figure B.1.4 the same as in Figure 6.4 but with the colour classification criterion at 0.6 instead of 0.7, which shows that the stellar metallicity differences that we find for the colour cut at 0.6 is very similar to what we find for the colour cut at 0.7.

6.6 Discussion

6.6.1 Stellar mass-metallicity relation

We see that the $MZ_{\star}R$ correlates with the large-scale environment, SFH type, morphology, and colour of the galaxies. The stellar metallicity of galaxies in voids is slightly lower than galaxies in filaments & walls at determined stellar mass bins, and much lower that galaxies in clusters at any given stellar mass. There are many works that study the $MZ_{g}R$ of galaxies and some of them even compare between different local (Deng 2011; Pasquali et al. 2012; Pilyugin et al. 2017), and large-scale environments (Wegner & Grogin 2008; Pustilnik et al. 2011; Kreckel et al. 2015; Wegner et al. 2019) but there is no consensus about the gas metallicity properties in void galaxies. However, only a few works study how the local environment affects the $MZ_{\star}R$, and none of them study how it is affected by the large-scale structures of the Universe. Scholz-Díaz et al. (2022, 2023) studied the stellar populations of groups of galaxies, and found that, for a given stellar mass, the stellar age and metallicity of central galaxies decreases with the halo mass. This means that the lower stellar metallicities that we find for void galaxies might be due to their higher halo-to-stellar mass ratios compared to denser environments (Artale et al. 2018; Alfaro et al. 2020; Habouzit et al. 2020; Rosas-Guevara et al. 2022). Additionally, Pasquali et al. (2010) and Gallazzi et al. (2021) found that the stellar metallicity of galaxies decreases as we move towards lower density galaxy groups and clusters. This is in line with our results, as we find that the stellar metallicity of galaxies located in large-scale environments with the lowest density (i.e.

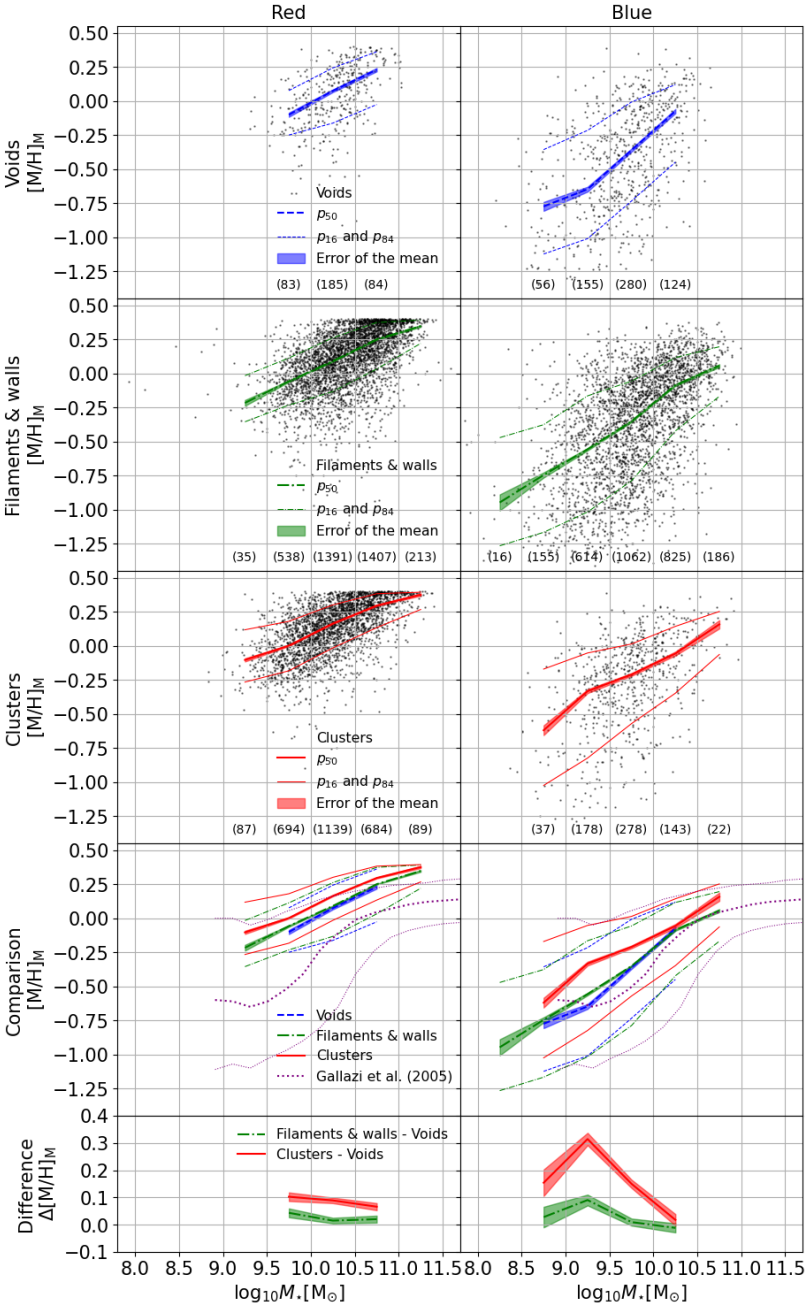

Figure 6.4: Same as Figure 6.2 but for red (left column) and blue galaxies (right column). See values reported in tables B.5 and B.6.

voids and filaments & walls) are, on average, lower than for galaxies located in clusters. However, they did not compare with void galaxies.

Gallazzi et al. (2021) found that the stellar metallicity of recent clusters/groups infallers (i.e. those galaxies that passed the virial radius of the host halo $<$ 2.5 Gyr ago) is lower than that of those that have been exposed to the environment of clusters/groups for a longer time ($>$ 2.5 Gyr). Recent infallers keep forming stars (although with lower rates) for $\sim$ 2 Gyr after their infall (Rhee et al. 2020, Figure 7 therein). The typical timescale of ram pressure stripping in clusters as massive as Virgo is $<$ 1 Gyr, and for tidal interactions is $\sim$ 2 Gyr (Boselli & Gavazzi 2006). This means that, for about 2 Gyr after falling into the cluster, the galaxies (recent infaller) still act as if they are in the previous host environment (i.e. voids or filaments & walls) with little changes in the SFR. The results of Gallazzi et al. (2021) would be in agreement with ours as they found that recent infallers (i.e. with void and filament & walls galaxy properties) have lower stellar metallicities compared to ancient infallers (i.e. with cluster galaxy properties).

It is well known that the metallicity of a galaxy is significantly determined by its SFH (Tantalo & Chiosi 2002), and this is reflected in our results. The stellar metallicity differences that we find for galaxies in different large-scale environments are much more significant for LT-SFH than for ST-SFH. ST-SFH galaxies formed a high fraction ($\sim$ 30%) of their stellar mass very early (more than 12.5 Gyr ago, see Chapter 5) enriching their ISM very quickly for the next generation of stars to be formed. Furthermore, they assembled 50% of their stellar mass at a similar time ($T_{50} \sim$ 11 Gyr ago) in voids, filaments & walls, and clusters. This suggests that in the early Universe there was less contrast between the large-scale environments, which did not affect the evolution of the ST-SFH galaxies in the beginning but later, i.e. when they assembled 70% of their stellar mass. Void galaxies formed 70% of their stellar mass later than in filaments & walls (by $\sim$ 1 Gyr) and much later than in clusters (by $\sim$ 2 Gyr), more significantly at low ($10^{9.0} - 10^{9.5}$ M$_\odot$) than at high stellar masses ($10^{10.0} - 10^{10.5}$ M$_\odot$).

LT-SFH galaxies have had a more steady SFHs, enriching their ISM slower, and possibly diluting their metallicity by metal-poor gas accretion. Moreover, LT-SFH galaxies have been affected by their large-scale environments since very early, assembling their stellar mass later in voids than in filaments & walls (at intermediate stellar masses, $10^{9.5} - 10^{10.0}$ M$_\odot$, by $\sim$ 1 Gyr), and much later than in clusters (at any given stellar mass by $\sim$ 2 Gyr). This indicates that galaxies that had

similar SFHs in the beginning (i.e. ST-SFH galaxies, with similar T_{50} in the three environments) would have similar stellar metallicities now, even if their SFH differ later (different T_{70} in the three environments). On the contrary, galaxies with different SFHs in the beginning (i.e. LT-SFH galaxies, with different T_{50} in the three environments) would have different stellar metallicities now. Therefore, the mass-weighted stellar metallicity of a galaxy is mostly determined by its initial SFH period (old stars). We confirm this in Figure 6.5, where we show a direct correlation (blue arrow) in the mass-weighted stellar age-metallicity distribution. We derive the mass-weighted stellar age following the same recipe as for metallicity given in Equation 6.1.

Gallazzi et al. (2005) found an effect of the age-metallicity degeneracy as an anti-correlation for the oldest galaxies in the stellar age-metallicity distribution for luminosity-weighted ages and metallicities (see their figures 11 and 12). We do not find this anti-correlation for the mass-weighted average in Figure 6.5. However, the comparison between luminosity-weighted and mass-weighted averages is not straightforward. We derive in Appendix B.2 the $MZ_{\star}R$ applying the luminosity-weighted average, where we find similar results to what we find in this chapter for the mass-weighted average. We show in Figure 6.6 the luminosity-weighted stellar age-metallicity distribution for our sample of galaxies and we recover a similar anti-correlation (red arrow) for the oldest galaxies. However, we keep having a direct correlation (blue arrow) for young galaxies. Void galaxies have assembled their mass on average slower than galaxies in denser environments (see Section 5), and their stellar populations are consequently younger than in filaments & walls, and clusters. This is in agreement with the lower stellar metallicities that we find for void galaxies.

We also show that the stellar metallicity differences that we find between different large-scale environments are more significant for blue spiral galaxies than for red elliptical galaxies. Gallazzi et al. (2005) found that, for a given stellar mass, early-type galaxies have on average older and more metal rich stellar populations than late-type galaxies. Red elliptical galaxies are more likely to be gas-poor quenched massive galaxies that have suffered high star formation bursts after galaxy-galaxy interactions or mergers, quickly enriching their ISM. They also suffer from internal feedback processes such as AGNs, supernovae, and stellar winds. Blue spiral galaxies are more likely to be gas-rich star-forming galaxies with less chances to have suffered mergers in the past, preserving their metal-poor surrounding gas, and enriching their ISM

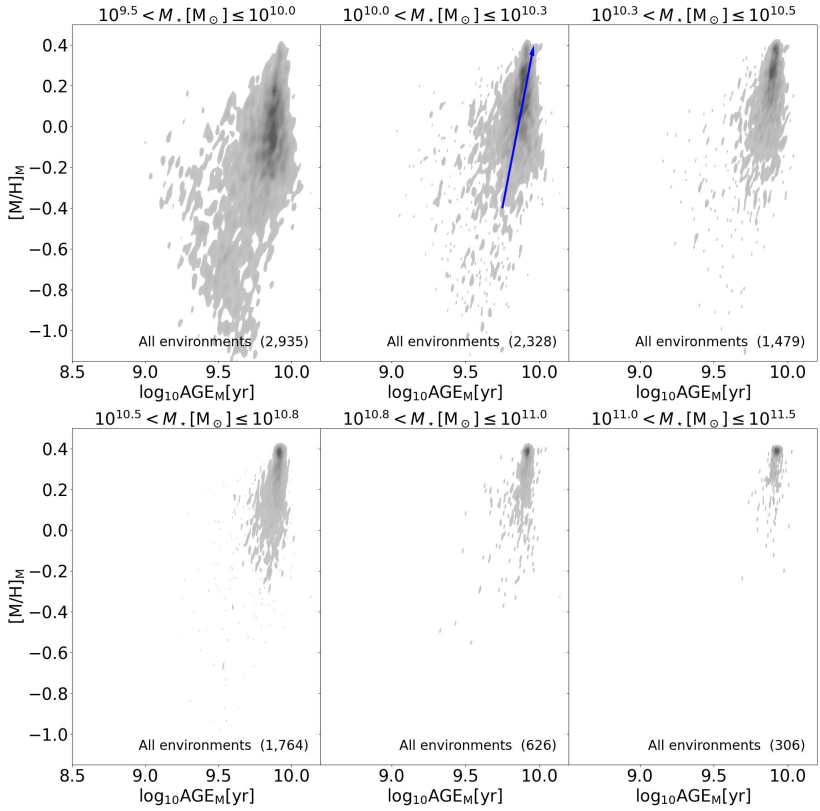

Figure 6.5: Stellar age-metallicity distribution for several stellar mass ranges as labeled. The stellar metallicities and ages of the galaxies are derived as the mass-weighted average. The blue arrows visually illustrate the age-metallicity correlation.

slower than red elliptical galaxies. Void galaxies are on average bluer and have later morphological types than in denser environments, fulfilling the expectations of finding lower stellar metallicities in void galaxies.

6.6.2 Scatter around the gas-phase mass-metallicity relation

As very little is known about the correlation between the $MZ_\star R$ and the large-scale environment we compare our results with previous studies about the gas-phase metallicity. It is not obvious to directly compare

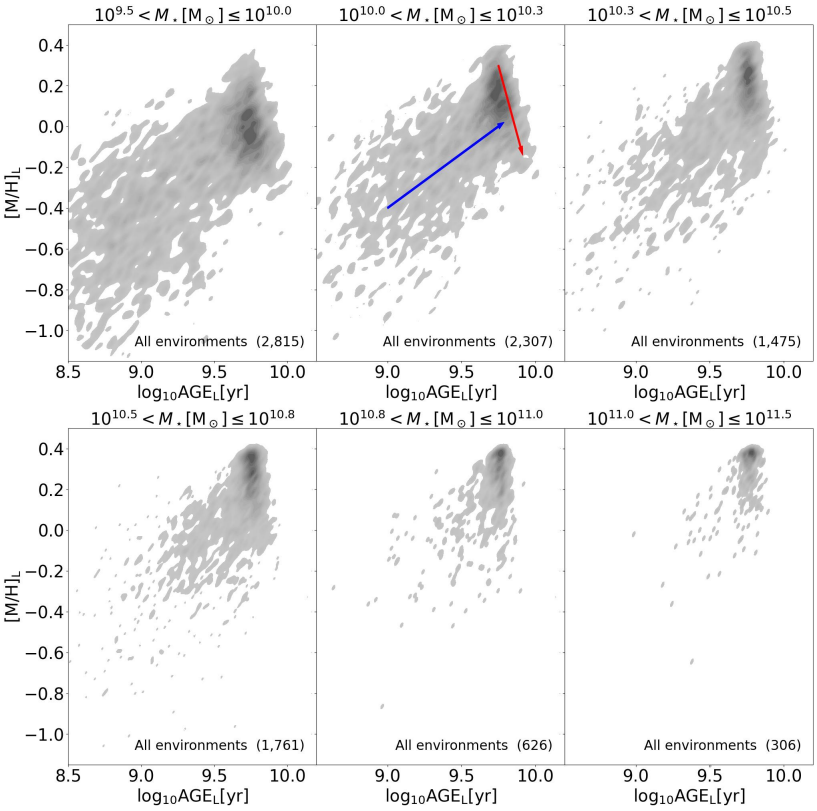

Figure 6.6: Same as Figure 6.5 but for the luminosity-weighted averages of the age and metallicity. The arrows visually illustrate the age-metallicity correlation (blue arrows) and anti-correlation (red arrow).

the MZ$_\star$R with studies focusing on the MZ$_g$R as this procedure only takes into account star-forming galaxies (with gas emission lines) but we also consider quenched galaxies (without gas emission lines). We can only refer to blue and spiral (i.e. star-forming) galaxies of our sample (right columns panels in figures 6.3 and 6.4, respectively) when comparing our MZ$_\star$R results with the MZ$_g$R. Additionally, previous studies (Gallazzi et al. 2005; Panter et al. 2008; Zahid et al. 2017) have shown that the stellar metallicity correlates with the gas-phase metallicity when considering young stellar populations or the luminosity-weighted average stellar metallicity. We show in Appendix B.2 the MZ$_\star$R applying the luminosity-weighted average, where we find similar results

to what we find in this chapter for the mass-weighted average of blue and spiral galaxies. Blue and spiral galaxies in voids have lower stellar metallicities than in filaments & walls and much lower than in clusters, and the differences are more significant at low than at high stellar mass. Thus, we assume that it is fair to compare our mass-weighted $MZ_{\star}R$ for blue spiral galaxies with the $MZ_{g}R$ results in the literature, and interpret our differences in the $MZ_{\star}R$ for different large-scale environments as a scatter around the main $MZ_{g}R$, associated with the halo mass of the galaxies, gas accretion, and gas feedback.

IllustrisTNG simulation (Torrey et al. 2019) shows that the scatter in the $MZ_{g}R$ correlates with the ISM-to-stellar mass ratio ($M_{\rm ISM}/M_{\star}$) and the SFR. High SFRs or low $M_{\rm ISM}/M_{\star}$ ratios increase the gas metallicity of star forming galaxies. That would imply that the higher stellar metallicity that we find for the blue and spiral galaxies in clusters is driven by a lower $M_{\rm ISM}/M_{\star}$ or higher SFR than in less dense environments.

An observational study (Yang et al. 2022) showed that the gas mass and the gas metallicity are anti-correlated at a given stellar mass up to $M_{\star} < 10^{10.5}$ $M_{\odot}$. Simulations (van de Voort et al. 2011) predict a correlation between the gas accretion rates and the host halo mass of the galaxy up to $M_{\rm h} < 10^{12.0}$ $M_{\odot}$. So, the more massive the halo, the higher the gas accretion and the gas fraction. This implies a decreased gas-phase metallicity, since the inflowing gas is assumed to be more metal-poor than the ISM. This would imply that the lower stellar metallicity that we find for our void galaxies is due to a higher gas mass or higher gas accretion rates driven by their more massive host halos. This scenario is supported by simulations that find that the halo-to-stellar mass ratio is higher in void galaxies compared to galaxies in denser large-scale environments (Artale et al. 2018; Alfaro et al. 2020; Habouzit et al. 2020; Rosas-Guevara et al. 2022). Another possibility is that there are two different modes of gas accretion (Kereš et al. 2005): the cold gas accretion mode dominates in void galaxies, while the hot gas accretion mode prevails in denser environments. Additionally, a previous observational study (Florez et al. 2021) found that void galaxies have higher gas mass than galaxies in denser environments, more significantly for low-mass ($M_{\star} < 10^{10.0}$ $M_{\odot}$) and early-type galaxies than for high-mass or late-type galaxies. However, other observational studies (Szomoru et al. 1996; Kreckel et al. 2012; Domínguez-Gómez et al. 2022) and simulations (Rosas-Guevara et al. 2022) did not find significant gas mass differences between galaxies in

different large-scale environments for this stellar mass regime. Very little observational evidences have been provided for gas accretion rates onto galaxies, given the considerable challenge of directly measuring it.

At higher stellar masses ($M_\star > 10^{10.5}$ $M_\odot$), Yang et al. (2022) find that the scatter of the MZ_gR correlates only very weakly with the gas mass but a stronger trend is found with AGN activity. Both EAGLE and IllustrisTNG simulations find that the scatter of the MZ_gR is no longer driven by systematic variations in gas inflow rate, but instead dominated by the impact of AGN feedback (De Rossi et al. 2017; Torrey et al. 2019; van Loon et al. 2021). Galaxies with the higher nuclear activity have the lowest metallicities. Previous observational studies (Constantin et al. 2008; Ceccarelli et al. 2022) found a larger fraction of AGNs or massive BH in voids than in denser large-scale environments. However, there is no consensus on the effect of the large-scale structure over the nuclear activity in galaxies yet, as Argudo-Fernández et al. (2018) found the opposite result for quenched isolated galaxies, and other studies did not find significant differences in the fraction of AGNs (Amiri et al. 2019, observation) or in the BH-to-galaxy mass ratio (Habouzit et al. 2020, simulation) between different large-scale environments. This would not be in disagreement with our results as we do not find significant stellar metallicity differences between galaxies in different large-scale environments at high stellar masses ($M_\star > 10^{10.5}$ $M_\odot$). However, in this stellar mass range, the stellar metallicity differences between galaxies in voids and denser large-scale environments might have been diluted by the effect of the metallicity saturation.

6.7 Conclusions

We apply a non-parametric full spectral fitting analysis to the SDSS spectra in the centre of statistically sound samples of galaxies in voids, filaments & walls, and clusters. We recover their stellar populations and study how the large-scale structures of the Universe affect the stellar mass-metallicity relation of galaxies for different SFH types, morphologies, and colours. The main conclusions are listed below:

1. Void galaxies have slightly lower stellar metallicities than galaxies in filaments & walls, more significantly at low ($10^{9.25}$ $M_\odot$ by 0.108 ± 0.019) than at high stellar masses ($10^{10.25}$ $M_\odot$ by 0.031 ± 0.009), and much lower than galaxies in clusters, also more significantly at low stellar masses ($10^{9.25}$ $M_\odot$ by 0.40 ± 0.02)

than at high stellar masses ($10^{10.75}$ $M_\odot$ by 0.084 ± 0.013). At high stellar masses ($10^{10.75}$ $M_\odot$), the differences between galaxies in voids and denser environments might have been diluted by the effect of the metallicity saturation.

2. The stellar metallicity differences between galaxies in voids and galaxies in denser environments are more significant for LT-SFH than for ST-SFH galaxies, more significant for spiral than for elliptical galaxies, and more significant for blue than for red galaxies.

3. ST-SFH galaxies in voids have slightly lower stellar metallicities than galaxies in filaments & walls at intermediate stellar masses ($10^{10.25}$ $M_\odot$, by 0.035 ± 0.011), and much lower than galaxies in clusters, more significantly at intermediate ($10^{10.25}$ $M_\odot$, by 0.152 ± 0.011) than at low ($10^{9.25}$ $M_\odot$, by 0.063 ± 0.017) stellar masses. LT-SFH galaxies in voids and filaments & walls have similar stellar metallicities, except for low stellar masses ($10^{9.25}$ $M_\odot$), where void galaxies have slightly lower stellar metallicities (by 0.104 ± 0.021). LT-SFH galaxies in voids have much lower stellar metallicities than in clusters, more significantly at low stellar masses ($10^{9.25}$ $M_\odot$, by 0.419 ± 0.024), than at high stellar masses ($10^{10.75}$ $M_\odot$, by 0.11 ± 0.03). We note again that at high stellar masses ($10^{10.75}$ $M_\odot$), the differences between ST-SFH galaxies in voids and denser environments might have been diluted by the effect of the metallicity saturation.

4. Both elliptical and spiral galaxies in voids have slightly lower stellar metallicities than in filaments & walls at intermediate stellar masses ($10^{9.75}$ $M_\odot$, by 0.057 ± 0.017 and 0.071 ± 0.016, respectively), and much lower than in clusters, more significantly at low stellar masses ($10^{9.25}$ $M_\odot$, by 0.26 ± 0.04 and 0.27 ± 0.03) than at high stellar masses ($10^{10.25}$ $M_\odot$, by 0.075 ± 0.012 and 0.077 ± 0.017).

5. Blue galaxies in voids have slightly lower stellar metallicities than blue galaxies in filaments & walls at low stellar masses ($10^{9.25}$ $M_\odot$, by 0.091 ± 0.020) but not significant differences are found between red galaxies in voids and filaments & walls. Red galaxies in voids have slightly lower stellar metallicities than red galaxies in clusters, more significantly at lower stellar masses ($10^{9.75}$ $M_\odot$ by 0.103 ± 0.016) than at higher stellar masses ($10^{10.75}$ $M_\odot$ by

0.066 ± 0.013). Blue galaxies in voids have lower stellar metallicities than blue galaxies in clusters, more significantly at lower stellar masses ($10^{9.25}$ $M_\odot$ by 0.315 ± 0.023) than at higher stellar masses ($10^{9.75}$ $M_\odot$ by 0.150 ± 0.015).

In summary, galaxies in voids and filaments & walls have similar stellar metallicities, except for intermediate stellar masses, where void galaxies have slightly lower stellar metallicities. Void galaxies have lower stellar metallicities than galaxies in clusters (more significantly at low than at high stellar masses). These differences can be explained by the slower SFHs of voids galaxies, specially at the initial star formation period in LT-SFH galaxies. Additionally, if we assume a good correlation between the stellar and gas-phase metallicities of star forming galaxies (i.e. blue and spiral galaxies, for which we find the highest stellar metallicity differences between galaxies in different large-scale environments, compared to red and elliptical galaxies, where the differences are less significant), we can explain the lower stellar metallicity of void galaxies at intermediate stellar masses ($M_\star < 10^{10.5}$ $M_\odot$) based on their higher halo-to-stellar mass ratio, and higher gas accretion. However, further research is needed in terms of gas mass content, gas-phase metallicity, and nuclear activity of void galaxies, together with the correlation between these physical processes and the SFH. The CAVITY project aims to fulfill these needs by analysing the resolved emission lines, stellar populations, and kinematics from PPAK IFU data, together with ancillary data, such as atomic and molecular gas of galaxies in voids.

Conclusions and future work

In this thesis we study how the large-scale structure of the Universe affects the star formation properties of galaxies by analysing their molecular gas and stellar populations. In the first part, we observed and analyse the CO$(1-0)$ and CO$(2-1)$ emission lines of 20 void galaxies in the IRAM 30 m telescope and derived their molecular gas mass to compare with galaxies in filaments and walls, together with the atomic gas mass and star formation rate obtained from the literature. This is a pilot survey of the current CO-CAVITY survey with around 100 galaxies observed up to date. In the second part of the thesis we derived the SFH and stellar metallicity from the SDSS optical spectrum from the centre of thousands of galaxies by applying non parametric full spectral fitting techniques (pPXF and STECKMAP), and compare galaxies in different large-scale environments: voids, filaments & walls, and clusters. This is a preparatory study of the galaxy mother sample of the CAVITY project. Our main conclusions of both parts are the following:

1. We do not find significant differences in the molecular gas, atomic gas, sSFR, and SFE properties for a given stellar mass between galaxies in voids and galaxies in filaments and walls, except for some stellar mass bins where the atomic gas mass ($M_\star > 10^{9.5}$ M$_\odot$) and SFE ($M_\star < 10^{9.5}$ M$_\odot$) are tentatively lower in void galaxies. However, due to the low number of galaxies in these stellar mass bins (four to five objects), the results need to be confirmed with a larger sample of void galaxies.

2. There are two types of SFHs, which are present in all the large-scale structures of the Universe. ST-SFH galaxies assembled a

high fraction (> 21.5%) of their stellar mass very early (> 12.5 Gyr ago) and progressively quenched later. LT-SFH galaxies formed a lower fraction of their stellar mass at that time but keep forming stars later. On average, void galaxies with both SFH types form their star slower than galaxies in filaments & walls, and much slower than galaxies in clusters.

3. Void galaxies have slightly lower stellar metallicities than galaxies in filaments & walls at intermediate stellar masses, and much lower than galaxies in clusters at any given stellar mass. These differences are more relevant for LT-SFH than for ST-SFH galaxies, for spiral than for elliptical, and for blue than for red galaxies.

In summary, we show in this thesis that voids host a population of galaxies that have evolved slower, and have metal-poorer stars than galaxies in denser environments, but we do not find significant differences in their current and potential star formation when we analyse the SFR and molecular gas. These results, open a new set of questions that fall beyond the scope of this thesis but can be answered in future studies:

- The number of galaxies with molecular and atomic gas data in the analysis that we carry out in Chapter 3 is too low to draw strong conclusions about the gas content of void galaxies, and more significant statistics is needed to confirm our results. This is going to be addressed soon by the CO-CAVITY project, which has observed around 100 galaxies with the IRAM 30 m telescope. In addition, another sub-project of CAVITY, the HI-CAVITY project, has recently obtained 146.25 hours of observation with the GBT radio telescope in West Virginia to measure the 21 cm emission line and derive the atomic gas mass of CO-CAVITY galaxies. These two sets of new observations will allow us to better understand the gas content differences between galaxies in different large-scale environments.

- We showed in Figure 5.4 that the SFH types do not clearly correlate with the current colour or morphology of the galaxies. However, the SFH type of a galaxy is directly linked to its evolution over the CMD. A future work would characterise the distribution of SFH types over the CMD, estimate how the galaxies evolve, and compare different large-scale environments.

- The results of our stellar population analysis is limited to the centres of the galaxies. Therefore, further research is needed to confirm that our results are also valid for the outer regions of the galaxies. The main goal of the CAVITY project is to observe around 300 void galaxies with the PMAS-PPAK IFU in the Calar Alto Observatory. The IFU data will give us spatially resolved spectral information of the galaxies, and will allow us to study their stellar populations, not only in their centres but also within their entire disks.

- Previous works have studied how the local environment affects the stellar populations of galaxies. They analyse the stellar ages and metallicities of groups of galaxies, and compare central and satellite galaxies for a given stellar mass or for a given halo mass. Among other results, they find signs of dry mergers in red sequence galaxies. However, they do not make any analysis of the large-scale effect. In this thesis, we have compared the stellar populations of galaxies in voids, filaments & walls, and clusters but we did not make any analysis of the local environment effect. In a future work, satellite and central galaxies can be compared as a function of the large-scale environment. This analysis will allow us to better understand how galaxy evolution is affected by the environment, from local to large-scale. In addition, if we find less signs of dry-mergers in voids, it might explain the different slope of the red sequence that we see on the CMD for different large-scale structures in Figure 2.4.

Conclusiones y trabajo futuro

En esta tesis estudiamos cómo la estructura a gran escala del Universo afecta las propiedades de formación estelar de las galaxias mediante el análisis del gas molecular y las poblaciones estelares. En la primera parte, observamos las líneas de emisión CO($1-0$) y CO($2-1$) de 20 galaxias de vacíos en el telescopio de 30 m del IRAM y derivamos la masa de gas molecular para compararlas con las galaxias en filamentos y muros, junto con la masa de gas atómico y la tasa de formación estelar obtenidas de la literatura. Ésta es una muestra piloto del proyecto CO-CAVITY, que ha observado unas 100 galaxias hasta ahora. En la segunda parte de la tesis, derivamos la historia de formación estelar (SFH) y la metalicidad estelar a partir de los espectros ópticos del SDSS de miles de galaxias mediante técnicas no parametrizadas de ajuste espectral completo (pPXF y STECKMAP) y comparamos galaxias en diferentes entornos a gran escala: vacíos, filamentos & muros, y cúmulos. Éste es un estudio preparatorio de la muestra madre de galaxias del proyecto CAVITY. Nuestras principales conclusiones son las siguientes:

1. No encontramos diferencias significativas en las propiedades de gas molecular, gas atómico, tasa de formación estelar específica, y eficiencia de formación estelar para una masa estelar dada entre las galaxias de vacíos y las galaxias de filamentos y muros, excepto para algunos intervalos de masa estelar donde la masa de gas atómico ($M_\star > 10^{9.5}\mathrm{M}_\odot$) y la eficiencia de formación estelar ($M_\star < 10^{9.5}\mathrm{M}_\odot$) son tentativamente más bajas en las galaxias de vacíos. Sin embargo, debido al bajo número de galaxias en estos intervalos de masa estelar (cuatro a cinco objetos), los resultados

deben confirmarse para una muestra más grande de galaxias de vacíos.

2. Existen dos tipos de historias de formación estelar (SFH) que están presentes en todas las estructuras a gran escala del Universo. Las galaxias con una SFH de corta escala de tiempo (ST-SFH, por sus siglas en inglés) ensamblaron una fracción alta ($> 21.5\%$) de su masa estelar en una etapa temprana (hace más de 12.5 Gyr) y se apagaron progresivamente más tarde. Las galaxias con una SFH de larga escala de tiempo (LT-SFH, por sus siglas en inglés) formaron una fracción menor de su masa estelar en esa etapa, pero continuaron formando estrellas más tarde. En promedio, las galaxias de vacíos con ambos tipos de SFH forman estrellas más lentamente que las galaxias en filamentos & muros, y mucho más lentamente que las galaxias de cúmulos.

3. Las galaxias de vacíos tienen ligeramente menor metalicidad estelar que las galaxias de filamentos & muros a masas estelares intermedias, y mucho menor metalicidad que las galaxias de cúmulos a cualquier masa estelar. Estas diferencias son más relevantes para LT-SFH que para ST-SFH, más relevantes para galaxias espirales que para galaxias elípticas, y más relevantes para galaxias azules que para galaxias rojas.

En resumen, en esta tesis mostramos que los vacíos albergan una población de galaxias que han evolucionado más lentamente y tienen estrellas con menor metalicidad que las galaxias en ambientes más densos. Sin embargo, no encontramos diferencias significativas en su actividad actual y potencial de formación estelar cuando analizamos la tasa de formación estelar y el gas molecular. Estos resultados dejan abiertas nuevas cuestiones que caen fuera del alcance de esta tesis, pero que se pueden responder en estudios futuros:

- El número de galaxias con datos de gas molecular y gas atómico en el análisis del Capítulo 3 es bajo para llegar a una conclusión sólida sobre el contenido de gas en las galaxias de vacíos, y se necesita una mayor estadística para confirmar nuestros resultados. Esto se abordará próximamente con el proyecto CO-CAVITY, que ha observado alrededor de 100 galaxias con el telescopio de 30 m del IRAM. Además, otro subproyecto de CAVITY, el proyecto HI-CAVITY, ha obtenido recientemente 146.25 horas

de observación con el radiotelescopio GBT en West Virginia para medir las líneas de emisión de 21cm y calcular la masa de gas atómico de las galaxias de CO-CAVITY. Estos dos nuevas muestras nos permitirán comprender mejor las diferencias del contenido de gas entre las galaxias en diferentes ambientes a gran escala.

- En la Figura 5.4 mostramos que los tipos de SFH no correlacionan claramente con el color o la morfología actuales de las galaxias. Sin embargo, el tipo de SFH de una galaxia está directamente vinculado a su evolución en el diagrama color-magnitud (CMD, por sus siglas en inglés). En un trabajo futuro se podría caracterizar la distribución de los tipos de SFH en el CMD, estimar cómo evolucionan las galaxias y comparar diferentes ambientes a gran escala.

- Los resultados de nuestro análisis de poblaciones estelares se limitan al centro de las galaxias. Por lo tanto, se necesita ampliar la investigación para confirmar que nuestros resultados son extrapolables a las regiones exteriores de las galaxias. El objetivo principal del proyecto CAVITY es observar alrededor de 300 galaxias de vacíos con el espectrógrafo de campo integral (IFU, por sus siglas en inglés) PMAS-PPAK del Observatorio de Calar Alto. Los datos del IFU nos proporcionarán información espectral espacialmente resuelta de las galaxias y nos permitirán estudiar sus poblaciones estelares, no sólo en el centro sino también en todo el disco.

- Trabajos anteriores han estudiado cómo el entorno local afecta a las poblaciones estelares de las galaxias. Analizan las edades y metalicidades estelares de grupos de galaxias, y comparan galaxias centrales y satélites para una masa estelar dada o para una masa de halo dada. Entre otros resultados, encuentran indicios de fusiones en seco de galaxias de la secuencia roja. Sin embargo, no realizan ningún análisis del ambiente a gran escala. En esta tesis, hemos comparado las poblaciones estelares de galaxias de vacíos, filamentos & muros, y cúmulos, pero no hemos realizado ningún análisis del ambiente local. En un trabajo futuro, se podrían comparar galaxias satélites y centrales en función del ambientes a gran escala. Este análisis nos permitiría comprender mejor cómo la evolución de las galaxias se ve afectada por su

entorno, desde el ambiente local hasta el ambiente a gran escala. Además, si se encontrasen menos indicios de fusiones en seco en los vacíos, podrían explicarse las diferentes pendientes de la secuencia roja que vemos en el CMD (Figura 2.4) para diferentes estructuras a gran escala.

Appendices

Appendix A

Molecular gas additional analysis

A.1 Theoretical $\mathrm{CO}(2-1)$-to-$\mathrm{CO}(1-0)$ line ratio

In this section we estimate the $\mathrm{CO}(2-1)$-to-$\mathrm{CO}(1-0)$ line ratio theoretical value, $R_{21\mathrm{theo}}$, assuming a Gaussian power pattern of the antenna and an exponential distribution of the CO emission in the galaxy.

The measured main beam temperature can be expressed as

$$T_{\mathrm{mb}}(\nu) = \frac{\int_{-\infty}^{\infty}\int_{-\infty}^{\infty} T_{\mathrm{B}}(x,y,\nu)P_{\mathrm{n}}(x,y)\mathrm{d}x\mathrm{d}y}{\int_{-\infty}^{\infty}\int_{-\infty}^{\infty} P_{\mathrm{n}}(x,y)\mathrm{d}x\mathrm{d}y}, \tag{A.1}$$

where P_{n} is the normalised power pattern of the antenna beam, and T_{B} is the brightness temperature of the source.

P_{n} is assumed to be a Gaussian distribution, $G[\Theta]$,

$$P_{\mathrm{n}}(x,y) = \exp\left(-\ln 2\left[\left(\frac{2x}{\Theta}\right)^2 + \left(\frac{2y}{\Theta}\right)^2\right]\right) = G[\Theta], \tag{A.2}$$

where Θ is the FWHM of the antenna beam ($\Theta_{10} = 22''$ and $\Theta_{21} = 11''$).

The velocity-integrated emission line intensity is

$$I_{\mathrm{CO}} = \int_{line} T_{\mathrm{mb}}(\nu)\mathrm{d}\nu. \tag{A.3}$$

In the same way as for the aperture correction, we assumed that the spatial distribution of the intrinsic brightness temperature is an exponential disc with an inclination i with respect to the line of sight. This intrinsic brightness temperature distribution, as observed in the coordinate system (x, y) in the plane of the sky, for this case is

$$T_{\rm B}(x,y,\nu) = \frac{T_{\rm Bc}(\nu)}{\cos(i)} \exp\left(-\frac{\sqrt{x^2+(y/\cos(i))^2}}{r_{\rm e}}\right) = T_{\rm Bc}(\nu) E[r_{\rm e}, i], \tag{A.4}$$

where $T_{\rm Bc}(\nu)$ is the intrinsic brightness temperature at the centre of the source, $r_{\rm e}$ is the exponential scale factor, which is derived from R_{90} as described in Sect. 3.1.1, and i is the inclination of the galaxy. The factor involving the inclination appears twice in the function: firstly, in the denominator, because the intrinsic brightness temperature is higher in an inclined galaxy by $1/\cos(i)$ for a given distance on the sky, (x, y), because of the higher apparent disc-thickness;and secondly, because the physical position along the radius of the galactic disc, y', is higher than the projected position on the sky, y.

Inserting this distribution (eq. A.4) and the Gaussian beam distribution (eq. A.2) into eq. A.1, we obtain for the measured main-beam temperature at the central position of the galaxy

$$\begin{aligned} T_{\rm mb}(\nu) &= \frac{\int_{-\infty}^{\infty}\int_{-\infty}^{\infty} T_{\rm Bc}(\nu) E[r_{\rm e}, i] G[\Theta] {\rm d}x{\rm d}y}{\int_{-\infty}^{\infty}\int_{-\infty}^{\infty} G[\Theta]{\rm d}x{\rm d}y} = \\ &\frac{\int_{-\infty}^{\infty}\int_{-\infty}^{\infty} \frac{T_{\rm Bc}(\nu)}{\cos(i)} \exp\left(-\frac{\sqrt{x^2+\left(\frac{y}{\cos(i)}\right)^2}}{r_{\rm e}}\right) \exp\left(-\ln 2\left[\left(\frac{2x}{\Theta}\right)^2+\left(\frac{2y}{\Theta}\right)^2\right]\right){\rm d}x{\rm d}y}{\int_{-\infty}^{\infty}\int_{-\infty}^{\infty} G[\Theta]{\rm d}x{\rm d}y} = \\ &\frac{\int_{-\infty}^{\infty}\int_{-\infty}^{\infty} T_{\rm Bc}(\nu) \exp\left(-\frac{\sqrt{x^2+(y')^2}}{r_{\rm e}}\right) \exp\left(-\ln 2\left[\left(\frac{2x}{\Theta}\right)^2+\left(\frac{2y'\cos(i)}{\Theta}\right)^2\right]\right){\rm d}x{\rm d}y'}{\int_{-\infty}^{\infty}\int_{-\infty}^{\infty} G[\Theta]{\rm d}x{\rm d}y} = \\ &\frac{\int_{-\infty}^{\infty}\int_{-\infty}^{\infty} T_{\rm Bc}(\nu) E'[r_{\rm e}] G'[\Theta, i] {\rm d}x{\rm d}y'}{\int_{-\infty}^{\infty}\int_{-\infty}^{\infty} G[\Theta]{\rm d}x{\rm d}y} \end{aligned} \tag{A.5}$$

where we made the substitution $y' = y/\cos(i)$.

We suppose that the line shape, $\psi(\nu)$, is the same for both CO(1−0) and CO(2 − 1) emission lines,

$$\frac{T_{\mathrm{Bc2-1}}(\nu)}{T_{\mathrm{Bc1-0}}(\nu)} = \frac{\bar{T}_{\mathrm{Bc2-1}}\psi(\nu)}{\bar{T}_{\mathrm{Bc1-0}}\psi(\nu)} = \frac{\bar{T}_{\mathrm{Bc2-1}}}{\bar{T}_{\mathrm{Bc1-0}}}. \tag{A.6}$$

Then, $R_{21\mathrm{theo}}$ is calculated as

$$R_{21\mathrm{theo}} = \frac{I_{\mathrm{CO(2-1)}}}{I_{\mathrm{CO(1-0)}}} = \frac{\bar{T}_{\mathrm{Bc2-1}}}{\bar{T}_{\mathrm{Bc1-0}}} \left(\frac{\Theta_{1-0}}{\Theta_{2-1}}\right)^2 \frac{\int_{-\infty}^{\infty}\int_{-\infty}^{\infty} E'[r_{\mathrm{e}}]G'[\Theta_{2-1}, i]\mathrm{d}x\mathrm{d}y'}{\int_{-\infty}^{\infty}\int_{-\infty}^{\infty} E'[r_{\mathrm{e}}]G'[\Theta_{1-0}, i]\mathrm{d}x\mathrm{d}y'}, \tag{A.7}$$

where we used the identity $\int_{-\infty}^{\infty}\int_{-\infty}^{\infty} G[\Theta]\mathrm{d}x\mathrm{d}y = \frac{\pi}{4\ln 2}\Theta^2$. The integrals were calculated numerically for each galaxy in this study.

A.2 Selection of SFR tracer

For a correct comparison of the different samples, we need to employ the same tracer for the SFR, or, if this is not possible, test whether different tracers give consistent results. In addition, the calibrations need to be based on the same initial mass function (IMF). Here, we used the Kroupa IMF (Kroupa 2001), which is very similar to the IMF by Chabrier (Chabrier 2003).

The SFR of the xCOLD GASS sample was derived from the NUV and MIR emission and followed the prescription from Janowiecki et al. (2017). The SFR of the HI-CALIFA sample was derived and calibrated from extinction-corrected Hα fluxes in Catalán-Torrecilla et al. (2015), resulting in practically the same prescription as we used (eq. 3.1) (difference $< 2\%$, which is negligible). Finally, the SFRs from the MPA-JHU were available for all samples.

In Fig. A.2.1 we compare the SFR from the MPA-JHU (Brinchmann et al. 2004) to the SFR derived from different tracers in the different studies. We find that for galaxies with a low SFR ($< 10^{-1}\,\mathrm{M_\odot\,yr^{-1}}$), the SFR from the MPA-JHU is overestimated for the VGS on average, but it is underestimated for the comparison sample. A similar result was obtained by Duarte Puertas et al. (2017). This suggests that the Hα aperture correction of the MPA-JHU might overestimate the SFR for small galaxies such as the VGS (values of $R_{90} \sim 4 - 15$ arcsec) and might underestimate it for larger galaxies such as the HI-CALIFA sample or xCOLD GASS ($R_{90} \sim 20 - 45$ arcsec). Fig. A.2.2 shows the SFR differences between the MPA-JHU and the tracer used in this work (for the different samples) as a function of the apparent size of the galaxy.

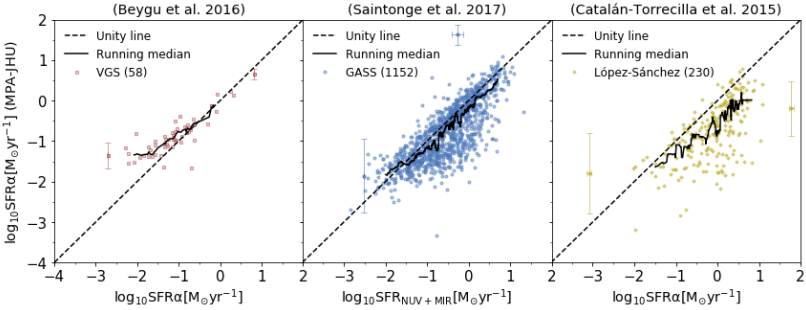

Figure A.2.1: Star formation rate from the MPA-JHU compared to the SFR derived from different tracers. Left: SFR of the VGS derived from Hα maps (Beygu et al. 2016). Centre: SFR of the xCOLD GASS sample derived from NUV and MIR emission (Saintonge et al. 2017). Right: SFR of the HI-CALIFA sample derived from Hα maps (Catalán-Torrecilla et al. 2015).

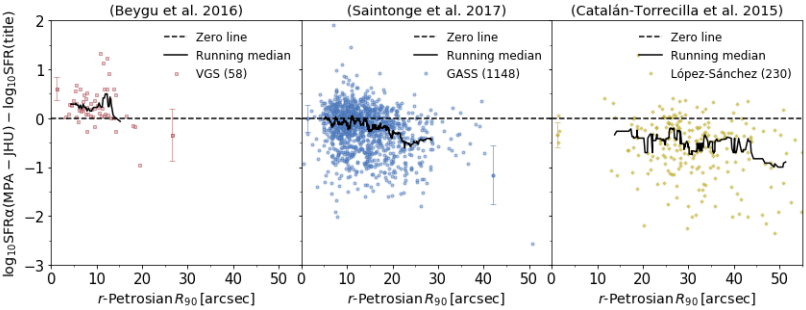

Figure A.2.2: Difference between the SFR from the MPA-JHU and the SFR derived from different tracers represented as a function of the apparent size of the galaxy (r-Petrosian R_{90}). Left: Difference between the SFR of the VGS derived from the MPA-JHU and the SFR derived from Hα maps (Beygu et al. 2016). Centre: Difference between the SFR of the xCOLD GASS sample derived from the MPA-JHU and the SFR derived from NUV and MIR emission (Saintonge et al. 2017). Right: Difference between the SFR of the HI-CALIFA sample derived from the MPA-JHU and the SFR derived from Hα maps (Catalán-Torrecilla et al. 2015).

In Fig. A.2.3 we compare the SFR derived from NUV and MIR to the values derived from Hα in order to test whether we obtain consistent results with the different prescription. First, we repeated the calculation of the SFR derived from NUV and MIR following Janowiecki et al. (2017) for the xCOLD GASS and compare their results to ours in Fig. A.2.3 (centre). We conclude that we have repeated the method accurately. Then, we applied this method to the VGS and the HI-CALFIA samples and compare in Fig. A.2.3 (left and right) our results to the SFR derived from Hα maps by Beygu et al. (2016) and

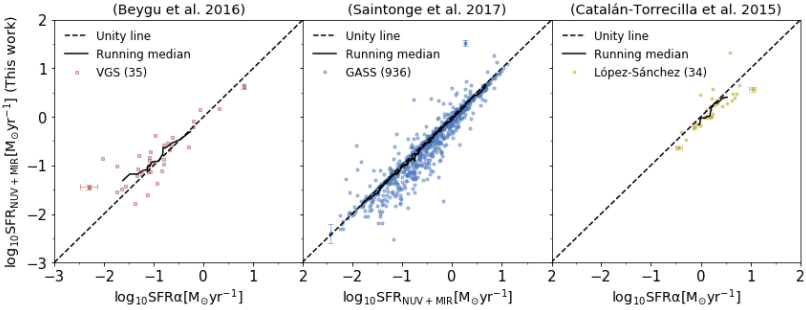

Figure A.2.3: Star formation rate tracer derived from NUV and MIR emission, following the prescription in Janowiecki et al. (2017), derived in the present thesis and compared with different SFR tracer. Left: SFR of the VGS derived from Hα maps (Beygu et al. 2016). Centre: SFR of the xCOLD GASS sample derived from NUV and MIR emission (Saintonge et al. 2017). Right: SFR of the HI-CALIFA sample derived from Hα maps (Catalán-Torrecilla et al. 2015).

Catalán-Torrecilla et al. (2015), respectively.

The comparisons show some scatter, but the running median follows the unity line for the VGS, the xCOLD GASS, and HI-CALIFA samples very well. We conclude that the SFR tracer from Janowiecki et al. (2017) is repeated accurately in the present thesis, and it is equivalent to the SFR tracers derived from Hα maps in Beygu et al. (2016) and Catalán-Torrecilla et al. (2015).

Finally, we use the SFR derived from H_α maps by Beygu et al. (2016) for the VGS, the SFR derived from Hα maps in Catalán-Torrecilla et al. (2015) for the HI-CALIFA sample, and the SFR derived from NUV and MIR emission by Saintonge et al. (2017) for the xCOLD GASS sample.

A.3 CO emission line spectra

Figs. A.3.1 and A.3.2 show the observed spectra of the CO$(1-0)$ and CO$(2-1)$ emission lines, respectively.

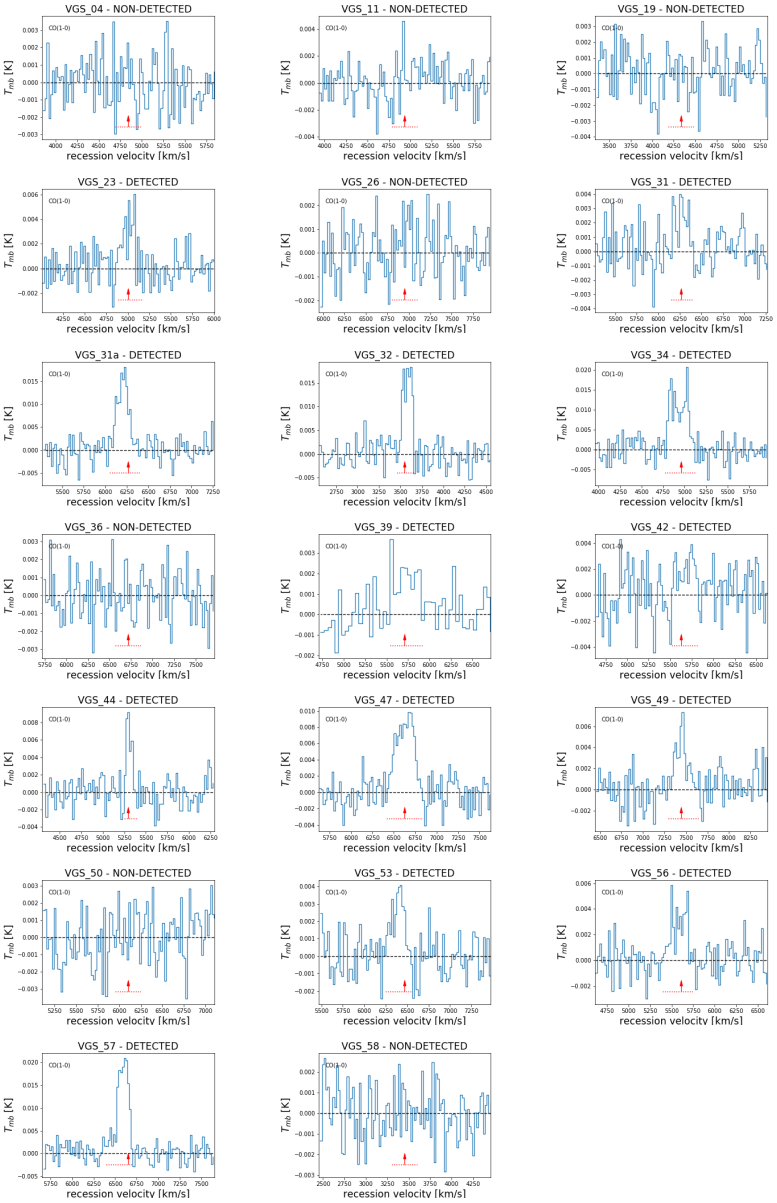

Figure A.3.1: Spectral representation of the CO(1 − 0) emission line $T_{\rm mb}$ in K at $\sim 20\,{\rm km\,s^{-1}}$ of the velocity resolution. The red arrow indicates the optical heliocentric recession velocity. The dotted red line shows the zero-level line width at which the velocity-integrated intensity has been calculated.

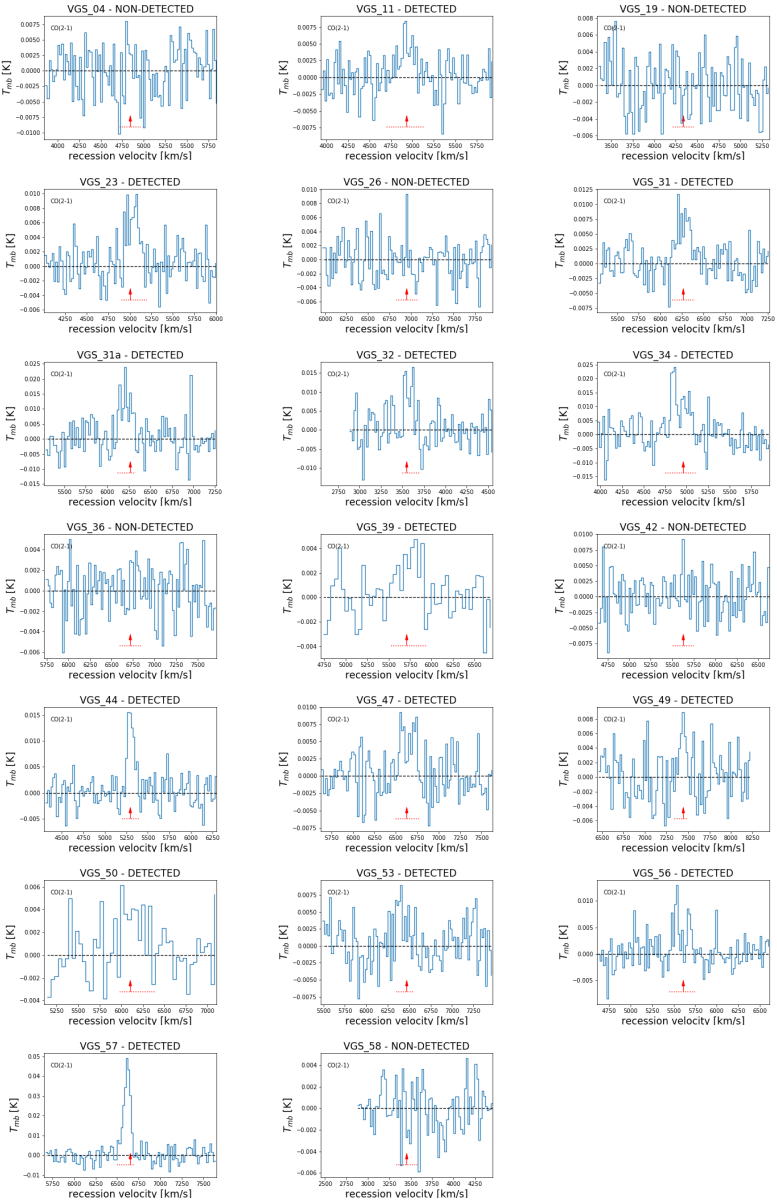

Figure A.3.2: Spectral representation of the CO(2 − 1) emission line $T_{\rm mb}$ in K at $\sim 20\,{\rm km\,s^{-1}}$ of the velocity resolution. The red arrow indicates the optical heliocentric recession velocity. The dotted red line shows the zero-level line width at which the velocity-integrated intensity has been calculated.

Appendix B

Stellar metallicity additional analysis

B.1 Stellar mass-metallicity relation for stellar mass adjusted samples

We showed in Figure 2.5 the colour vs. stellar mass diagram distribution of our galaxy samples. Void galaxies are on average bluer and less massive than galaxies in denser environments. Our stellar metallicity analysis might be affected by the different stellar mass distribution of the three samples. We define 5 stellar mass bins of 0.5 dex between $10^{8.5}$ and $10^{11.0}$ $M_{\odot}$ and select random sub-samples with the same stellar mass distribution as our void galaxy sample inside each stellar mass bin (see Section 2.2.3).

In figures B.1.1-B.1.3 we show the same as figures 6.2-6.4, respectively, but for the sub-samples with the same stellar mass distribution inside each stellar mass bin. The values represented in the figures are reported in tables B.7-B.12. The stellar metallicity differences that we find between galaxies in voids, filaments & walls, and cluster for the sub-samples with the same stellar mass distribution are similar to what we find in Chapter 6 for the main sample. In addition, in Figure B.1.4 we show the same as in Figure 6.4 for red and blue galaxies but with the colour classification criterion at 0.6 instead of 0.7 mag. The results change but the general tendency is similar.

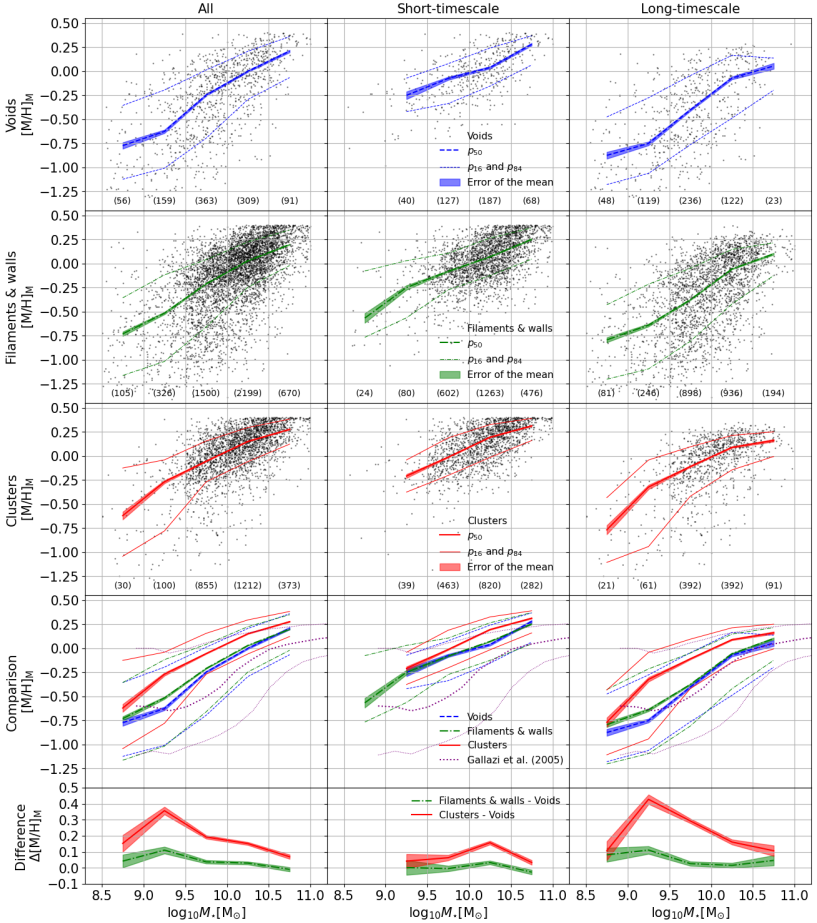

Figure B.1.1: Same as Figure 6.2 but for the sub-samples of galaxies with the same stellar mass distribution. See values reported in tables B.7 and B.8.

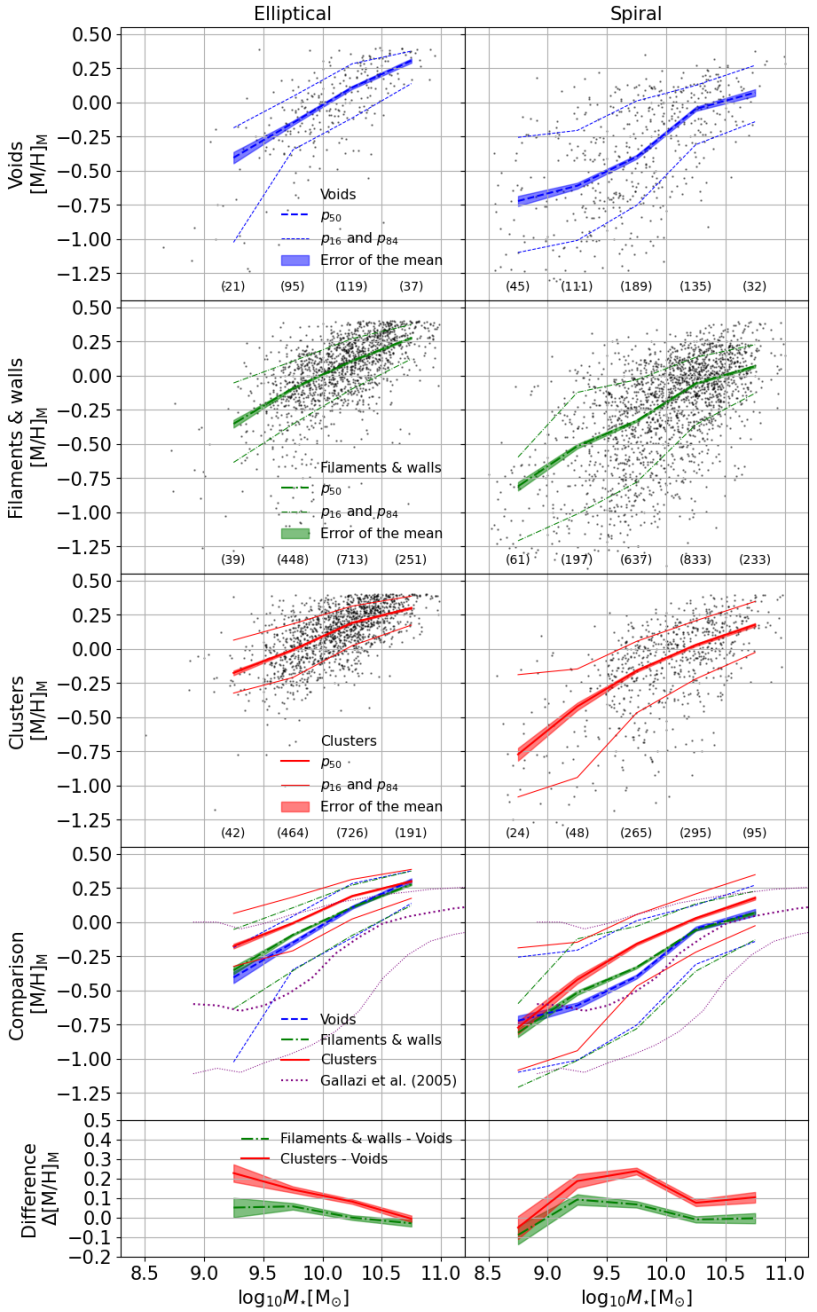

Figure B.1.2: Same as Figure 6.3 but for the sub-samples of galaxies with the same stellar mass distribution. See values reported in tables B.9 and B.10.

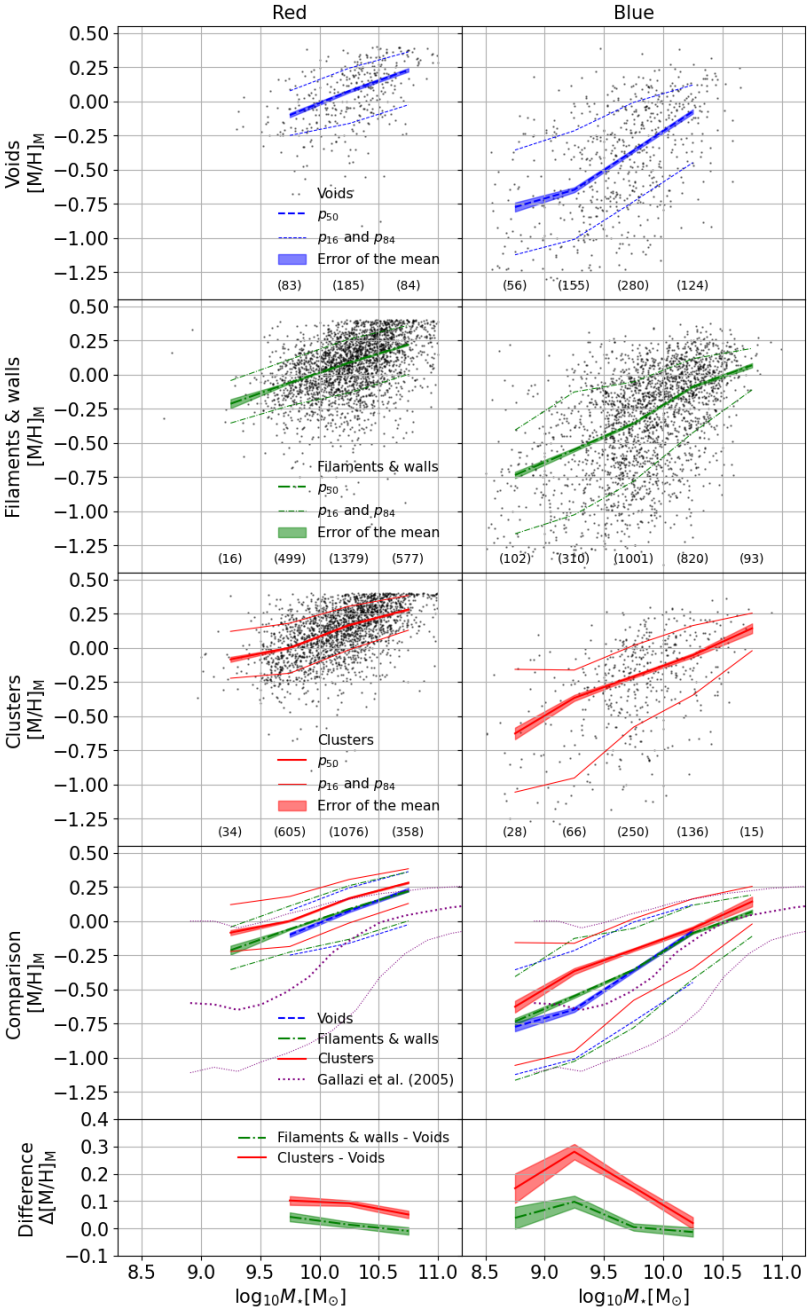

Figure B.1.3: Same as Figure 6.4 but for the sub-samples of galaxies with the same stellar mass distribution. See values reported in tables B.11 and B.12.

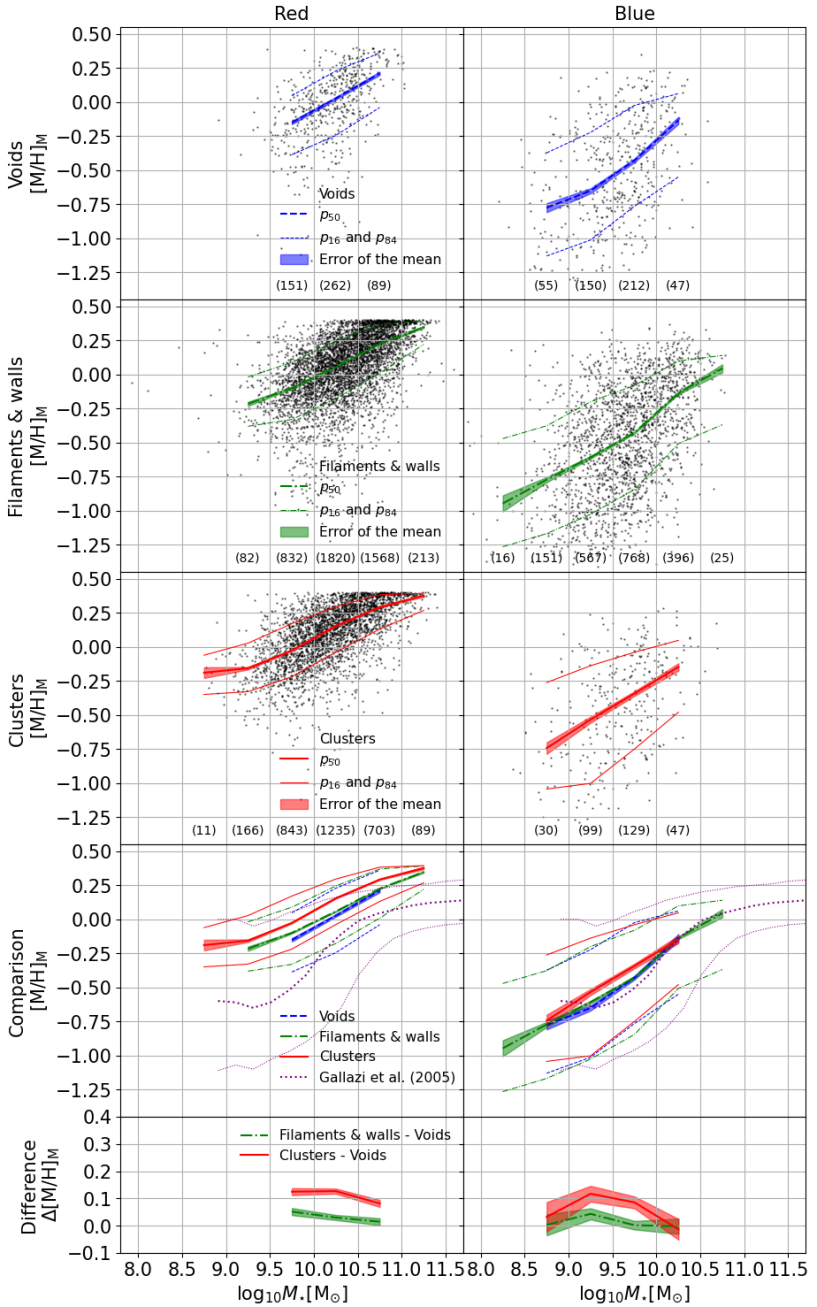

Figure B.1.4: Same as Figure 6.4 but with the colour classification criterion at 0.6 instead of 0.7. See values reported in tables B.13 and B.14.

B.2 Luminosity-weighted stellar mass-metallicity relation

In this section we present the $MZ_{\star}R$ for different SFH types (Figure B.2.1), morphologies (Figure B.2.2), and colours (Figure B.2.3) when the stellar metallicity of a galaxy is calculated as the luminosity-weighted average:

$$[M/H]_{L} = \frac{\sum L_{\star}[M/H]_{\star}}{\sum L_{\star}}$$

where $L_{\star}$ and $[M/H]_{\star}$ are the luminosity and metallicity of the stars within the galaxy, which are derived using STECKMAP in Chapter 4.

The luminosity-weighted stellar metallicities differences that we find between galaxies in different large-scale environments are similar to what we find in Chapter 6 for the mass-weighted average.

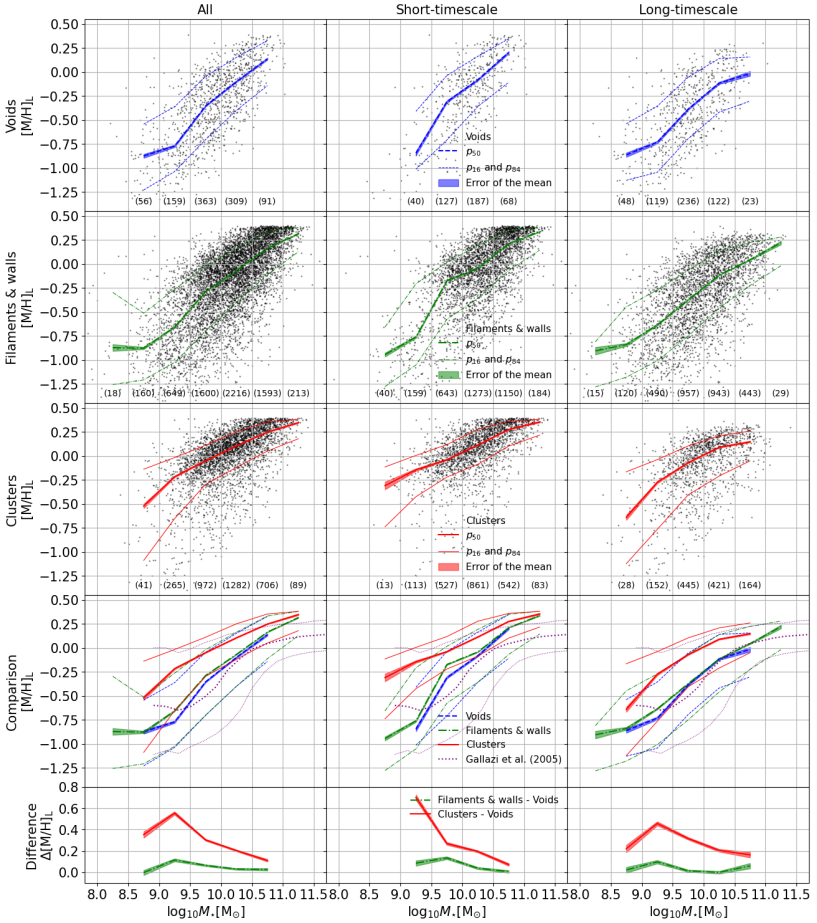

Figure B.2.1: Same as Figure 6.2 but for the stellar metallicity calculated as the luminosity-weighted average. See values reported in tables B.15 and B.16.

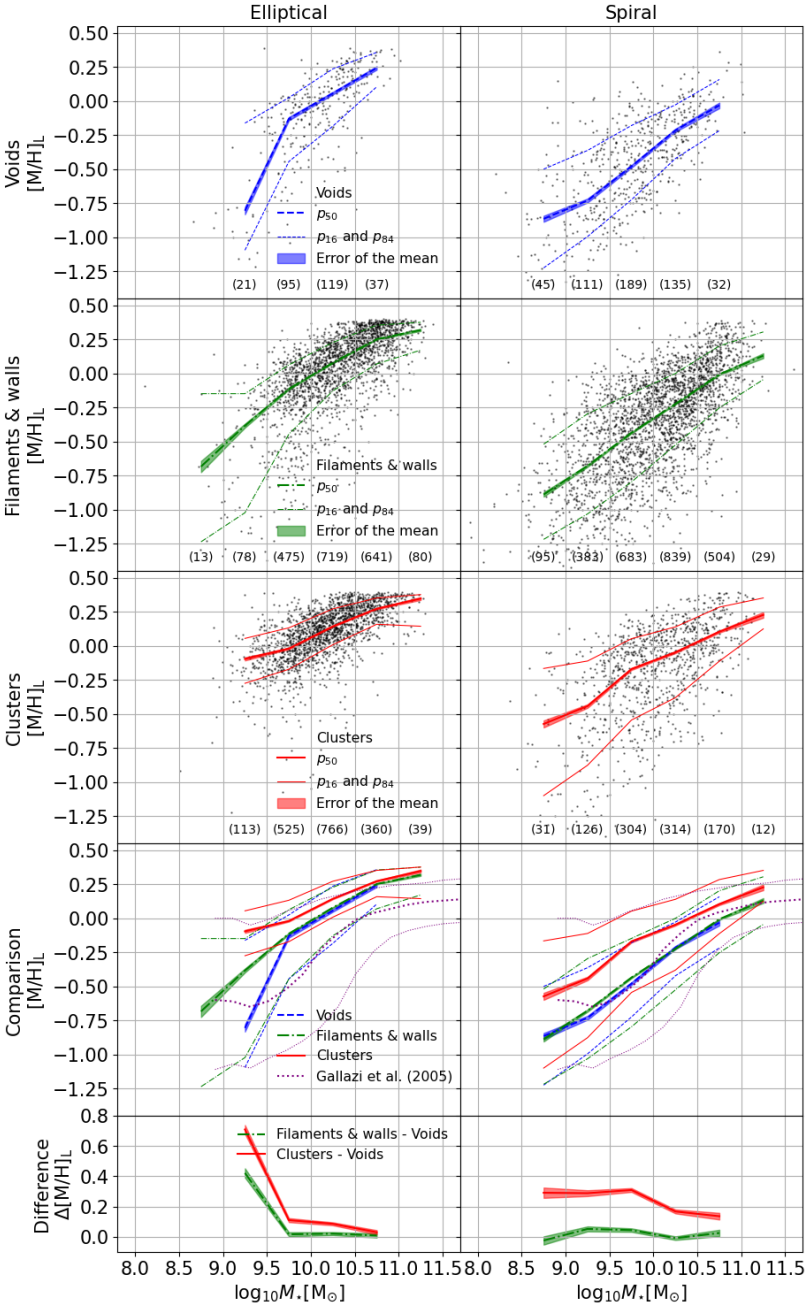

Figure B.2.2: Same as Figure 6.3 but for the stellar metallicity calculated as the luminosity-weighted average. See values reported in tables B.17 and B.18.

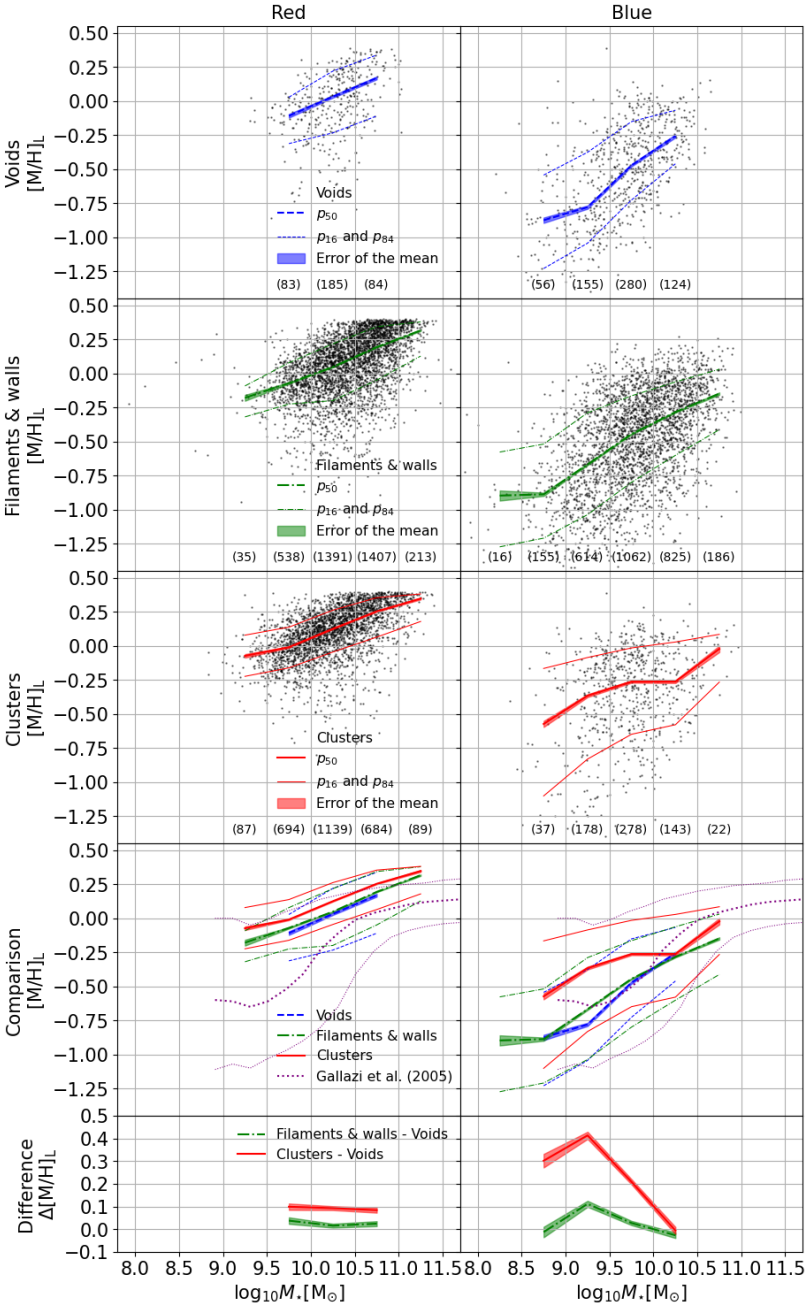

Figure B.2.3: Same as Figure 6.4 but for the stellar metallicity calculated as the luminosity-weighted average. See values reported in tables B.19 and B.20.

B.3 Tables of the stellar mass-metallicity relation

In this section we report the $MZ_{\star}R$ in tables. In tables B.1 and B.2 we present values represented in Figure 6.2 for all the galaxies, galaxies with ST-SFH and galaxies with LT-SFH. In table B.3 and B.4 we present values represented in Figure 6.3 for elliptical and spiral galaxies. In tables B.5 and B.6 we present values represented in Figure 6.4 for red and blue galaxies with the classification criterion at 0.7 mag. In tables B.7-B.12 we present values represented in figures B.1.1-B.1.3 for the sub-samples with the same stellar mass distribution. In tables B.13 and B.14 we present values represented in Figure B.1.4 for red and blue galaxies with the classification criterion at 0.6 mag. In tables B.15-B.20 we present values represented in figures B.2.1-B.2.3 for the luminosity-weighted average.

	[M/H]$_M$											
	All				ST-SFH				LT-SFH			
$\log_{10} M_\star[M_\odot]$	n	p_{50}	p_{16}	p_{84}	n	p_{50}	p_{16}	p_{84}	n	p_{50}	p_{16}	p_{84}
(a) Voids												
8.25	4	-	-	-	1	-	-	-	3	-	-	-
8.75	56	-0.77±0.03	-1.12	-0.36	8	-	-	-	48	-0.88±0.04	-1.18	-0.48
9.25	159	-0.627±0.017	-1.01	-0.20	40	-0.25±0.04	-0.42	-0.07	119	-0.752±0.019	-1.06	-0.28
9.75	363	-0.247±0.009	-0.70	0.01	127	-0.076±0.016	-0.34	0.08	236	-0.403±0.012	-0.77	-0.05
10.25	309	-0.000±0.009	-0.29	0.21	187	0.038±0.011	-0.16	0.24	122	-0.072±0.014	-0.49	0.16
10.75	91	0.208±0.012	-0.07	0.36	68	0.279±0.013	0.06	0.37	23	0.05±0.03	-0.20	0.14
11.25	4	-	-	-	3	-	-	-	1	-	-	-
(b) Filaments & walls												
8.25	18	-0.92±0.05	-1.24	-0.21	3	-	-	-	15	-0.95±0.06	-1.28	-0.58
8.75	160	-0.737±0.018	-1.16	-0.31	40	-0.49±0.04	-0.73	-0.05	120	-0.865±0.021	-1.20	-0.43
9.25	649	-0.519±0.009	-1.01	-0.13	159	-0.255±0.017	-0.57	0.05	490	-0.648±0.01	-1.06	-0.24
9.75	1600	-0.211±0.004	-0.66	0.04	643	-0.080±0.006	-0.27	0.11	957	-0.374±0.006	-0.81	-0.05
10.25	2216	0.031±0.003	-0.24	0.23	1273	0.073±0.004	-0.12	0.27	943	-0.056±0.005	-0.42	0.15
10.75	1593	0.223±0.003	0.00	0.37	1150	0.277±0.003	0.07	0.38	443	0.111±0.006	-0.13	0.24
11.25	213	0.347±0.007	0.22	0.39	184	0.370±0.007	0.24	0.39	29	0.241±0.022	0.10	0.28
(c) Clusters												
8.25	2	-	-	-	0	-	-	-	2	-	-	-
8.75	41	-0.55±0.03	-0.96	-0.16	13	-0.18±0.06	-0.40	-0.05	28	-0.67±0.04	-1.06	-0.30
9.25	265	-0.23±0.01	-0.60	-0.01	113	-0.146±0.014	-0.33	0.05	152	-0.333±0.015	-0.85	-0.07
9.75	972	-0.054±0.004	-0.27	0.16	527	-0.012±0.005	-0.20	0.19	445	-0.108±0.007	-0.42	0.10
10.25	1282	0.148±0.003	-0.06	0.29	861	0.190±0.004	-0.02	0.32	421	0.089±0.006	-0.15	0.21
10.75	706	0.292±0.004	0.13	0.38	542	0.319±0.004	0.18	0.39	164	0.166±0.009	-0.00	0.26
11.25	89	0.376±0.008	0.27	0.39	83	0.379±0.008	0.29	0.39	6	-	-	-

Table B.1: Stellar mass-metallicity relation for all the galaxies regardless of their SFH type (left multi-column), galaxies with ST-SFH (centre multi-column), and galaxies with LT-SFH (right multi-column) in voids (a), filaments & walls (b), and clusters (c). The stellar mas-metallicity relation is derived as the 50^{th} percentile (p_{50}) of the distribution, together with the error of the mean, inside each stellar mass bin. The 16^{th} (p_{16}) and 84^{th} (p_{84}) percentiles represent the dispersion of the stellar mass-metallicity relation. The number of galaxies (n) inside each stellar mas bin is also reported.

	Δ[M/H]$_{\rm M}$					
	All		ST-SFH		LT-SFH	
$\log_{10} M_\star$[M$_\odot$]	Δp_{50}	σ	Δp_{50}	σ	Δp_{50}	σ
(a) Filaments & walls - Voids						
8.25	-	-	-	-	-	-
8.75	0.04±0.04	1.0	-	-	0.01±0.04	0.2
9.25	0.108±0.019	5.7	-0.00±0.04	-0.0	0.104±0.021	5.0
9.75	0.04±0.01	4.0	-0.004±0.017	-0.2	0.029±0.013	2.2
10.25	0.031±0.009	3.4	0.035±0.011	3.2	0.016±0.015	1.1
10.75	0.015±0.013	1.2	-0.003±0.014	-0.2	0.06±0.03	2.0
11.25	-	-	-	-	-	-
(b) Clusters - Voids						
8.25	-	-	-	-	-	-
8.75	0.23±0.05	4.6	-	-	0.20±0.05	4.0
9.25	0.40±0.02	20.0	0.11±0.04	2.8	0.419±0.024	17.5
9.75	0.19±0.01	19.0	0.063±0.017	3.7	0.295±0.014	21.1
10.25	0.148±0.009	16.4	0.152±0.011	13.8	0.161±0.015	10.7
10.75	0.084±0.013	6.5	0.040±0.014	2.9	0.11±0.03	3.7
11.25	-	-	-	-	-	-

Table B.2: Differences of stellar mass-metallicity relation between galaxies in filaments & walls and voids (a), and between galaxies in clusters and voids (b) for all the galaxies regardless of their SFH type (left multi-column), galaxies with ST-SFH (centre multi-column), and galaxies with LT-SFH (right multi-column). Δp_{50} represents the difference (together with its error) of the 50^{th} percentile of the stellar mass-metallicity distribution between different large-scale environments, and σ is the ratio between the nominal value and the error or the difference.

	[M/H]$_{\rm M}$							
	Elliptical				Spiral			
$\log_{10} M_\star$[M$_\odot$]	n	p_{50}	p_{16}	p_{84}	n	p_{50}	p_{16}	p_{84}
(a) Voids								
8.25	0	-	-	-	3	-	-	-
8.75	3	-	-	-	45	-0.72±0.04	-1.10	-0.26
9.25	21	-0.41±0.04	-1.02	-0.19	111	-0.610±0.022	-1.01	-0.21
9.75	95	-0.151±0.015	-0.35	0.04	189	-0.399±0.014	-0.75	0.01
10.25	119	0.108±0.011	-0.12	0.28	135	-0.048±0.015	-0.31	0.12
10.75	37	0.305±0.015	0.14	0.37	32	0.071±0.024	-0.14	0.27
11.25	1	-	-	-	2	-	-	-
(b) Filaments & walls								
8.25	1	-	-	-	9	-	-	-
8.75	13	-0.55±0.06	-0.87	-0.29	95	-0.833±0.024	-1.20	-0.51
9.25	78	-0.357±0.02	-0.68	-0.06	383	-0.571±0.012	-1.02	-0.17
9.75	475	-0.094±0.006	-0.36	0.10	683	-0.328±0.008	-0.79	-0.04
10.25	719	0.110±0.004	-0.10	0.27	839	-0.057±0.006	-0.36	0.13
10.75	641	0.291±0.004	0.13	0.38	504	0.113±0.006	-0.10	0.27
11.25	80	0.34±0.01	0.24	0.39	29	0.224±0.022	0.07	0.36
(c) Clusters								
8.25	0	-	-	-	2	-	-	-
8.75	8	-	-	-	31	-0.55±0.04	-1.04	-0.19
9.25	113	-0.145±0.011	-0.33	0.08	126	-0.345±0.018	-0.85	-0.07
9.75	525	-0.006±0.005	-0.21	0.18	304	-0.144±0.009	-0.46	0.06
10.25	766	0.184±0.004	0.02	0.31	314	0.028±0.008	-0.23	0.20
10.75	360	0.307±0.004	0.19	0.38	170	0.197±0.009	-0.01	0.33
11.25	39	0.376±0.013	0.29	0.39	12	0.27±0.03	0.21	0.38

Table B.3: Same as Table B.1 but for elliptical (left multi-column) and spiral galaxies (right multi-column).

	Δ[M/H]$_{\rm M}$			
	Elliptical		Spiral	
$\log_{10} M_\star$[M$_\odot$]	Δp_{50}	σ	Δp_{50}	σ
(a) Filaments & walls - Voids				
8.25	-	-	-	-
8.75	-	-	-0.11±0.04	-2.8
9.25	0.05±0.05	1.0	0.039±0.024	1.6
9.75	0.057±0.017	3.4	0.071±0.016	4.4
10.25	0.002±0.012	0.2	-0.009±0.016	-0.6
10.75	-0.014±0.016	-0.9	0.04±0.03	1.3
11.25	-	-	-	-
(b) Clusters - Voids				
8.25	-	-	-	-
8.75	-	-	0.17±0.05	3.4
9.25	0.26±0.04	6.5	0.27±0.03	9.0
9.75	0.145±0.016	9.1	0.255±0.017	15.0
10.25	0.075±0.012	6.2	0.077±0.017	4.5
10.75	0.003±0.016	0.2	0.13±0.03	4.3
11.25	-	-	-	-

Table B.4: Same as Table B.2 but for elliptical (left multi-column) and spiral galaxies (right multi-column).

	[M/H]$_{\rm M}$							
	Red ($g-r>0.7$)				Blue ($g-r\leq 0.7$)			
$\log_{10} M_\star$[M$_\odot$]	n	p_{50}	p_{16}	p_{84}	n	p_{50}	p_{16}	p_{84}
(a) Voids								
8.25	0	-	-	-	4	-	-	-
8.75	0	-	-	-	56	-0.77±0.03	-1.12	-0.36
9.25	4	-	-	-	155	-0.648±0.018	-1.01	-0.22
9.75	83	-0.101±0.015	-0.25	0.08	280	-0.361±0.011	-0.73	-0.01
10.25	185	0.075±0.01	-0.16	0.24	124	-0.074±0.016	-0.45	0.12
10.75	84	0.230±0.013	-0.03	0.36	7	-	-	-
11.25	4	-	-	-	0	-	-	-
(b) Filaments & walls								
8.25	2	-	-	-	16	-0.95±0.06	-1.27	-0.47
8.75	5	-	-	-	155	-0.746±0.019	-1.17	-0.38
9.25	35	-0.216±0.021	-0.36	-0.02	614	-0.557±0.009	-1.02	-0.16
9.75	538	-0.057±0.005	-0.23	0.11	1062	-0.351±0.006	-0.79	-0.06
10.25	1391	0.090±0.003	-0.13	0.26	825	-0.086±0.006	-0.42	0.12
10.75	1407	0.250±0.003	0.03	0.37	186	0.057±0.011	-0.17	0.20
11.25	213	0.347±0.007	0.22	0.39	0	-	-	-
(c) Clusters								
8.25	0	-	-	-	2	-	-	-
8.75	4	-	-	-	37	-0.62±0.04	-1.02	-0.17
9.25	87	-0.103±0.012	-0.27	0.12	178	-0.333±0.014	-0.82	-0.05
9.75	694	0.002±0.004	-0.18	0.18	278	-0.21±0.01	-0.57	0.01
10.25	1139	0.164±0.003	-0.02	0.30	143	-0.056±0.014	-0.35	0.14
10.75	684	0.296±0.004	0.13	0.38	22	0.16±0.03	-0.06	0.25
11.25	89	0.376±0.008	0.27	0.39	0	-	-	-

Table B.5: Same as Table B.1 but for red (left multi-column) and blue galaxies (right multi-column).

	Δ[M/H]$_{\rm M}$			
	Red ($g-r>0.7$)		Blue ($g-r\leq 0.7$)	
$\log_{10} M_\star$[M$_\odot$]	Δp_{50}	σ	Δp_{50}	σ
(a) Filaments & walls - Voids				
8.25	-	-	-	-
8.75	-	-	0.03±0.04	0.8
9.25	-	-	0.091±0.020	4.5
9.75	0.044±0.016	2.8	0.010±0.013	0.8
10.25	0.02±0.01	2.0	-0.012±0.017	-0.7
10.75	0.021±0.013	1.6	-	-
11.25	-	-	-	-
(b) Clusters - Voids				
8.25	-	-	-	-
8.75	-	-	0.15±0.05	3.0
9.25	-	-	0.315±0.023	13.7
9.75	0.103±0.016	6.4	0.150±0.015	10.0
10.25	0.09±0.01	9.0	0.018±0.021	0.9
10.75	0.066±0.013	5.1	-	-
11.25	-	-	-	-

Table B.6: Same as Table B.2 but for red (left multi-column) and blue galaxies (right multi-column).

	[M/H]$_M$											
	All				ST-SFH				LT-SFH			
$\log_{10} M_\star[M_\odot]$	n	p_{50}	p_{16}	p_{84}	n	p_{50}	p_{16}	p_{84}	n	p_{50}	p_{16}	p_{84}
(a) Voids												
8.75	56	-0.77±0.03	-1.12	-0.36	8	-	-	-	48	-0.88±0.04	-1.18	-0.48
9.25	159	-0.627±0.017	-1.01	-0.20	40	-0.25±0.04	-0.42	-0.07	119	-0.752±0.019	-1.06	-0.28
9.75	363	-0.247±0.009	-0.70	0.01	127	-0.076±0.016	-0.34	0.08	236	-0.403±0.012	-0.77	-0.05
10.25	309	-0.000±0.009	-0.29	0.21	187	0.038±0.011	-0.16	0.24	122	-0.072±0.014	-0.49	0.16
10.75	91	0.208±0.012	-0.07	0.36	68	0.279±0.013	0.06	0.37	23	0.05±0.03	-0.20	0.14
(b) Filaments & walls												
8.75	105	-0.732±0.023	-1.16	-0.36	24	-0.57±0.05	-0.77	-0.08	81	-0.79±0.03	-1.20	-0.43
9.25	326	-0.516±0.012	-1.02	-0.12	80	-0.250±0.023	-0.56	0.03	246	-0.641±0.014	-1.10	-0.21
9.75	1500	-0.210±0.005	-0.66	0.04	602	-0.080±0.007	-0.27	0.11	898	-0.376±0.006	-0.81	-0.05
10.25	2199	0.030±0.003	-0.25	0.22	1263	0.071±0.004	-0.13	0.26	936	-0.056±0.005	-0.42	0.15
10.75	670	0.198±0.005	-0.02	0.35	476	0.253±0.005	0.05	0.37	194	0.100±0.01	-0.12	0.22
(c) Clusters												
8.75	30	-0.62±0.04	-1.04	-0.13	9	-	-	-	21	-0.77±0.05	-1.11	-0.43
9.25	100	-0.270±0.016	-0.78	-0.04	39	-0.210±0.02	-0.38	-0.04	61	-0.324±0.022	-0.94	-0.04
9.75	855	-0.055±0.004	-0.27	0.16	463	-0.012±0.006	-0.20	0.19	392	-0.110±0.007	-0.42	0.09
10.25	1212	0.151±0.003	-0.06	0.29	820	0.195±0.004	-0.02	0.33	392	0.090±0.006	-0.15	0.21
10.75	373	0.277±0.005	0.12	0.38	282	0.313±0.005	0.16	0.39	91	0.161±0.012	-0.01	0.25

Table B.7: Same as Table B.1 but for sub-samples with the same stellar mass distribution.

$\Delta[\mathrm{M/H}]_{\mathrm{M}}$

	All		ST-SFH		LT-SFH	
$\log_{10} M_\star[\mathrm{M}_\odot]$	Δp_{50}	σ	Δp_{50}	σ	Δp_{50}	σ
(a) Filaments & walls - Voids						
8.75	0.04±0.04	1.0	-	-	0.08±0.04	2.0
9.25	0.111±0.021	5.3	0.00±0.05	0.0	0.111±0.024	4.6
9.75	0.038±0.011	3.5	-0.004±0.017	-0.2	0.027±0.013	2.1
10.25	0.030±0.009	3.3	0.033±0.011	3.0	0.016±0.015	1.1
10.75	-0.009±0.013	-0.7	-0.026±0.014	-1.9	0.05±0.03	1.7
(b) Clusters - Voids						
8.75	0.15±0.05	3.0	-	-	0.11±0.06	1.8
9.25	0.357±0.023	15.5	0.04±0.04	1.0	0.43±0.03	14.3
9.75	0.19±0.01	19.0	0.063±0.017	3.7	0.293±0.014	20.9
10.25	0.152±0.009	16.9	0.157±0.011	14.3	0.161±0.015	10.7
10.75	0.069±0.013	5.3	0.034±0.014	2.4	0.11±0.03	3.7

Table B.8: Same as Table B.2 but for sub-samples with the same stellar mass distribution.

$[\mathrm{M/H}]_{\mathrm{M}}$

	Elliptical				Spiral			
$\log_{10} M_\star[\mathrm{M}_\odot]$	n	p_{50}	p_{16}	p_{84}	n	p_{50}	p_{16}	p_{84}
(a) Voids								
8.75	3	-	-	-	45	-0.72±0.04	-1.10	-0.26
9.25	21	-0.41±0.04	-1.02	-0.19	111	-0.610±0.022	-1.01	-0.21
9.75	95	-0.151±0.015	-0.35	0.04	189	-0.399±0.014	-0.75	0.01
10.25	119	0.108±0.011	-0.12	0.28	135	-0.048±0.015	-0.31	0.12
10.75	37	0.305±0.015	0.14	0.37	32	0.071±0.024	-0.14	0.27
(b) Filaments & walls								
8.75	9	-	-	-	61	-0.81±0.03	-1.21	-0.60
9.25	39	-0.35±0.03	-0.64	-0.05	197	-0.517±0.016	-1.01	-0.12
9.75	448	-0.093±0.007	-0.36	0.10	637	-0.331±0.008	-0.78	-0.03
10.25	713	0.109±0.004	-0.10	0.27	833	-0.057±0.006	-0.36	0.13
10.75	251	0.276±0.006	0.12	0.37	233	0.069±0.009	-0.13	0.23
(c) Clusters								
8.75	5	-	-	-	24	-0.77±0.05	-1.08	-0.19
9.25	42	-0.176±0.017	-0.32	0.06	48	-0.42±0.03	-0.94	-0.15
9.75	464	-0.007±0.005	-0.21	0.18	265	-0.160±0.01	-0.47	0.05
10.25	726	0.191±0.004	0.02	0.31	295	0.029±0.008	-0.22	0.21
10.75	191	0.299±0.006	0.17	0.39	95	0.176±0.012	-0.03	0.35

Table B.9: Same as Table B.3 but for sub-samples with the same stellar mass distribution.

$\Delta[\mathrm{M/H}]_{\mathrm{M}}$

	Elliptical		Spiral	
$\log_{10} M_\star[\mathrm{M}_\odot]$	Δp_{50}	σ	Δp_{50}	σ
(a) Filaments & walls - Voids				
8.75	-	-	-0.09±0.05	-1.8
9.25	0.05±0.05	1.0	0.09±0.03	3.0
9.75	0.058±0.017	3.4	0.068±0.016	4.2
10.25	0.001±0.012	0.1	-0.009±0.016	-0.6
10.75	-0.028±0.016	-1.8	-0.00±0.03	-0.0
(b) Clusters - Voids				
8.75	-	-	-0.05±0.06	-0.8
9.25	0.23±0.04	5.8	0.19±0.03	6.3
9.75	0.145±0.016	9.1	0.239±0.017	14.1
10.25	0.083±0.012	6.9	0.077±0.017	4.5
10.75	-0.005±0.016	-0.3	0.10±0.03	3.3

Table B.10: Same as Table B.4 but for sub-samples with the same stellar mass distribution.

	$[M/H]_M$							
	Red ($g-r>0.7$)				Blue ($g-r\leq 0.7$)			
$\log_{10} M_\star[M_\odot]$	n	p_{50}	p_{16}	p_{84}	n	p_{50}	p_{16}	p_{84}
(a) Voids								
8.75	0	-	-	-	56	-0.77±0.03	-1.12	-0.36
9.25	4	-	-	-	155	-0.648±0.018	-1.01	-0.22
9.75	83	-0.101±0.015	-0.25	0.08	280	-0.361±0.011	-0.73	-0.01
10.25	185	0.075±0.01	-0.16	0.24	124	-0.074±0.016	-0.45	0.12
10.75	84	0.230±0.013	-0.03	0.36	7	-	-	-
(b) Filaments & walls								
8.75	3	-	-	-	102	-0.735±0.023	-1.17	-0.41
9.25	16	-0.21±0.03	-0.36	-0.04	310	-0.550±0.013	-1.03	-0.13
9.75	499	-0.058±0.006	-0.23	0.11	1001	-0.356±0.006	-0.78	-0.05
10.25	1379	0.089±0.003	-0.13	0.26	820	-0.087±0.006	-0.43	0.12
10.75	577	0.221±0.005	0.00	0.36	93	0.068±0.015	-0.11	0.19
(c) Clusters								
8.75	2	-	-	-	28	-0.63±0.04	-1.06	-0.16
9.25	34	-0.085±0.018	-0.22	0.12	66	-0.367±0.022	-0.95	-0.16
9.75	605	0.001±0.005	-0.19	0.18	250	-0.209±0.011	-0.58	0.02
10.25	1076	0.167±0.003	-0.01	0.30	136	-0.054±0.015	-0.35	0.16
10.75	358	0.281±0.005	0.13	0.38	15	0.14±0.04	-0.02	0.25

Table B.11: Same as Table B.5 but for sub-samples with the same stellar mass distribution.

	$\Delta[M/H]_M$			
	Red ($g-r>0.7$)		Blue ($g-r\leq 0.7$)	
$\log_{10} M_\star[M_\odot]$	Δp_{50}	σ	Δp_{50}	σ
(a) Filaments & walls - Voids				
8.75	-	-	0.04+/-0.04	1.0
9.25	-	-	0.098+/-0.022	4.5
9.75	0.042+/-0.016	2.6	0.005+/-0.013	0.4
10.25	0.01+/-0.01	1.0	-0.013+/-0.017	-0.8
10.75	-0.009+/-0.013	-0.7	-	-
(b) Clusters - Voids				
8.75	-	-	0.15+/-0.05	3.0
9.25	-	-	0.28+/-0.03	9.3
9.75	0.102+/-0.016	6.4	0.151+/-0.016	9.4
10.25	0.09+/-0.01	9.0	0.020+/-0.021	1.0
10.75	0.051+/-0.014	3.6	-	-

Table B.12: Same as Table B.6 but for sub-samples with the same stellar mass distribution.

	[M/H]$_M$						
	Red ($g-r>0.6$)				Blue ($g-r\leq 0.6$)		
$\log_{10} M_\star$[M$_\odot$]	n	p_{50}	p_{16}	p_{84}	n	p_{50}	p_{16}	p_{84}
(a) Voids								
8.25	0	-	-	-	4	-	-	-
8.75	1	-	-	-	55	-0.78±0.03	-1.13	-0.37
9.25	9	-	-	-	150	-0.652±0.018	-1.01	-0.22
9.75	151	-0.151±0.012	-0.39	0.05	212	-0.429±0.014	-0.77	-0.02
10.25	262	0.027±0.009	-0.25	0.23	47	-0.13±0.03	-0.55	0.06
10.75	89	0.210±0.012	-0.04	0.36	2	-	-	-
11.25	4	-	-	-	0	-	-	-
(b) Filaments & walls								
8.25	2	-	-	-	16	-0.95±0.06	-1.27	-0.47
8.75	9	-	-	-	151	-0.773±0.019	-1.17	-0.38
9.25	82	-0.216±0.016	-0.38	-0.02	567	-0.608±0.009	-1.03	-0.20
9.75	832	-0.100±0.005	-0.33	0.09	768	-0.427±0.008	-0.85	-0.08
10.25	1820	0.057±0.003	-0.18	0.24	396	-0.137±0.009	-0.51	0.10
10.75	1568	0.225±0.003	0.01	0.37	25	0.04±0.03	-0.37	0.14
11.25	213	0.347±0.007	0.22	0.39	0	-	-	-
(c) Clusters								
8.25	0	-	-	-	2	-	-	-
8.75	11	-0.19±0.04	-0.35	-0.06	30	-0.74±0.04	-1.04	-0.26
9.25	166	-0.157±0.01	-0.33	0.03	99	-0.534±0.023	-1.00	-0.14
9.75	843	-0.026±0.004	-0.22	0.17	129	-0.343±0.017	-0.75	-0.04
10.25	1235	0.154±0.003	-0.04	0.30	47	-0.15±0.03	-0.48	0.05
10.75	703	0.292±0.004	0.13	0.38	3	-	-	-
11.25	89	0.376±0.008	0.27	0.39	0	-	-	-

Table B.13: Same as Table B.5 but for the colour classification criterion at 0.6 instead of 0.7.

	Δ[M/H]$_M$			
	Red (>0.6)		Blue (≤ 0.6)	
$\log_{10} M_\star$[M$_\odot$]	Δp_{50}	σ	Δp_{50}	σ
(a) Filaments & walls - Voids				
8.25	-	-	-	-
8.75	-	-	0.03±0.05	0.6
9.25	-	-	0.12±0.03	4.0
9.75	0.125±0.013	9.6	0.086±0.022	3.9
10.25	0.127±0.009	14.1	-0.01±0.04	-0.2
10.75	0.082±0.013	6.3	-	-
11.25	-	-	-	-
(b) Clusters - Voids				
8.25	-	-	-	-
8.75	-	-	0.15±0.05	3.0
9.25	-	-	0.315±0.023	13.7
9.75	0.103±0.016	6.4	0.150±0.015	10.0
10.25	0.09±0.01	9.0	0.018±0.021	0.9
10.75	0.066±0.013	5.1	-	-
11.25	-	-	-	-

Table B.14: Same as Table B.6 but for the colour classification criterion at 0.6 instead of 0.7.

	[M/H]$_L$											
	All				ST-SFH				LT-SFH			
$\log_{10} M_\star[M_\odot]$	n	p_{50}	p_{16}	p_{84}	n	p_{50}	p_{16}	p_{84}	n	p_{50}	p_{16}	p_{84}
(a) Voids												
8.25	4	-	-	-	1	-	-	-	3	-	-	-
8.75	56	-0.875±0.02	-1.23	-0.54	8	-	-	-	48	-0.863±0.022	-1.13	-0.54
9.25	159	-0.772±0.012	-1.04	-0.36	40	-0.847±0.022	-1.01	-0.41	119	-0.733±0.014	-1.05	-0.36
9.75	363	-0.354±0.007	-0.70	-0.05	127	-0.309±0.011	-0.71	-0.04	236	-0.387±0.009	-0.69	-0.05
10.25	309	-0.099±0.007	-0.40	0.15	187	-0.082±0.008	-0.36	0.16	122	-0.116±0.011	-0.42	0.14
10.75	91	0.14±0.01	-0.14	0.33	68	0.204±0.011	-0.11	0.35	23	-0.017±0.024	-0.30	0.16
11.25	4	-	-	-	3	-	-	-	1	-	-	-
(b) Filaments & walls												
8.25	18	-0.87±0.03	-1.26	-0.30	3	-	-	-	15	-0.91±0.04	-1.28	-0.81
8.75	160	-0.878±0.012	-1.21	-0.51	40	-0.946±0.02	-1.28	-0.66	120	-0.841±0.014	-1.18	-0.45
9.25	649	-0.656±0.006	-1.03	-0.26	159	-0.761±0.011	-1.05	-0.21	490	-0.635±0.007	-1.01	-0.27
9.75	1600	-0.289±0.003	-0.70	-0.02	643	-0.174±0.005	-0.58	0.02	957	-0.373±0.005	-0.75	-0.07
10.25	2216	-0.068±0.002	-0.40	0.16	1273	-0.043±0.003	-0.36	0.19	943	-0.116±0.004	-0.46	0.14
10.75	1593	0.1644±0.0024	-0.11	0.33	1150	0.210±0.003	-0.07	0.35	443	0.044±0.005	-0.22	0.22
11.25	213	0.316±0.005	0.13	0.38	184	0.337±0.005	0.14	0.38	29	0.221±0.019	-0.02	0.28
(c) Clusters												
8.25	2	-	-	-	0	-	-	-	2	-	-	-
8.75	41	-0.522±0.022	-1.09	-0.14	13	-0.31±0.04	-0.74	-0.12	28	-0.64±0.03	-1.12	-0.17
9.25	265	-0.216±0.008	-0.65	-0.02	113	-0.144±0.012	-0.43	0.00	152	-0.275±0.011	-0.77	-0.04
9.75	972	-0.050±0.004	-0.30	0.11	527	-0.039±0.005	-0.22	0.12	445	-0.070±0.006	-0.41	0.10
10.25	1282	0.105±0.003	-0.12	0.25	861	0.114±0.003	-0.09	0.28	421	0.090±0.005	-0.21	0.21
10.75	706	0.248±0.003	0.05	0.35	542	0.276±0.003	0.10	0.36	164	0.148±0.008	-0.05	0.26
11.25	89	0.347±0.007	0.18	0.38	83	0.354±0.007	0.22	0.38	6	-	-	-

Table B.15: Same as Table B.1 but for the stellar metallicity calculated as the luminosity-weighted average.

Δ[M/H]$_{\rm L}$

$\log_{10} M_\star$[M$_\odot$]	All Δp_{50}	All σ	ST-SFH Δp_{50}	ST-SFH σ	LT-SFH Δp_{50}	LT-SFH σ
(a) Filaments & walls - Voids						
8.25	-	-	-	-	-	-
8.75	-0.002±0.023	-0.1	-	-	0.02±0.03	0.7
9.25	0.115±0.013	8.8	0.086±0.024	3.6	0.098±0.015	6.5
9.75	0.066±0.008	8.2	0.135±0.012	11.2	0.01±0.01	1.0
10.25	0.031±0.007	4.4	0.039±0.009	4.3	-0.001±0.012	-0.1
10.75	0.027±0.011	2.5	0.007±0.012	0.6	0.06±0.02	3.0
11.25	-	-	-	-	-	-
(b) Clusters - Voids						
8.25	-	-	-	-	-	-
8.75	0.35±0.03	11.7	-	-	0.22±0.03	7.3
9.25	0.555±0.014	39.6	0.70±0.02	35.0	0.458±0.018	25.4
9.75	0.304±0.008	38.0	0.270±0.012	22.5	0.317±0.011	28.8
10.25	0.204±0.007	29.1	0.196±0.009	21.8	0.206±0.012	17.2
10.75	0.111±0.011	10.1	0.072±0.012	6.0	0.16±0.03	5.3
11.25	-	-	-	-	-	-

Table B.16: Same as Table B.2 but for the stellar metallicity calculated as the luminosity-weighted average.

[M/H]$_{\rm L}$

$\log_{10} M_\star$[M$_\odot$]	Elliptical n	Elliptical p_{50}	Elliptical p_{16}	Elliptical p_{84}	Spiral n	Spiral p_{50}	Spiral p_{16}	Spiral p_{84}
(a) Voids								
8.25	0	-	-	-	3	-	-	-
8.75	3	-	-	-	45	-0.865±0.022	-1.23	-0.50
9.25	21	-0.81±0.03	-1.10	-0.16	111	-0.731±0.015	-0.99	-0.36
9.75	95	-0.130±0.012	-0.44	0.02	189	-0.48±0.01	-0.72	-0.18
10.25	119	0.057±0.009	-0.18	0.24	135	-0.215±0.011	-0.42	-0.03
10.75	37	0.243±0.013	0.10	0.36	32	-0.032±0.021	-0.22	0.16
11.25	1	-	-	-	2	-	-	-
(b) Filaments & walls								
8.25	1	-	-	-	9	-	-	-
8.75	13	-0.68±0.04	-1.24	-0.15	95	-0.889±0.016	-1.22	-0.52
9.25	78	-0.383±0.015	-1.02	-0.15	383	-0.678±0.008	-1.03	-0.30
9.75	475	-0.113±0.006	-0.45	0.06	683	-0.435±0.006	-0.80	-0.15
10.25	719	0.078±0.004	-0.13	0.23	839	-0.223±0.004	-0.53	-0.00
10.75	641	0.252±0.003	0.07	0.35	504	-0.007±0.005	-0.25	0.20
11.25	80	0.319±0.008	0.17	0.38	29	0.130±0.018	-0.04	0.30
(c) Clusters								
8.25	0	-	-	-	2	-	-	-
8.75	8	-	-	-	31	-0.57±0.03	-1.10	-0.17
9.25	113	-0.096±0.012	-0.27	0.05	126	-0.442±0.013	-0.88	-0.11
9.75	525	-0.020±0.005	-0.17	0.13	304	-0.170±0.007	-0.54	0.05
10.25	766	0.143±0.003	0.01	0.27	314	-0.047±0.007	-0.38	0.14
10.75	360	0.273±0.004	0.16	0.35	170	0.104±0.007	-0.11	0.28
11.25	39	0.347±0.011	0.14	0.38	12	0.227±0.021	0.12	0.35

Table B.17: Same as Table B.3 but for the stellar metallicity calculated as the luminosity-weighted average.

	Δ[M/H]$_L$			
	Elliptical		Spiral	
$\log_{10} M_\star$[M$_\odot$]	Δp_{50}	σ	Δp_{50}	σ
(a) Filaments & walls - Voids				
8.25	-	-	-	-
8.75	-	-	-0.02±0.03	-0.7
9.25	0.42±0.03	14.0	0.052±0.017	3.1
9.75	0.017±0.014	1.2	0.045±0.012	3.8
10.25	0.02±0.01	2.0	-0.009±0.012	-0.7
10.75	0.009±0.014	0.6	0.026±0.021	1.2
11.25	-	-	-	-
(b) Clusters - Voids				
8.25	-	-	-	-
8.75	-	-	0.29±0.03	9.7
9.25	0.71±0.03	23.7	0.289±0.019	15.2
9.75	0.110±0.013	8.5	0.309±0.013	23.8
10.25	0.086±0.01	8.6	0.168±0.013	12.9
10.75	0.030±0.014	2.1	0.136±0.022	6.2
11.25	-	-	-	-

Table B.18: Same as Table B.4 but for the stellar metallicity calculated as the luminosity-weighted average.

	[M/H]$_L$							
	Red ($g-r>0.7$)				Blue ($g-r\leq 0.7$)			
$\log_{10} M_\star$[M$_\odot$]	n	p_{50}	p_{16}	p_{84}	n	p_{50}	p_{16}	p_{84}
(a) Voids								
8.25	0	-	-	-	4	-	-	-
8.75	0	-	-	-	56	-0.875±0.02	-1.23	-0.54
9.25	4	-	-	-	155	-0.779±0.012	-1.04	-0.38
9.75	83	-0.109±0.013	-0.31	0.03	280	-0.472±0.008	-0.73	-0.15
10.25	185	0.032±0.008	-0.23	0.22	124	-0.257±0.011	-0.46	-0.07
10.75	84	0.169±0.011	-0.11	0.34	7	-	-	-
11.25	4	-	-	-	0	-	-	-
(b) Filaments & walls								
8.25	2	-	-	-	16	-0.90±0.04	-1.27	-0.58
8.75	5	-	-	-	155	-0.888±0.012	-1.21	-0.52
9.25	35	-0.179±0.022	-0.32	-0.09	614	-0.667±0.006	-1.04	-0.29
9.75	538	-0.071±0.005	-0.22	0.08	1062	-0.445±0.004	-0.80	-0.16
10.25	1391	0.048±0.003	-0.20	0.22	825	-0.283±0.005	-0.60	-0.06
10.75	1407	0.1938±0.0024	-0.05	0.34	186	-0.148±0.009	-0.41	0.03
11.25	213	0.316±0.005	0.13	0.38	0	-	-	-
(c) Clusters								
8.25	0	-	-	-	2	-	-	-
8.75	4	-	-	-	37	-0.573±0.022	-1.10	-0.17
9.25	87	-0.074±0.013	-0.22	0.08	178	-0.366±0.011	-0.83	-0.09
9.75	694	-0.010±0.004	-0.16	0.14	278	-0.263±0.008	-0.65	-0.02
10.25	1139	0.125±0.003	-0.05	0.26	143	-0.262±0.011	-0.58	0.03
10.75	684	0.253±0.003	0.06	0.35	22	-0.022±0.023	-0.27	0.08
11.25	89	0.347±0.007	0.18	0.38	0	-	-	-

Table B.19: Same as Table B.5 but for the stellar metallicity calculated as the luminosity-weighted average.

	$\Delta[\mathrm{M/H}]_{\mathrm{L}}$			
	Red ($g-r>0.7$)		Blue ($g-r\leq 0.7$)	
$\log_{10} M_\star[\mathrm{M}_\odot]$	Δp_{50}	σ	Δp_{50}	σ
(a) Filaments & walls - Voids				
8.25	-	-	-	-
8.75	-	-	-0.012±0.023	-0.5
9.25	-	-	0.112±0.013	8.6
9.75	0.038±0.014	2.7	0.028±0.009	3.1
10.25	0.016±0.009	1.8	-0.026±0.012	-2.2
10.75	0.025±0.011	2.3	-	-
11.25	-	-	-	-
(b) Clusters - Voids				
8.25	-	-	-	-
8.75	-	-	0.30±0.03	10.0
9.25	-	-	0.414±0.016	25.9
9.75	0.099±0.014	7.1	0.209±0.012	17.4
10.25	0.093±0.009	10.3	-0.006±0.016	-0.4
10.75	0.084±0.011	7.6	-	-
11.25	-	-	-	-

Table B.20: Same as Table B.6 but for the stellar metallicity calculated as the luminosity-weighted average.

List of Acronyms

ΛCMD Λ Cold Dark Matter. 39

BAO Baryon Acoustic Oscillations. 42

BH Black Hole. 28

CAHA Centro Astronómico Hispano en Andalucía. 48

CALIFA Calar Alto Legacy Integral Field Area. 52

CAVITY Calar Alto Void Integral-field Treasury surveY. 48

CCS Complete Control Sample. 56

CMBR Cosmic Microwave Background Radiation. 38

CMD Colour Magnitude Diagram. 29

CO-CS CO Control Sample. 56

DTFE Delaunay Tessellation Field Estimator. 53

E-MILES Extended Medium resolution INT Library of Empirical Spectra. 98

FWHM Full Width at Half Maximum. 88

GBT Green Bank Telescope. 48

HOD Halo Occupation Distribution. 118

HR Hertzsprung-Russel. 34

ICM IntraCluster Medium. 44

IFU Integral Field Unit. 48

IMF Initial Mass Function. 36

INT Isaac Newton Telescope. 48

IRAM Institut de Radioastronomie Millimétrique. 48

ISM Interstellar Medium. 26

KS Kolmogorov–Smirnov. 60

LOSVD Line-Of-Sight Velocity Distribution. 98

LT-SFH Long-Timescale SFH. 109

MIR Mid-InfraRed. 92

MPA-JHU Max-Planck-Institut für Astrophysik and Johns Hopkins University. 54

MS Main Sequence. 34

MW Milky Way. 26

MZ$_\star$R stellar mass-metallicity relation. 124

MZ$_{\rm g}$R gas-phase mass-metallicity relation. 46

NUV Near-UltraViolet. 92

pPXF Penalized Pixel-Fitting. 98

s.e.m. standard error of the mean. 109

S/N Signal-to-Noise ratio. 53

SDSS Sloan Digital Sky Survey. 43

SF Star-Forming. 75

SFE = **SFR**/$M_{\mathrm{H_2}}$ Star Formation Efficiency. 45

SFH Star Formation History. 47

SFMS Star-Forming Main Sequence. 30

SFR Star Formation Rate. 29

SNIa SuperNova type Ia. 36

sSFR = **SFR**/$M_\star$ specific Star Formation Rate. 64

SSP Single-age Single-metallicity stellar Population. 99

ST-SFH Short-Timescale SFH. 109

STECKMAP STEllar Content and Kinematics from high resolution galactic spectra via Maximum A Posteriori. 98

VGS Void Galaxy Survey. 52

WSRT Westerbork Synthesis Radio Telescope. 53

WVF Watershed Void Finder. 43

xGASS extended GALEX Arecibo SDSS Survey. 52

Bibliography

Abazajian, K. N., Adelman-McCarthy, J. K., Agüeros, M. A., et al. 2009, ApJS, 182, 543

Abell, G. O., Corwin, Harold G., J., & Olowin, R. P. 1989, ApJS, 70, 1

Accurso, G., Saintonge, A., Catinella, B., et al. 2017, MNRAS, 470, 4750

Ahumada, R., Prieto, C. A., Almeida, A., et al. 2020, ApJS, 249, 3

Alfaro, I. G., Rodriguez, F., Ruiz, A. N., & Lambas, D. G. 2020, A&A, 638, A60

Alpaslan, M., Robotham, A. S. G., Obreschkow, D., et al. 2014, MNRAS, 440, L106

Amiri, A., Tavasoli, S., & De Zotti, G. 2019, ApJ, 874, 140

Aragon-Calvo, M. A. & Szalay, A. S. 2013, MNRAS, 428, 3409

Argudo-Fernández, M., Lacerna, I., & Duarte Puertas, S. 2018, A&A, 620, A113

Argudo-Fernández, M., Verley, S., Bergond, G., et al. 2015, A&A, 578, A110

Artale, M. C., Zehavi, I., Contreras, S., & Norberg, P. 2018, MNRAS, 480, 3978

Bennett, C. L., Halpern, M., Hinshaw, G., et al. 2003, ApJS, 148, 1

Beygu, B., Kreckel, K., van de Weygaert, R., van der Hulst, J. M., & van Gorkom, J. H. 2013, AJ, 145, 120

Beygu, B., Kreckel, K., van der Hulst, J. M., et al. 2016, MNRAS, 458, 394

Bigiel, F., Leroy, A. K., Walter, F., et al. 2011, ApJ, 730, L13

Birkhoff, G. D. 1927, Relativity and Modern Physics

Blakeslee, J. P., Vazdekis, A., & Ajhar, E. A. 2001, MNRAS, 320, 193

Bolatto, A. D., Wolfire, M., & Leroy, A. K. 2013, ARA&A, 51, 207

Bolatto, A. D., Wong, T., Utomo, D., et al. 2017, ApJ, 846, 159

Boselli, A. & Gavazzi, G. 2006, PASP, 118, 517

Brinchmann, J., Charlot, S., White, S. D. M., et al. 2004, MNRAS, 351, 1151

Cappellari, M. 2017, MNRAS, 466, 798

Cappellari, M. 2022, MNRAS submitted

Cappellari, M. & Emsellem, E. 2004, PASP, 116, 138

Castignani, G., Combes, F., Jablonka, P., et al. 2021, arXiv e-prints, arXiv:2101.04389

Catalán-Torrecilla, C., Gil de Paz, A., Castillo-Morales, A., et al. 2015, A&A, 584, A87

Catinella, B., Saintonge, A., Janowiecki, S., et al. 2018, MNRAS, 476, 875

Ceccarelli, L., Duplancic, F., & Garcia Lambas, D. 2022, MNRAS, 509, 1805

Cen, R. 2011, ApJ, 741, 99

Chabrier, G. 2003, PASP, 115, 763

Chung, J., Kim, S., Rey, S.-C., & Lee, Y. 2021, arXiv e-prints, arXiv:2110.07836

Cimatti, A., Fraternali, F., & Nipoti, C. 2020, Introduction to galaxy formation and evolution: from primordial gas to present-day galaxies

Cole, S., Percival, W. J., Peacock, J. A., et al. 2005, MNRAS, 362, 505

Colless, M., Dalton, G., Maddox, S., et al. 2001, MNRAS, 328, 1039

Combes, F., Boisse, P., Mazure, A., Blanchard, A., & Seymour, M. 2002, Galaxies and cosmology

Constantin, A., Hoyle, F., & Vogeley, M. S. 2008, ApJ, 673, 715

Cortese, L., Bekki, K., Boselli, A., et al. 2016, MNRAS, 459, 3574

Courtois, H. M., van de Weygaert, R., Aubert, M., et al. 2023, A&A, 673, A38

Das, M., Saito, T., Iono, D., Honey, M., & Ramya, S. 2015, ApJ, 815, 40

De Rossi, M. E., Bower, R. G., Font, A. S., Schaye, J., & Theuns, T. 2017, MNRAS, 472, 3354

den Brok, J. S., Chatzigiannakis, D., Bigiel, F., et al. 2021, MNRAS, 504, 3221

Deng, X.-F. 2011, AJ, 141, 162

Domínguez-Gómez, J., Lisenfeld, U., Pérez, I., et al. 2022, A&A, 658, A124

Domínguez-Gómez, J., Lisenfeld, U., Pérez, I., et al. 2023, A&A, 670, C3

Domínguez Sánchez, H., Huertas-Company, M., Bernardi, M., Tuccillo, D., & Fischer, J. L. 2018, MNRAS, 476, 3661

Doroshkevich, A. G., Zeldovich, Y. B., Syunyaev, R. A., & Khlopov, M. Y. 1980, Pisma v Astronomicheskii Zhurnal, 6, 457

Dreyer, J. L. E. 1888, MmRAS, 49, 1

Dreyer, J. L. E. 1895, MmRAS, 51, 185

Dreyer, J. L. E. 1910, MmRAS, 59, 105

Duarte Puertas, S., Vilchez, J. M., Iglesias-Páramo, J., et al. 2017, A&A, 599, A71

Duarte Puertas, S., Vilchez, J. M., Iglesias-Páramo, J., et al. 2022, A&A, 666, A186

Einstein, A. 1915, Sitzungsberichte der Königlich Preussischen Akademie der Wissenschaften, 844

Einstein, A. 1916, Annalen der Physik, 354, 769

Einstein, A. 1917, Sitzungsberichte der Königlich Preussischen Akademie der Wissenschaften, 142

Eisenstein, D. J., Zehavi, I., Hogg, D. W., et al. 2005, ApJ, 633, 560

El-Ad, H. & Piran, T. 1997, ApJ, 491, 421

Falcón-Barroso, J., Sánchez-Blázquez, P., Vazdekis, A., et al. 2011, A&A, 532, A95

Florez, J., Berlind, A. A., Kannappan, S. J., et al. 2021, ApJ, 906, 97

Friedmann, A. 1922, Zeitschrift fur Physik, 10, 377

Friedmann, A. 1924, Zeitschrift fur Physik, 21, 326

Gabàs Masip, J. 2017, RBA, Las galaxias

Galadí-Enríquez, D. 2016, (GE16), RBA, La evolución estelar

Gallazzi, A., Charlot, S., Brinchmann, J., White, S. D. M., & Tremonti, C. A. 2005, MNRAS, 362, 41

Gallazzi, A. R., Pasquali, A., Zibetti, S., & Barbera, F. L. 2021, MNRAS, 502, 4457

Gamow, G. 1970, My world line: An informal autobiography.

García-Benito, R., González Delgado, R. M., Pérez, E., et al. 2019, A&A, 621, A120

Gershtein, S. S. & Zel'dovich, Y. B. 1966, ZhETF Pisma Redaktsiiu, 4, 174

Goldberg, D. M. & Vogeley, M. S. 2004, ApJ, 605, 1

González Delgado, R. M., García-Benito, R., Pérez, E., et al. 2015, A&A, 581, A103

Gould, R. J. & Salpeter, E. E. 1963, ApJ, 138, 393

Grossi, M., Corbelli, E., Bizzocchi, L., et al. 2016, A&A, 590, A27

Habouzit, M., Pisani, A., Goulding, A., et al. 2020, MNRAS, 493, 899

Hao, C.-N., Kennicutt, R. C., Johnson, B. D., et al. 2011, ApJ, 741, 124

Harrison, E. R. 1970, Phys. Rev. D, 1, 2726

Herschel, J. F. W. 1864, Philosophical Transactions of the Royal Society of London Series I, 154, 1

Herschel, W. 1785, Philosophical Transactions of the Royal Society of London Series I, 75, 213

Herschel, W. 1802, Philosophical Transactions of the Royal Society of London Series I, 92, 477

Hoskin, M. A. 1976, Journal for the History of Astronomy, 7, 169

Hoyle, F. & Vogeley, M. S. 2002, ApJ, 566, 641

Hoyle, F., Vogeley, M. S., & Pan, D. 2012, MNRAS, 426, 3041

Hubble, E. 1929, Proceedings of the National Academy of Science, 15, 168

Hubble, E. P. 1926, ApJ, 64, 321

Huchra, J. P., Macri, L. M., Masters, K. L., et al. 2012, ApJS, 199, 26

Huchtmeier, W. K. & Richter, O. G. 1989, A&A, 210, 1

Hunt, L. K., Tortora, C., Ginolfi, M., & Schneider, R. 2020, A&A, 643, A180

Janowiecki, S., Catinella, B., Cortese, L., et al. 2017, MNRAS, 466, 4795

Jeans, J. H. 1902, Philosophical Transactions of the Royal Society of London Series A, 199, 1

Kaplan, E. L. & Meier, P. 1958, Journal of the American Statistical Association, 53, 457

Kauffmann, G., Heckman, T. M., White, S. D. M., et al. 2003, MNRAS, 341, 33

Kenney, J. D. & Young, J. S. 1986, ApJ, 301, L13

Kereš, D., Katz, N., Weinberg, D. H., & Davé, R. 2005, MNRAS, 363, 2

Knop, R. A., Aldering, G., Amanullah, R., et al. 2003, ApJ, 598, 102

Kreckel, K., Croxall, K., Groves, B., van de Weygaert, R., & Pogge, R. W. 2015, ApJ, 798, L15

Kreckel, K., Platen, E., Aragón-Calvo, M. A., et al. 2012, AJ, 144, 16

Kreckel, K., Platen, E., Aragón-Calvo, M. A., et al. 2011, AJ, 141, 4

Kroupa, P. 2001, MNRAS, 322, 231

Lavaux, G. & Wandelt, B. D. 2010, MNRAS, 403, 1392

Leavitt, H. S. & Pickering, E. C. 1912, Harvard College Observatory Circular, 173, 1

Lemaître, G. 1931, MNRAS, 91, 483

Lemaître, G. 1933, Comptes Rendus de L'Academie des Sciences de Paris, 903–904

Leroy, A. K., Walter, F., Bigiel, F., et al. 2009, AJ, 137, 4670

Leroy, A. K., Walter, F., Brinks, E., et al. 2008, AJ, 136, 2782

Lifshitz, E. M. 1946, Zhurnal Eksperimentalnoi i Teoreticheskoi Fiziki, 16, 587

Lisenfeld, U., Espada, D., Verdes-Montenegro, L., et al. 2011, A&A, 534, A102

Lisenfeld, U., Xu, C. K., Gao, Y., et al. 2019, A&A, 627, A107

Longair, M. S. 2023, (L23), Springer, AAL, Galaxy Formation

Lyubimov, V. A., Novikov, E. G., Nozik, V. Z., et al. 1981, Soviet Journal of Experimental and Theoretical Physics, 54, 616

Michell, J. 1767, Philosophical Transactions of the Royal Society of London Series I, 57, 234

Moresco, M., Amati, L., Amendola, L., et al. 2022, Living Reviews in Relativity, 25, 6

Murphy, E. J., Condon, J. J., Schinnerer, E., et al. 2011, ApJ, 737, 67

Novikov, I. 1964, Zhurnal Èksperimental'noi i Teoreticheskoi Fiziki, 46, 686–689

Ocvirk, P., Pichon, C., Lançon, A., & Thiébaut, E. 2006a, MNRAS, 365, 74

Ocvirk, P., Pichon, C., Lançon, A., & Thiébaut, E. 2006b, MNRAS, 365, 46

Pan, D. C., Vogeley, M. S., Hoyle, F., Choi, Y.-Y., & Park, C. 2012, MNRAS, 421, 926

Panter, B., Jimenez, R., Heavens, A. F., & Charlot, S. 2008, MNRAS, 391, 1117

Park, C., Choi, Y.-Y., Vogeley, M. S., et al. 2007, ApJ, 658, 898

Partridge, R. B. 1980a, Phys. Scr, 21, 624

Partridge, R. B. 1980b, ApJ, 235, 681

Pasquali, A., Gallazzi, A., Fontanot, F., et al. 2010, MNRAS, 407, 937

Pasquali, A., Gallazzi, A., & van den Bosch, F. C. 2012, MNRAS, 425, 273

Patiri, S. G., Prada, F., Holtzman, J., Klypin, A., & Betancort-Rijo, J. 2006, MNRAS, 372, 1710

Paturel, G., Fouqué, P., Buta, R., & Garcia, A. M. 1991, A&A, 243, 319

Peebles, P. J. E. 1982, ApJ, 263, L1

Peebles, P. J. E. 2001, ApJ, 557, 495

Penzias, A. A. & Wilson, R. W. 1965, ApJ, 142, 419

Percival, W. J., Baugh, C. M., Bland-Hawthorn, J., et al. 2001, MNRAS, 327, 1297

Pietrinferni, A., Cassisi, S., Salaris, M., & Castelli, F. 2004, ApJ, 612, 168

Pilyugin, L. S., Grebel, E. K., Zinchenko, I. A., Nefedyev, Y. A., & Mattsson, L. 2017, MNRAS, 465, 1358

Pisani, A., Massara, E., Spergel, D. N., et al. 2019, BAAS, 51, 40

Planck Collaboration, Aghanim, N., Akrami, Y., et al. 2020, A&A, 641, A1

Platen, E., van de Weygaert, R., & Jones, B. J. T. 2007, MNRAS, 380, 551

Platen, E., van de Weygaert, R., Jones, B. J. T., Vegter, G., & Calvo, M. A. A. 2011, MNRAS, 416, 2494

Porter, L. E., Holwerda, B. W., Kruk, S., et al. 2023, arXiv e-prints, arXiv:2304.05999

Poulin, V., Smith, T. L., & Karwal, T. 2023, arXiv e-prints, arXiv:2302.09032

Pustilnik, S. A., Tepliakova, A. L., & Kniazev, A. Y. 2011, Astrophysical Bulletin, 66, 255

Pérez Fernández, P. 2017, (PF17), RBA, Las nubes y el polvo cósmico

Rémy-Ruyer, A., Madden, S. C., Galliano, F., et al. 2014, A&A, 563, A31

Rhee, J., Smith, R., Choi, H., et al. 2020, ApJS, 247, 45

Ricciardelli, E., Cava, A., Varela, J., & Quilis, V. 2014, MNRAS, 445, 4045

Ricciardelli, E., Quilis, V., & Planelles, S. 2013, MNRAS, 434, 1192

Rieder, S., van de Weygaert, R., Cautun, M., Beygu, B., & Portegies Zwart, S. 2013, MNRAS, 435, 222

Rojas, R. R., Vogeley, M. S., Hoyle, F., & Brinkmann, J. 2004, ApJ, 617, 50

Rojas, R. R., Vogeley, M. S., Hoyle, F., & Brinkmann, J. 2005, ApJ, 624, 571

Rosas-Guevara, Y., Tissera, P., Lagos, C. d. P., Paillas, E., & Padilla, N. 2022, MNRAS

Rubin, V. C., Ford, W. K., J., & Thonnard, N. 1980, ApJ, 238, 471

Sachs, R. K. & Wolfe, A. M. 1967, ApJ, 147, 73

Sage, L. J., Weistrop, D., Cruzen, S., & Kompe, C. 1997, AJ, 114, 1753

Saintonge, A., Catinella, B., Cortese, L., et al. 2016, MNRAS, 462, 1749

Saintonge, A., Catinella, B., Tacconi, L. J., et al. 2017, ApJS, 233, 22

Saintonge, A., Kauffmann, G., Wang, J., et al. 2011, MNRAS, 415, 61

Salim, S., Lee, J. C., Ly, C., et al. 2014, ApJ, 797, 126

Salim, S., Rich, R. M., Charlot, S., et al. 2007, ApJS, 173, 267

Sánchez, S. F., Kennicutt, R. C., Gil de Paz, A., et al. 2012, A&A, 538, A8

Sánchez-Blázquez, P., Ocvirk, P., Gibson, B. K., Pérez, I., & Peletier, R. F. 2011, MNRAS, 415, 709

Sánchez-Blázquez, P., Peletier, R. F., Jiménez-Vicente, J., et al. 2006, MNRAS, 371, 703

Schaap, W. E. 2007, PhD thesis, Kapteyn Astronomical Institute

Schaap, W. E. & van de Weygaert, R. 2000, A&A, 363, L29

Schneider, P. 2015, Extragalactic Astronomy and Cosmology: An Introduction

Scholz-Díaz, L., Martín-Navarro, I., & Falcón-Barroso, J. 2022, MNRAS, 511, 4900

Scholz-Díaz, L., Martín-Navarro, I., & Falcón-Barroso, J. 2023, MNRAS, 518, 6325

Sheth, R. K. & van de Weygaert, R. 2004, MNRAS, 350, 517

Silk, J. 1968, ApJ, 151, 459

Smith, R. W. & Gingerich, O. 1982, Nature, 298, 776

Smoot, G. F., Bennett, C. L., Kogut, A., et al. 1992, ApJ, 396, L1

Solomon, P. M., Downes, D., Radford, S. J. E., & Barrett, J. W. 1997, ApJ, 478, 144

Springob, C. M., Haynes, M. P., Giovanelli, R., & Kent, B. R. 2005, ApJS, 160, 149

Strauss, M. A., Weinberg, D. H., Lupton, R. H., et al. 2002, AJ, 124, 1810

Szomoru, A., van Gorkom, J. H., Gregg, M. D., & Strauss, M. A. 1996, AJ, 111, 2150

Tantalo, R. & Chiosi, C. 2002, A&A, 388, 396

Tempel, E., Tuvikene, T., Kipper, R., & Libeskind, N. I. 2017, A&A, 602, A100

Theureau, G., Coudreau, N., Hallet, N., et al. 2004, VizieR Online Data Catalog, J/A+A/430/373

Tolman, R. C. 1934, Proceedings of the National Academy of Science, 20, 169

Tonry, J. L., Schmidt, B. P., Barris, B., et al. 2003, ApJ, 594, 1

Torrey, P., Vogelsberger, M., Marinacci, F., et al. 2019, MNRAS, 484, 5587

Tremaine, S. & Gunn, J. E. 1979, Phys. Rev. Lett., 42, 407

Tremonti, C. A., Heckman, T. M., Kauffmann, G., et al. 2004, ApJ, 613, 898

Trimble, V. 1995, PASP, 107, 1133

Trussler, J., Maiolino, R., Maraston, C., et al. 2021, MNRAS, 500, 4469

Vallés-Pérez, D., Quilis, V., & Planelles, S. 2021, ApJ, 920, L2

van de Voort, F., Schaye, J., Booth, C. M., Haas, M. R., & Dalla Vecchia, C. 2011, MNRAS, 414, 2458

van de Weygaert, R. 2016, in The Zeldovich Universe: Genesis and Growth of the Cosmic Web, ed. R. van de Weygaert, S. Shandarin, E. Saar, & J. Einasto, Vol. 308, 493–523

van de Weygaert, R. & Schaap, W. 2009, The Cosmic Web: Geometric Analysis, ed. V. J. Martínez, E. Saar, E. Martínez-González, & M. J. Pons-Bordería, Vol. 665, 291–413

van de Weygaert, R. & van Kampen, E. 1993, MNRAS, 263, 481

van Loon, M. L., Mitchell, P. D., & Schaye, J. 2021, MNRAS, 504, 4817

Varela, J., Betancort-Rijo, J., Trujillo, I., & Ricciardelli, E. 2012, ApJ, 744, 82

Vazdekis, A., Casuso, E., Peletier, R. F., & Beckman, J. E. 1996, ApJS, 106, 307

Vazdekis, A., Coelho, P., Cassisi, S., et al. 2015, MNRAS, 449, 1177

Vazdekis, A., Koleva, M., Ricciardelli, E., Röck, B., & Falcón-Barroso, J. 2016, MNRAS, 463, 3409

Vazdekis, A., Sánchez-Blázquez, P., Falcón-Barroso, J., et al. 2010, MNRAS, 404, 1639

Wegner, G. & Grogin, N. A. 2008, AJ, 136, 1

Wegner, G. A., Salzer, J. J., Taylor, J. M., & Hirschauer, A. S. 2019, ApJ, 883, 29

Wilson, T. L., Rohlfs, K., & Hüttemeister, S. 2013, Tools of Radio Astronomy

Worthey, G. 1994, ApJS, 95, 107

Yang, N., Scholte, D., & Saintonge, A. 2022, arXiv e-prints, arXiv:2212.10657

York, D. G., Adelman, J., Anderson, John E., J., et al. 2000, AJ, 120, 1579

Zahid, H. J., Kudritzki, R.-P., Conroy, C., Andrews, B., & Ho, I. T. 2017, ApJ, 847, 18

Zeldovich, Y. B. 1972, MNRAS, 160, 1P